# Synoptic-Scale Environments and Dynamical Mechanisms Associated with Predecessor Rain Events Ahead of Tropical Cyclones

Abstract of

a thesis presented to the Faculty

of the University at Albany, State University of New York

in partial fulfillment of the requirements

for the degree of

Master of Science

College of Arts & Sciences

Department of Atmospheric and Environmental Sciences

Benjamin J. Moore
2010

## ABSTRACT

Predecessor rain events (PREs) are distinct mesoscale regions of heavy rainfall that develop ahead of landfalling tropical cyclones (TCs) as a continuous poleward-moving stream of deep tropical moisture emanating from the TC encounters a region of ascent to produce heavy, prolonged rainfall. PREs present a forecast challenge because they have the potential to cause significant inland flooding, given that they are typically characterized by large rainfall totals (>100 mm in 24 h). An increased risk of flooding is posed if the TC rain shield subsequently passes over the region affected by the PRE. The primary objectives of this thesis are to: 1) document the distinct synoptic-scale configurations favorable for the development of PREs, and 2) examine the dynamical mechanisms associated with PREs. Accomplishing these objectives will ultimately lead to the development of a set of operational forecasting tools and techniques not only to diagnose the potential for PRE development but also to predict how a PRE may evolve in time and space.

A climatology of PREs occurring in the U.S. ahead of North Atlantic basin TCs during 1988–2008 is presented in order to document the temporal and geographical distributions and the statistical properties of PREs. In conjunction with this climatology, PREs are stratified into three distinct categories: "jet in ridge" (JR), "southwesterly jet" (SJ), and "downstream confluence" (DC), based upon the configuration of the upper-tropospheric flow within which the PRE and TC are embedded. PRE-relative composites are presented in order to elucidate the key synoptic-scale features and dynamical mechanisms associated with each PRE category. While the PRE-relative composites for

each category indicate that PREs tend to develop as a stream of moisture from a TC encounters a region of ascent situated along a low-level baroclinic zone and beneath the equatorward entrance region of an upper-level jet streak, the lower- and upper-level synoptic-scale flow configurations associated with each category differ markedly. Moreover, the role of the TC in establishing favorable conditions for PRE development varies among the three categories.

Detailed case studies of the PREs that occurred ahead of TC Rita (2005; JR category), TC Wilma (2005; SJ category), and TC Ernesto (2006; DC category) are performed in order to investigate the dynamical mechanisms associated with each PRE category. The findings for these three case studies bolster the findings for the PRE-relative composites by providing considerable insight into the diverse synoptic and mesoscale mechanisms that can be associated with PRE development. Based upon the results of these case studies and of the PRE-relative composites, conceptual models are presented in order to illustrate the salient features and processes associated with each PRE category.

# Synoptic-Scale Environments and Dynamical Mechanisms Associated with Predecessor Rain Events Ahead of Tropical Cyclones

A thesis presented to the Faculty

of the University at Albany, State University of New York

in partial fulfillment of the requirements

for the degree of

Master of Science

College of Arts & Sciences

Department of Atmospheric and Environmental Sciences

Benjamin J. Moore
2010

## ACKNOWLEDGMENTS

I would first like to thank my family, especially Mom and Dad, for the continuous support they have given me throughout my time in graduate school; I could not have done it without them. Second, I would like to thank my dear friend Claire for all the love, comfort, and guidance she has given me during my last year in graduate school.

Thanks go out to my advisors, Dr. Dan Keyser and Dr. Lance Bosart, for their incredible guidance (academic, scientific, and otherwise) through the course of this research. My fellow graduate students need to be acknowledged for making my experience in graduate school truly pleasurable and for offering continuous assistance during this research. Considerable assistance in preparing the computer routines utilized to analyze data and to generate plots during this research was provided by Jay Cordeira, Alan Srock, and Kevin Tyle. I would also like to thank Patti Seguin and Barbara Zampella for their assistance in various administrative matters. My sincere gratitude goes out to Ross Lazear for his assistance in printing and submitting this thesis.

Lastly, I would like to thank Mike Jurewicz of the Binghamton, NY, NWS forecast office for serving as the NWS focal point for this research under the Collaborative Science, Technology, and Applied Research (CSTAR) program. His addition of an operational perspective was quite valuable for this research. This research was supported by the National Oceanic and Atmospheric Administration (NOAA) Grant NA07NWS4680001, awarded to the University at Albany, SUNY as part of the CSTAR program.

## TABLE OF CONTENTS

## LIST OF TABLES

## LIST OF FIGURES

Figure 5.9: Ten 36-h backward kinematic air parcel trajectories ending within the PRE region at 0600 UTC 25 September 2005 overlaid on the NCEP 1° GFS total PW analysis at 1800 UTC 23 September 2005 (shaded in mm according to the color bar on the left). The red (black) numbers denote the ending (beginning) point of each trajectory. Trajectories 1–5 begin at 850 hPa and trajectories 6–10 begin at 700 hPa. The white circles mark the 0000 UTC 25 September and 0000 UTC 24 September air parcel positions. The air parcel pressure values (hPa) are shaded according to the color bar at the bottom. For reference, the track of TC Rita subsequent to 1800 UTC 23 September 2005 is indicated by the blue arrow, and the positions of TC Rita at 1800 UTC 23 September, 0000 UTC 25 September, and 0600 UTC September 2005 are marked by the tropical storm symbols. The dashed blue line indicates the location of the 925-hPa baroclinic zone at 0600 UTC 25 September.

Figure 5.10: 200-hPa irrotational wind vectors (> 5 m $s^{-1}$; reference vector is at the bottom of each panel), 200-hPa wind speed (shaded in m $s^{-1}$ according to the color bar ), 700-hPa ascent (contoured in red every $5 \times 10^{-3}$ hPa $s^{-1}$ starting at $-5 \times 10^{-3}$ hPa $s^{-1}$), and 250–200-hPa PV (0.5, 1, 2, 4, and 6 PVU contours shown in black) generated from the NCEP 1° GFS analyses at (a) 0000 UTC, (b) 0600 UTC, and (c) 1200 UTC 25 September 2005. The TC and PRE locations are denoted by the tropical storm symbol and the star, respectively. Cross-section E–F is indicated in panels (a) and (c).

Figure 5.11: Vertical cross sections generated from the NCEP 1° GFS analyses showing potential temperature (contoured in gray every 3 K), ascent (contoured in red every $5 \times 10^{-3}$ hPa $s^{-1}$ starting at $-5 \times 10^{-3}$ hPa $s^{-1}$), PV (shaded in PVU according to the color bar), and horizontal wind speed (contoured in black every 10 m $s^{-1}$ starting at 30 m $s^{-1}$) at (a) 0000 UTC and (b) 1200 UTC 25 September 2005. Panel (b) also shows positive 12-h potential temperature changes (contoured in green every 0.5 K starting at 1 K and every 1 K starting at 3 K) between 0000 UTC and 1200 UTC 25 September. The cross-section location is indicated in Figs. 5.10a,c.

Fig. 5.12: The NHC Best Track positions for TC Ernesto during 29 August–3 September 2006 overlaid on the NPVU QPE analysis (shaded in mm according to the color bar) for 1200 UTC 30 August–1200 UTC 1 September 2006. The filled (unfilled) circles denote the 0000 UTC (1200 UTC) TC positions. The inset in the upper-left corner shows NPVU QPE analysis (shaded in mm according to the color bar) for 1200 UTC 30–1200 UTC 31 August 2006.

Figure 5.13: As in Fig. 5.3, except for 1800 UTC 30 August 2006.

Figure 5.14: NCEP 20-km RUC analyses of 2-m potential temperature (contoured in red every 2 K) and 10-m winds (barbs in m $s^{-1}$ according to the convention in Fig. 5.2) overlaid on WSI NOWrad radar reflectivity mosaics (shaded in dB*Z* according to the color bar) at (a) 1800 UTC 30 August, (b) 2100 UTC 30 August, (c) 0000 UTC 31 August, and (d) 0600 UTC 31 August 2006. Cross sections A–B and C–D are indicated in panels (b) and (c), respectively. The TC location is denoted by the tropical storm symbol.

Figure 5.22: The NHC Best Track positions for TC Wilma during 16–26 October 2005 overlaid on the NPVU QPE analysis (shaded in mm according to the color bar) for 1200 UTC 23–1200 UTC 25 October 2005. The filled (unfilled) circles denote the 0000 UTC (1200 UTC) TC positions. The red numbers indicate the 1200 UTC central sea level pressure values (hPa) for TC Wilma. The red dashed line indicates the time and location at which TC Wilma was classified as extratropical.

Figure 5.23: *GOES-12* IR (~11 $\mu$m) satellite imagery at (a) 1800 UTC 23 October, (b) 0000 UTC 24 October, (c) 0600 UTC 24 October, and (d) 1200 UTC 24 October 2005. The "W" and the "α" symbols indicate the positions of TC Wilma and TS Alpha, respectively. [Images courtesy of the National Climatic Data Center (NCDC) GIBBS web site at http:// www.ncdc.noaa.gov/gibbs/].

Figure 5.24: WSI NOWrad radar reflectivity mosaics (shaded in dB*Z* according to the color bar) at (a) 1800 UTC 23 October, (b) 0000 UTC 24 October, (c) 0300 UTC 24 October, (d) 0600 UTC 24 October, (e) 1200 UTC 24 October, and (f) 1800 UTC 24 October 2005.

Figure 5.25: As in Fig. 5.3, except for 1800 UTC 23 October 2005, and the position of TS Alpha is indicated by the "α" symbol.

Figure 5.26: 850-hPa geopotential height (contoured in black every 2 dam), potential temperature (contoured in blue every 2 K), Petterssen frontogenesis [contoured in green every 1 K (100 km)$^{-1}$ (3 h)$^{-1}$ starting at 1 K (100 km)$^{-1}$ (3 h)$^{-1}$], and positive potential temperature advection (shaded in $10^{-5}$ K s$^{-1}$ according to the color bar) generated from the NCEP 1° GFS analyses at (a) 1800 UTC 23 October, (b) 0000 UTC 24 October, (c) 0600 UTC 24 October, and (d) 1200 UTC 24 October 2005. Cross section A–B is indicated in panel (c).

Figure 5.27: As in Fig. 5.16, except generated from the NCEP 1° GFS analysis at 0600 UTC 24 October 2005. The star denotes the position of the PRE. The cross section location is indicated in Fig. 5.26c.

Figure 5.28: As in Fig. 5.17, except generated from the NCEP 1° GFS analyses at (a) 1800 UTC 23 October, (b) 0000 UTC 24 October, (c) 0600 UTC 24 October, and (d) 1200 UTC 24 October 2005.

Figure 5.29: As in Fig. 5.18, except all trajectories end at 600 hPa at 0600 UTC 24 October 2005, and the PW analysis at 1800 UTC 22 October is shaded. The dashed blue line denotes the axis of maximum radar reflectivity values associated with the PRE at 0600 UTC 24 October. The red "α" symbol denotes the position of TS Alpha at 1800 UTC 22 October.

Figure 5.30: As in Fig. 5.10, except for (a) 1800 UTC 23 October, (b) 0600 UTC 24 October, (c) 1200 UTC 24 October, and (d) 1800 UTC 24 October 2005.

## 1. Introduction

### 1.1 Motivation and objectives

The predecessor rain event (PRE) was first defined by Cote (2007, hereafter C07) as a coherent mesoscale region of heavy rainfall that develops as moisture originating from the vicinity of a tropical cyclone (TC) is transported by the synoptic-scale flow towards a region of atmospheric lifting well ahead of the TC. Sustained by deep tropical moisture characterized by precipitable water (PW) values often in excess of 50 mm, PREs are frequently manifested as persistent bands of heavy rainfall, with rainfall rates in excess of 100 mm $(24\ h)^{-1}$. They therefore possess significant potential to cause extreme rainfall totals and high-impact flooding, an aspect that has been highlighted by the recent devastating flood-producing PREs associated with TC Frances (2004), TC Katrina (2005; C07), TC Erin (2007; Galarneau et al. 2010, hereafter GBS10), and TC Ike (2008).

Due to the substantial focus likely paid to local effects of landfalling TCs (i.e., high winds, storm surge, outer rainbands, eyewall convection) by operational forecasters and the lack of attention paid to their possible remote effects, PREs have the potential to take both the operational forecasting community and the general public by surprise. Adding to this problem, PREs may be poorly forecasted by numerical models due to their inability to: 1) adequately resolve mesoscale features and characteristics associated with heavy-rain-producing convective systems (Davis et al. 2003; Jankov and Gallus 2004), and 2) represent the dynamical and thermodynamic environmental influences of a TC moving into the midlatitudes (e.g., Atallah and Bosart 2003). Faced with these challenges, improved forecasting of PREs relies, in large part, on forecasters' ability to recognize synoptic-scale patterns and key ingredients that could be potentially favorable

for PRE development ahead of a TC. Specifically, we argue that a successful PRE forecast must involve a thorough identification of the processes that might lead to: 1) moisture transport from the TC to the PRE region, 2) sufficient forcing for upward vertical motion and thermodynamic instability to support heavy, convective rainfall in the presence of the TC moisture, and 3) quasi-stationary behavior of the precipitation system.

The goal of this thesis is to demonstrate, in a composite and case study framework, that there exist distinct, favorable pathways to PRE development, each representing a unique synoptic-scale configuration in which the three key factors: TC moisture, forcing for ascent, and slow precipitation system motion, culminate in the production of remote heavy rainfall ahead of a TC. Furthermore, we seek to elucidate the dynamical mechanisms that govern the spatial and temporal characteristics of PREs within these synoptic-scale configurations. Accomplishing these objectives will ultimately lead to the development of a set of operational forecasting tools and techniques not only to assess the potential for PRE development but also to project how it may evolve in time and space.

## 1.2 Background

### *1.2.1 Previous work on PREs*

Though the PRE was only recently defined by C07, the concept has its origins in a study by Bosart and Carr (1978), which examined a heavy rain event in western New York and Pennsylvania ahead of TC Agnes (1972). Bosart and Carr documented how a stream of deep tropical moisture from the TC Agnes circulation interacted with a baroclinic environment, producing > 200 mm of rainfall well ahead of TC Agnes. The

remote region of heavy rainfall developed as moisture from TC Agnes streamed northward along the Appalachians towards a region of confluent flow and quasi-geostrophic (QG) forcing for ascent associated with an approaching midtropospheric short-wave trough. This process, illustrated schematically in Fig. 1.1, shows that the PRE developed remotely from the rain region directly associated with TC Agnes and, moreover, that it was dynamically driven by processes *external* to the TC.

The concepts expounded by Bosart and Carr (1978) on antecedent heavy rainfall ahead of TCs were recently extended by C07, who conducted a climatology of PREs associated with Atlantic basin TCs during 1998–2006. C07 identified 47 PREs associated with 21 TCs and stratified them by their position relative to the total observed track of the TC, finding that 26 occurred left of the TC track (LOT), 12 along track (AT) and 9 right of track (ROT). On average, PREs were separated from their parent TCs by approximately 1000 km and preceded the passage of the TC past the latitude at which the PRE occurred by ~36 h. Through composite analysis and case studies, C07 showed that PREs tended to form in a region where a poleward moisture surge from a TC interacted with a region of lift associated with a low-level baroclinic zone and the equatorward entrance region of an upper-tropospheric jet streak (Fig. 1.2a). In addition, C07 suggested that regions of orographic lifting and mesoscale boundaries associated with coastal fronts and regions of cold air damming could also be loci for PRE development (Fig. 1.2b). A recent study by Srock and Bosart (2009) showed that a coastal front on the oceanward side of a region of cold air damming in the lee of the southern Appalachian Mountains acted as the focus for antecedent heavy rainfall ahead of TC Marco (1990).

GBS10 examined the environments of PREs that occurred during 1995–2008 in a

storm-relative composite framework and through a case study of a high-impact PRE associated with TC Erin (2007). They documented the importance of the interaction of a region of deep baroclinicity beneath the equatorward entrance region of an upper-tropospheric jet streak with a poleward surge of moisture from the TC for PRE development. Specifically, frontogenesis and warm-air advection, driven by the impingement of strong low-level flow between the TC and an anticyclone to its east upon a low-level baroclinic zone, serves as a focus for PRE development, while further dynamical support is provided at upper levels as diabatically generated low potential vorticity (PV) outflow associated with the TC acts to strengthen the upper-tropospheric jet streak downstream of an advancing trough.

*1.2.2. Relationship of PREs to heavy rainfall events*

The results from the C07 and GBS10 studies suggest that the synoptic and mesoscale conditions associated with PREs closely resemble those associated with the "frontal" pattern for flash-flood-producing mesoscale convective systems (MCSs; Fig. 1.3) first documented by Maddox et al. (1979). The environmental properties and dynamical processes associated with this configuration are well documented (e.g., Maddox et al. 1979; Augustine and Caracena 1994; Glass et al. 1995; Junker et al. 1999; Moore et al. 2003; Schumacher and Johnson 2005, 2006) and typically are dominated by the advection of warm, moist air by a low-level jet (LLJ) towards a quasi-stationary low-level baroclinic zone (Figs. 1.3a,b) downstream of a weak 500-hPa short-wave trough (Fig. 1.3c). In this configuration, warm-air advection, moisture convergence, and convective destabilization maximized at the intersection of the LLJ with the baroclinic

zone provide the necessary ingredients to initiate and maintain MCSs. Additionally, frontogenesis associated with horizontal speed convergence and horizontal deformation at the terminus of the LLJ has been shown to be an important mesoscale lifting mechanism to support MCSs (e.g., Trier and Parsons 1993; Augustine and Caracena 1994; Trier et al. 2006).

Within an environment of sufficient moisture, instability, and lift to support convection, prolonged heavy rainfall accompanying PREs and MCSs associated with the "frontal" pattern is favored by slow system movement and convective cell "training" (e.g., Doswell et al. 1996), a process by which convective cells repeatedly pass over a given area. Most frequently the mesoscale organization of PREs and heavy-rain-producing MCSs resembles the "training line/adjoining stratiform" (TL/AS) and "backbuilding/quasi-stationary" (BB) extreme-rain-producing MCS archetypes (Fig. 1.4) defined by Schumacher and Johnson (2005). Both of these organizational modes characterized the PRE associated with TC Erin (2007), examined by GBS10. In this event, a line of convection oriented parallel to the 0–6 km vertical wind shear resulted in the repeated passage of convective cells over southern Minnesota and western Wisconsin (TL/AS organization), while new cells continuously developed directly upstream (BB organization), keeping the line stationary. Such a combination of the TL/AS and BB organizational modes allows for high rainfall rates to persist for a prolonged period of time, therefore posing a substantial risk for locally extreme rainfall totals and flash flooding (e.g., Chappell 1986; Doswell 1996; Junker et al. 1999; Schumacher and Johnson 2005).

For TL/AS MCSs (Fig. 1.4a), veering wind direction with height at low levels and

weak-to-moderate midlevel speed shear oriented parallel to the axis of convection favor slow, line-parallel MCS motion (e.g., Maddox et al. 1979; Junker et al. 1999; Schumacher and Johnson 2005). For BB MCSs (Fig.1.4b), persistent moisture convergence and mesoscale lifting, afforded by the interaction of a low-level jet with a surface frontal boundary, favors the continuous development of convective cells upstream of an antecedent convective line (e.g., Chappell 1986; Glass et al. 1995; Doswell et al. 1996; Schumacher and Johnson 2005). In addition, environments characterized by high relative humidity and, correspondingly, high PW values, which are typical of PREs (GBS10), favor high precipitation efficiencies (Market et al. 2003) and preclude the formation of strong downdrafts, which would otherwise favor forward system propagation (e.g., Doswell et al. 1996; Davis 2001).

On the synoptic scale, dynamical support for heavy rainfall associated with MCSs and PREs is often provided by an upper-tropospheric jet streak (e.g., Uccellini and Johnson 1979) or by an approaching short-wave trough (e.g., Bosart and Carr 1978; Doswell and Bosart 2001). Though typically not sufficient to trigger convection, the QG forcing for ascent associated with an ageostrophic circulation accompanying a jet streak or associated with upward increasing cyclonic vorticity advection linked to a short-wave trough can aid in both environmental moistening and thermodynamic destabilization, thereby making conditions favorable for convection (Doswell 1987).

The indirect and direct thermal circulations associated with an upper-tropospheric jet streak can couple with the thermally direct circulation associated with a region of lower-tropospheric frontogenesis, thus producing troposphere-deep regions of ascent (Keyser 1999; Hakim and Keyser 2001). Typically, the superposition of lower- and

upper-tropospheric thermally direct circulations, illustrated in Fig. 1.5, occurs frequently in environments of heavy-rain-producing MCSs in the warm season (e.g., Junker et al. 1999; Moore et al. 2003) and in the environments of PREs (C07; GBS10). As these thermally direct circulations couple, they can be further augmented by latent heat release within a persistent region of heavy rainfall. This heating can act to strengthen thermal gradients in the middle troposphere and thereby enhance frontogenesis (Hsie et al. 1984; Colle 2003). In addition, the diabatically generated anticyclonic outflow at upper levels associated with the region of heavy rainfall can strengthen the upper-tropospheric jet streak, leading to an enhanced thermally direct circulation in the entrance region (e.g., Maddox et al. 1981; Keyser and Johnson 1984; Wolf and Johnson 1995).

In some PRE cases, such as TC Fran (1996) studied by C07 in which baroclinicity and QG forcing for ascent were weak, persistent moist upslope flow along orographic features, such as the Appalachian Mountains, can be the main focus for the development of heavy rainfall. Elevated terrain can serve as an anchor for quasi-stationary heavy rainfall provided that the flow remains upslope and that moisture and instability are continuously replenished (e.g., Maddox et al. 1978; Lin et al. 2001). The lifting of moist, unstable air over elevated terrain has been frequently implicated as a mechanism for extreme rainfall in the western Mediterranean (e.g., Doswell et al. 1998; Romero et al. 2000) and along the northwestern coast of the U.S. (e.g., Ralph et al. 2005), and can also result in the enhancement of precipitation directly associated with landfalling TCs (e.g., Schwarz 1970; Sinclair 1994).

*1.2.3 PREs in the context of extratropical transition of TCs*

Though the environments and the physical mechanisms associated with PREs closely resemble those classically implicated for flash flooding and heavy rainfall, PREs should, nonetheless, be treated separately from ordinary heavy rain events due to both the direct and indirect dynamical and thermodynamic influences of a TC on their formation. Indeed, analogies can be drawn between the PRE process and the extratropical transition (ET) process, though we stress that they are two distinct processes. The composite analyses and case studies conducted by C07 and GBS10 indicate that the Maddox et al. (1979) "frontal" pattern in the environments of PREs often arises as strong poleward low-level flow associated with the outer circulation of the TC, aided by anticyclonic flow to its east, impinges upon a low-level baroclinic zone beneath the equatorward entrance region of an upper-tropospheric jet streak. This setup, characterized by veering winds with height at low levels in the presence of warm-air advection, frontogenesis, and deep moisture flux from the TC, favors the formation of a quasi-stationary region of heavy rainfall along the baroclinic zone. This configuration is analogous to the transformation stage of ET (Fig. 1.6), documented by Klein et al. (2000), wherein frontogenesis and warm-air advection serve as lifting mechanisms for the development of heavy rainfall ahead of a poleward-moving TC as its circulation begins interacting with a pre-existing baroclinic zone. The key distinction for PREs in this context is that they are *separate* entities from the main TC rain shield.

Additionally, as is common for PREs (GBS10), the ET process involves the favorable interaction of a TC with an approaching middle-/upper-tropospheric trough (e.g., DiMego and Bosart 1982a,b; Harr et al. 2000; Atallah and Bosart 2003). During

this interaction, the development of large vorticity gradients in the middle and upper troposphere between the approaching trough and the diabatically generated outflow ridge associated with the TC leads to enhanced QG forcing for ascent associated with cyclonic vorticity advection by the thermal wind (e.g., Bosart and Lackmann 1995; Klein et al. 2002; Atallah and Bosart 2003; Atallah et al. 2007). This forcing for ascent, in turn, favors the formation of asymmetries in the TC rain shield and contributes to the reintensification of the TC as an extratropical cyclone.

As the TC undergoes ET, the reduction of PV and attendant ridge building in the upper troposphere due to diabatic processes (i.e., latent heating) associated with the TC rain shield can result in enhanced downstream upper-tropospheric PV gradients (or similarly geopotential height gradients), leading to the strengthening of a downstream upper-tropospheric jet streak (e.g., Bosart and Lackmann 1995; Atallah and Bosart 2003; Agustí-Panareda et al. 2004). Reimer et al. (2008) showed the intensification of a downstream upper-tropospheric jet streak occurs during ET in association with the poleward advection of low-PV air by the diabatically generated divergent outflow associated with a transitioning TC. As a jet streak strengthens in response to diabatic processes, the ageostrophic circulation within the entrance region can be enhanced, which leads to greater ascent and enhanced heavy rainfall poleward of the TC center (e.g., Bosart and Lackmann 1995; Atallah and Bosart 2003). The composite analysis conducted by GBS10 suggests that the strengthening of an upper-tropospheric jet streak in response to diabatic heating and attendant ridge amplification accompanying the TC is likely an important process in PRE development.

### *1.2.4 Remote rainfall associated with TCs in the North Pacific*

Recent studies have investigated the influence of TCs in the Western and Eastern North Pacific on distant rainfall, suggesting that conditions favorable for PREs are not limited to Atlantic basin TCs. Wang et al. (2009) showed how moisture advected by the outer circulation of Typhoon Songda (2004) contributed to distant heavy rainfall in Japan as it recurved along the eastern coast of Asia. Eastern North Pacific TCs have been linked to moisture surges in the Gulf of California, which in turn impact rainfall in northwestern Mexico and the southwestern United States (e.g., Higgins and Shi 2005; Farfán and Fogel 2007). Recent work by Corbosiero et al. (2009) and Svoma (2010) has documented the important contribution of eastern North Pacific TC moisture to rainfall distributions over the southwestern United States.

## 1.3 Thesis format

The remainder of this thesis is organized as follows. Chapter 2 will document the various data sources and methods employed to identify and stratify PRE cases, to construct composite analyses, and to conduct case studies. A climatology of PREs that occurred during 1988–2008 will presented in chapter 3, and PRE-relative composite analyses will be presented in chapter 4. Chapter 5 will present multiscale case studies of PREs associated with TC Rita (2005), TC Wilma (2005), and TC Ernesto (2006). The results of this thesis will be summarized and discussed in chapter 6. Chapter 7 will provide concluding remarks and suggestions for future work.

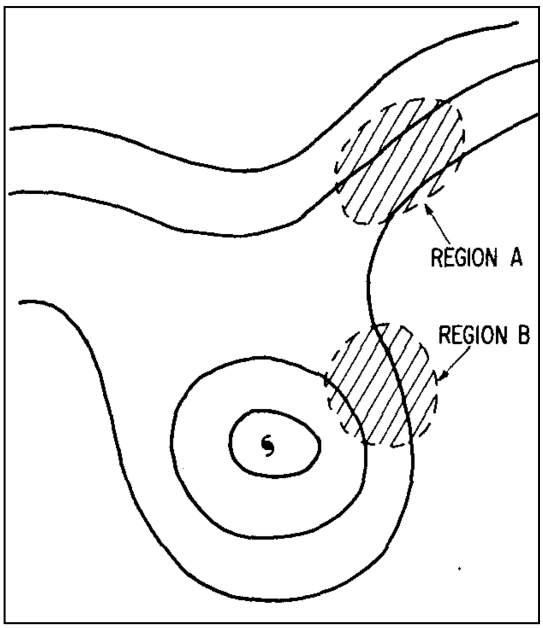


Figure 1.1: Schematic midtropospheric streamlines associated with a PRE ahead of TC Agnes (1972). Shaded regions indicate loci of heavy rainfall. Reproduced from Fig. 13 in Bosart and Carr (1978).

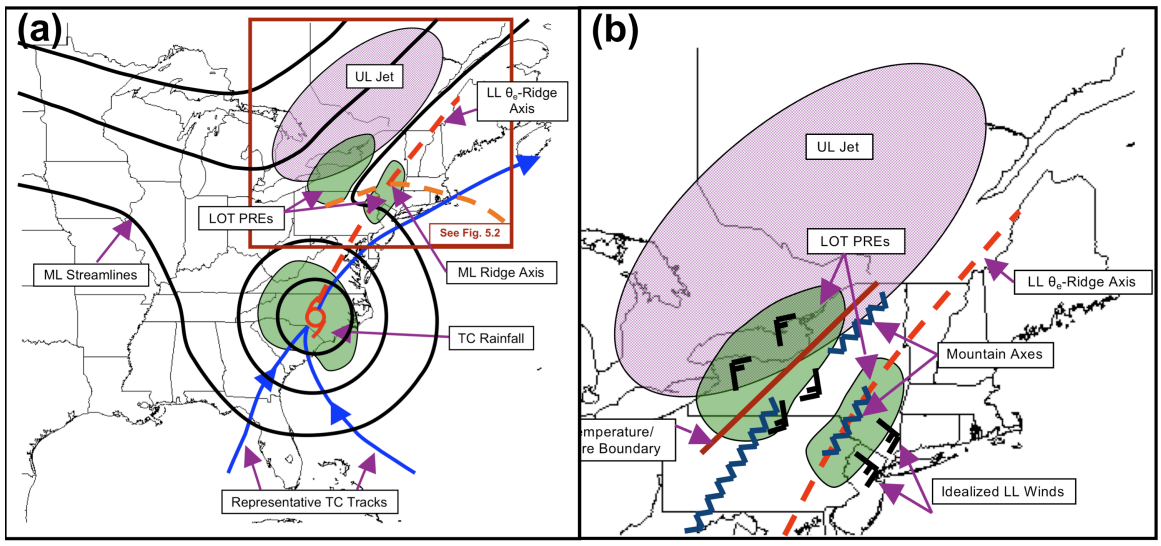


Figure 1.2: Conceptual model of the synoptic-scale environment associated with LOT PREs in advance of TCs, revised and updated from Bosart and Carr (1978). Position of TC is given by tropical storm symbol. Representative TC tracks are marked with solid blue arrows. Low-level (LL) features are representative of the 925-hPa level, midlevel (ML) features are representative of the 700-hPa level, and upper-level (UL) features are representative of the 200-hPa level. Boxed region indicates the area of the mesoscale and physiographic conceptual model shown in panel (b). Reproduced from Figs. 5.1 and 5.2 in C07.

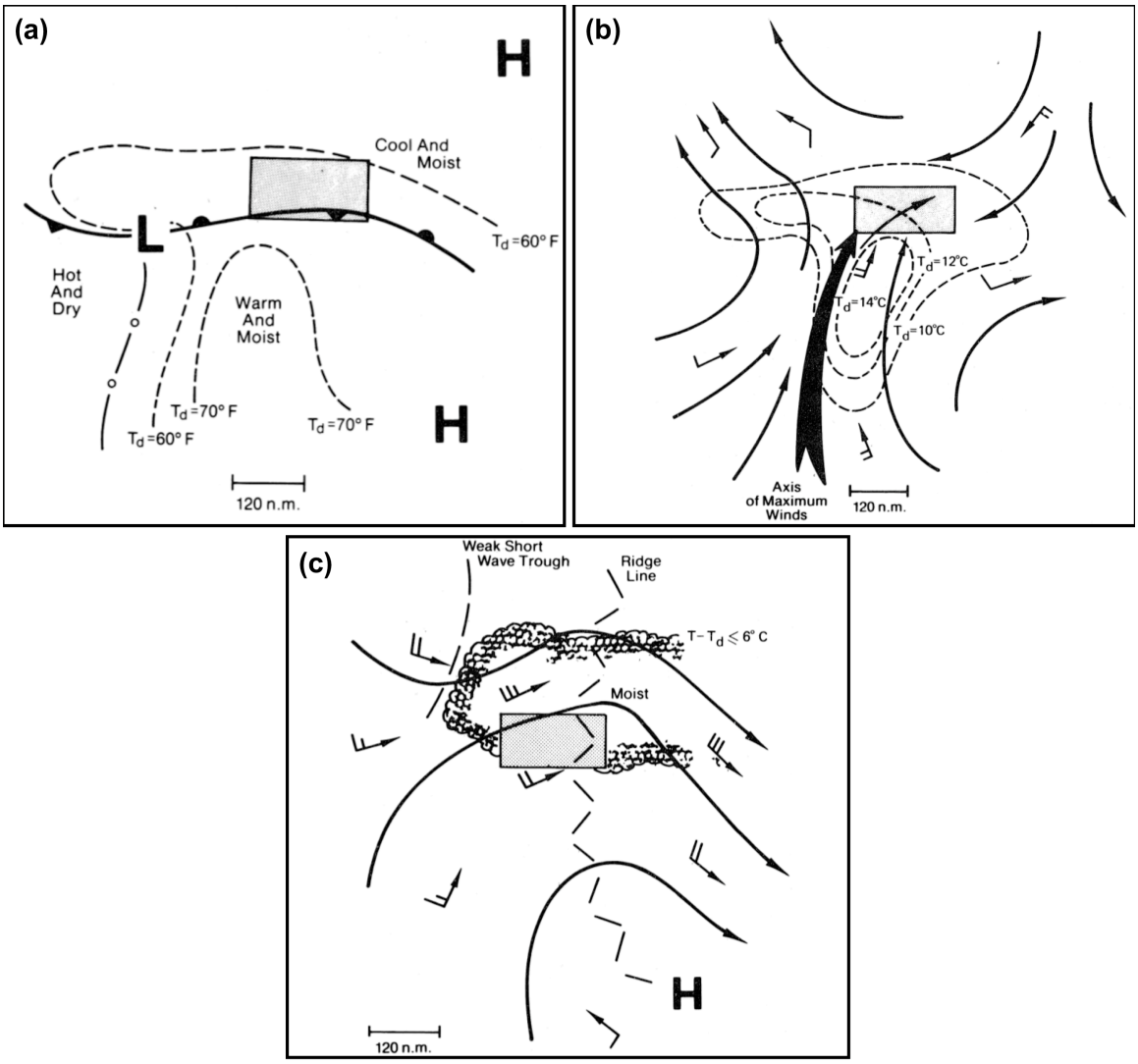


Figure 1.3: Schematic depictions of the (a) surface, (b) 850 hPa, and (c) 500 hPa patterns associated with the "frontal" type flash flooding scenario. The shaded box indicates the region of greatest potential for heavy rainfall and flash flooding. Figure reproduced from Figs. 8a–c in Maddox et al. (1979).

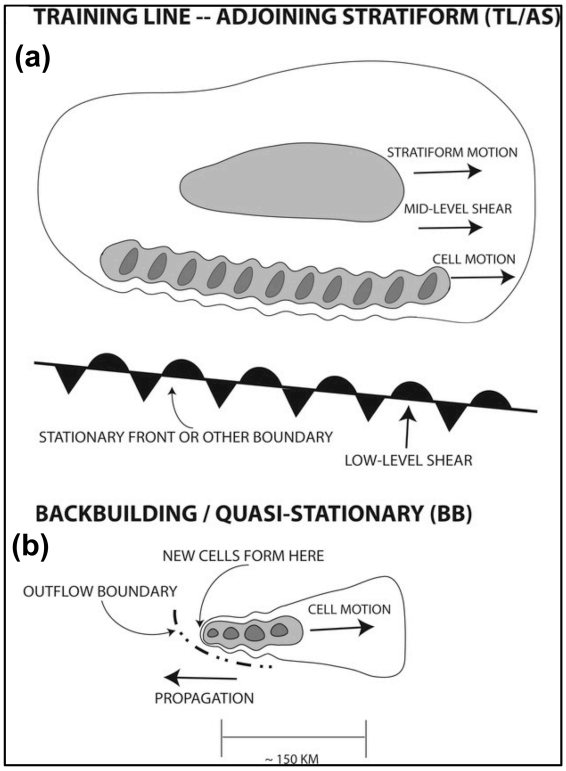


Figure 1.4: Schematic diagram of the radar-observed features of the (a) TL/AS and (b) BB patterns of extreme-rain-producing MCSs. Contours (and shading) represent approximate radar reflectivity values of 20, 40, and 50 dB*Z*. In (a), the low-level and midlevel shear arrows refer to the shear in the surface-to-925-hPa and 925–500-hPa layers, respectively, as discussed in section 4 of Schumacher and Johnson (2005). The dash–dot line in (b) represents an outflow boundary; such boundaries were observed in many of the BB MCS cases. The length scale at the bottom is approximate and can vary substantially, especially for BB systems, depending on the number of mature convective cells present at a given time. Caption and figure reproduced from Fig. 3 in Schumacher and Johnson (2005).

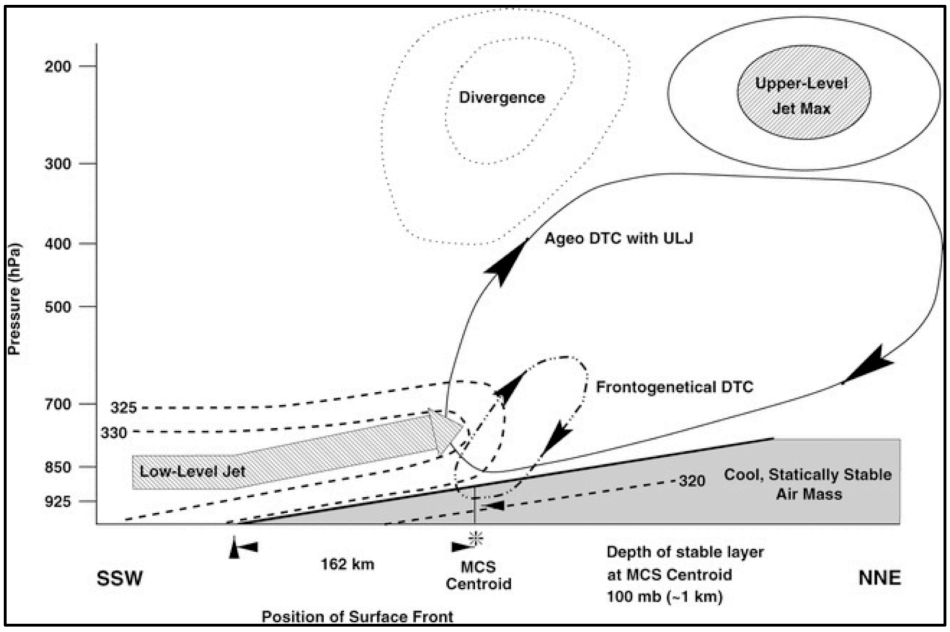


Figure 1.5: Schematic cross section of an elevated convective event taken parallel to a low-level jet (LLJ) across a surface frontal zone. Dashed lines represent typical $\theta_e$ values, the large stippled arrow represents the ascending LLJ, the thin solid oval with arrows represents the ageostrophic direct thermal circulation (DTC) associated with the upper-level jet (ULJ), and the dash–dotted oval with arrows represents the DTC associated with the low-level frontogenetical forcing. The area aloft enclosed by dotted lines indicates upper-level divergence; the area aloft enclosed by solid lines denotes the location of the ULJ. Note that in this cross section, the horizontal distance between the MCS and the location of the ULJ is not to scale. Caption and figure reproduced from Fig. 14 in Moore et al. (2003).

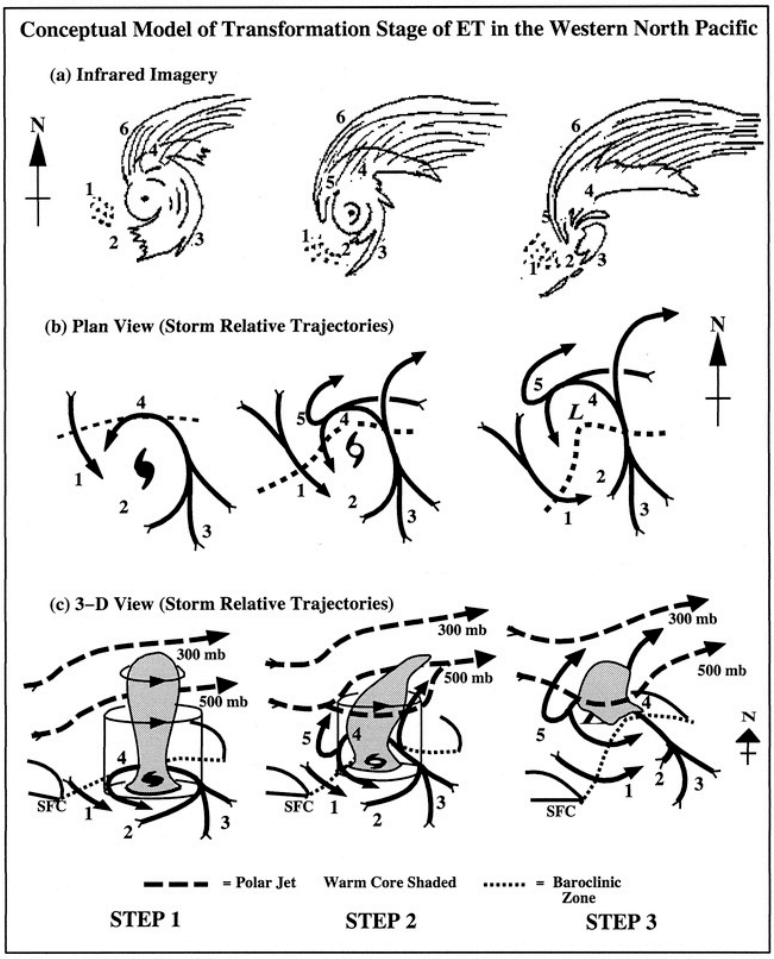


Figure 1.6: Conceptual model of transformation stage of ET in the western North Pacific, with labeled areas as follows: 1) environmental equatorward flow of cooler, drier air (with corresponding open cell cumulus); 2) decreased TC convection in the western quadrant (with corresponding dry slot) in step 1, which extends throughout the southern quadrant in steps 2 and 3; 3) environmental poleward flow of warm, moist air is ingested into TC circulation, which maintains convection in the eastern quadrant and results in an asymmetric distribution of clouds and precipitation in steps 1 and 2; steps 2 and 3 also feature a southerly jet that ascends tilted isentropic surfaces; 4) ascent of warm, moist inflow over tilted isentropic surfaces associated with baroclinic zone (dashed line) in middle and lower panels; 5) ascent (undercut by dry-adiabatic descent) that produces cloudbands wrapping westward and equatorward around the storm center; dry-adiabatic descent occurs close enough to the circulation center to produce erosion of eyewall convection in step 3; 6) cirrus shield with a sharp cloud edge if confluent with polar jet. Caption and figure reproduced from Fig. 5 in Klein et al. (2000).

## 2. Data and methods

### 2.1 PRE identification

The PRE databases from C07 and GBS10 were extended to include all PREs during 1988–2008 (Table 1). In contrast to GBS10, our analysis closely follows that of C07 by considering multiple PREs per TC rather than just the initial PRE. Coherent regions of rainfall occurring in advance of landfalling and near-landfalling TCs were identified as PREs based upon the following criteria (after GBS10):

- Radar reflectivity values $\geq 35$ dB$Z$ within a coherent area of rainfall must persist for at least 6 h.
- The average rainfall rate must be $\geq 100$ mm $(24\ \text{h})^{-1}$ over duration of the PRE.
- In addition to the radar reflectivity and rainfall rate criteria, the following two criteria must be satisfied:
  - There must be a clear horizontal separation depicted in the radar imagery between the coherent area of rainfall and the TC rain shield.
  - Deep tropical moisture directly associated with the TC must be advected from the TC by the lower-/middle-tropospheric flow into the region of the coherent area of rainfall.

Candidate PREs that occurred during 1988–1994 were manually tracked using the National Oceanic and Atmospheric Administration (NOAA) National Climatic Data Center (NCDC) United States radar summary charts archived on 35 mm microfilm at the University at Albany Science Library. For cases that occurred during 1995–2008, the

manual tracking was done using national radar reflectivity mosaics available from the National Center for Atmospheric Research (NCAR) case selection archive (http://locust.mmm.ucar.edu/imagearchive/) and from NCDC (http://www4.ncdc.noaa.gov/cgi-win/wwcgi.dll?wwNexrad~Images2). Although the radar summary charts used to track cases during 1988–1994 are available at coarser spatial and temporal resolution than the radar mosaics used for cases during 1995–2008, they still allowed for the identification of what we contend to be the major PREs during that time period. In the course of the manual radar tracking, an effort was made to delineate coherent, organized areas of rainfall from more transient, scattered areas of rainfall. Contemporaneous or consecutive organized areas of rainfall associated with the same parent TC were considered to be distinct, separate PREs; however, broken areas of rainfall situated within a larger coherent area of rainfall were considered to constitute a single PRE. Each PRE was tracked until it weakened and no longer met the $\geq 35$ dB$Z$ radar reflectivity threshold, or until it merged with the main TC rain shield and no longer constituted a distinct region of rainfall.

Precipitation amounts for cases that occurred during 2001–2008 were determined using the quantitative precipitation estimates (QPE) gridded dataset (McDonald and Baker 2001) available for the continental United States at 4-km horizontal resolution and 6-h temporal resolution from the National Precipitation Verification Unit (NPVU; http://www.hpc.ncep.noaa.gov/npvu/archive/rfc.shtml). For cases occurring prior to 2001, the NOAA Climate Prediction Center (CPC) Unified Precipitation Dataset (UPD; Higgins et al. 2000) was used. This dataset is gridded at a horizontal resolution of 0.25° × 0.25° and is available for download from the NOAA Earth System Research

Laboratory (ESRL; http://www.esrl.noaa.gov/psd/data/gridded/data.unified.html). Observations from the National Weather Service (NWS) cooperative high-resolution 24-h rain gauge network and the hourly precipitation dataset (HPD), both archived at NCDC (http://www.ncdc.noaa.gov/oa/climate/climatedata.html), were used to supplement the gridded precipitation datasets.

Moisture transport from the TC to the PRE region was investigated for each PRE case using gridded analyses of PW and the synoptic-scale flow generated from the National Centers for Environmental Prediction–National Center for Atmospheric Research (NCEP–NCAR) Reanalysis dataset (Kalnay et al. 1996; Kistler et al. 2001), with 2.5° × 2.5° horizontal resolution and 6-h temporal resolution. Observed upper-air and surface charts archived at the NOAA Storm Predicition Center (SPC; http://w1.spc.woc.noaa.gov/obswx/maps/), as well as twice-daily atmospheric soundings archived at the University of Wyoming (http://weather.uwyo.edu/upperair/sounding.html), were used as supplementary resources to verify the gridded analyses.

## 2.2 PRE stratification scheme

A subjective PRE stratification scheme based upon the synoptic-scale upper-tropospheric flow configuration characterizing the environment of the PRE and the TC was developed in order to identify dynamically distinct flow patterns for PRE development. Synoptic-scale charts of the 200-hPa flow generated from the 2.5° NCEP–NCAR Reanalysis dataset were analyzed for each case, and the cases were subsequently stratified based upon the following factors:

- Positions of major trough and ridge axes relative to the TC and PRE locations.
- Amplitude and orientation of the major troughs and ridges.
- Orientation and position of the upper-tropospheric jet streak relative to the TC and to the major trough and ridge axes.

From this stratification process, three distinct synoptic-scale patterns favorable for PRE development were identified (Fig. 2.1): "jet in ridge" (JR), "southwesterly jet" (SJ), and "downstream confluence" (DC). In the JR pattern (Fig. 2.1a), an anticyclonically curved jet streak is typically situated on the poleward flank of a broad ridge downstream of the axis of a positively tilted trough, with the PRE situated within the equatorward entrance region the jet streak. The SJ pattern (Fig. 2.1b) is generally characterized by a jet streak positioned in the southwesterly flow between an approaching trough upstream and a ridge extending poleward and eastward from the TC location, with the PRE located in the equatorward entrance region of the jet streak. The TC is typically located much closer to the jet streak and the upstream trough axis in the SJ pattern than in the JR pattern. For the DC pattern (Fig. 2.1c), the jet streak associated with PRE development is situated within a trough-over-ridge configuration downstream of the TC. The upstream flow is typically weak and characterized by ridge poleward of a weak short-wave trough situated directly upstream of the TC.

## 2.3 Composite analysis

After stratifying the PRE cases, synoptic-scale composites were generated for the

time of PRE initiation (T−0 h), 12 h prior to PRE initiation (T−12 h), and 12 h after PRE initiation (T+12 h) for the JR, SJ, and DC categories using the 2.5° NCEP–NCAR Reanalysis dataset. The 6-h analysis time closest to the PRE initiation time was used for T–0 h; however, if the PRE initiation time fell halfway between analysis times, the later time was used. As in GBS10, the grids for each PRE case were shifted prior to calculating the composite fields such that the PRE centroid, subjectively determined from radar imagery, was positioned at the mean PRE location for each category. Only the initial PRE for each individual TC was used for the compositing in order to preclude the dominance of the composite signal by multiple PREs associated with the same TC. The initial PREs for the bolded TCs in Table 1 were used for the composites.

2.4 Case studies

The PREs associated with TC Rita (2005), TC Wilma (2005), and TC Ernesto (2006) were selected as representative case studies for the JR, SJ, and DC categories, respectively. To examine the dynamical processes associated with these cases, a suite of observational datasets and gridded model analyses was employed. Observational datasets included: (i) WSI Corporation NOWrad radar imagery with 2-km horizontal resolution and 15-min temporal resolution (Carbone et al. 2002, p. 2035), (ii) Hourly Automated Surface Observing System (ASOS) observations and twice-daily radiosonde data archived at the University at Albany, (iii) NCDC HPD observations, (iv) the NPVU gridded QPE dataset, and (v) the National Hurricane Center (NHC) Best Track dataset (http://www.nhc.noaa.gov/pastall.shtml).

The NCEP GFS 6-h gridded analyses with 1.0° × 1.0° horizontal resolution and 50-

hPa (25-hPa between 1000 hPa and 900 hPa) vertical resolution were used to generate synoptic-scale charts and to calculate diagnostic quantities. The Rapid Update Cycle (RUC) hourly analyses (Benjamin et al. 2002) gridded at 20-km horizontal resolution and 25-hPa vertical resolution were used to generate mesoscale analyses.

## 2.5 Diagnostics

### *2.5.1 QG forcing for vertical motion*

Regions of QG forcing for vertical motion were diagnosed using the **Q**-vector form of the QG omega equation (Hoskins et al. 1978), which can be written as [adapted from Martin 2006b, his Eq. (1)]:

$$\left(\sigma\nabla_p^2 + f_o^2\frac{\partial^2}{\partial p^2}\right)\omega = -2\nabla_p\cdot\vec{Q} \qquad (1)$$

where $\vec{Q}$ is defined as [adapted from Martin 2006b, his Eq. (2)]:

$$\vec{Q} = -f_o\gamma\left[\left(\frac{\partial\vec{V}_g}{\partial x}\cdot\nabla_p\theta\right)\hat{i} + \left(\frac{\partial\vec{V}_g}{\partial y}\cdot\nabla_p\theta\right)\hat{j}\right] \quad . \qquad (2)$$

In Eq. (2), $\gamma = (R/f_o p_o)(p_o/p)^{(c_v/c_p)}$, where $p_o$ is 1000 hPa. The σ term in Eq. (1) represents the static stability and is given by $\sigma = -(RT_r/p\theta_r)(\partial\theta_r/\partial p)$, where $T_r$ and $\theta_r$ are domain-averaged values of temperature and potential temperature on isobaric surfaces, respectively. Though we do not explicitly solve for $\omega$, Eqs. (1) and (2) are used to *qualitatively* determine regions of forcing for vertical motion, with regions of $\nabla\cdot\vec{Q} < 0$ $(> 0)$ implying forcing for ascent (descent).

*2.5.2 Frontogenesis*

Frontogenesis was calculated as an additional diagnostic to depict regions of forcing for ascent. It was calculated using the Petterssen frontogenesis equation (Petterssen 1936; 1956, pp. 200–201), which describes the Lagrangian rate of change of the magnitude of the horizontal potential temperature gradient. The quantity was calculated for an isobaric surface as [adapted from Keyser et al. 1988, his Eqs. (1.1)–(1.4)]:

$$\frac{d}{dt_p}\left|\nabla_p\theta\right| = -\frac{1}{2}\left|\nabla_p\theta\right|\left(D - E\cos 2\beta\right) \qquad (3)$$

where,

$$E = \left(E_{st}^2 + E_{sh}^2\right)^{1/2}. \qquad (4)$$

$D$ and $E$ represent the divergence and the total deformation, respectively, evaluated on an isobaric surface. In Eq. (4), $E_{st}$ and $E_{sh}$ denote the stretching deformation and the shearing deformation, respectively, where $E_{st} = \partial u/\partial x - \partial v/\partial y$ and $E_{sh} = \partial v/\partial x + \partial u/\partial y$. $\beta$ is the difference between the local orientations of the horizontal axis of dilatation, $\delta$, and the isentropes, $\alpha$, where:

$$\tan\alpha = -\frac{\partial\theta}{\partial x}\left(\frac{\partial\theta}{\partial y}\right)^{-1} \qquad (5)$$

and

$$\tan 2\delta = E_{sh}/E_{st}. \qquad (6)$$

Eq. (1) indicates that frontogenesis occurs in the presence of convergence ($D < 0$) and when $\beta < 45°$.

As a link back to the **Q**-vector diagnostic [Eqs. (1), (2)], following the geostrophic flow on an isobaric surface, the Petterssen equation can be written as [adapted from

Martin 2006a, his Eq. (7.13b)]:

$$\frac{d}{dt_g}\left|\nabla_p\theta\right| = \left(\frac{1}{f_o\gamma}\right)\left(\frac{\vec{Q}\cdot\nabla_p\theta}{\left|\nabla_p\theta\right|}\right), \tag{7}$$

where $d/dt_g = \partial/\partial t + \vec{V}_g \cdot \nabla_p$ . This expression indicates that frontogenesis occurs where $\vec{Q}$ points across the isentropes from cold to warm air.

*2.5.3 Moisture contributions*

A fundamental ingredient for PRE development is the transport of deep moisture from the TC environment to the region of the PRE. To evaluate this transport, the horizontal moisture flux was calculated as:

$$MF = q\vec{V} \tag{8}$$

and subsequently integrated vertically using the formulation:

$$VIMF = -\int_{p_o}^{p}\left(q\vec{V}\right)\frac{dp}{g}, \tag{9}$$

In (8) and (9), $q$ is the specific humidity, $\vec{V}$ is the horizontal wind, $g$ is the acceleration due to gravity, and $p_o$ is 1000 hPa. In addition, following Doswell et al. (1998), the vertically integrated moisture flux divergence was calculated using:

$$VIMFD = -\int_{p_o}^{p}\nabla\cdot\left(q\vec{V}\right)\frac{dp}{g} \tag{10}$$

in order to identify mesoscale regions favorable for deep moist convection. Regions where $VIMFD < 0$ are indicative of a net accumulation of moisture within a column. In order to determine the source regions of moist air parcels entering the PRE region, kinematic backward air parcel trajectories ending at various levels in the PRE region were calculated from the 1° GFS analysis dataset. The trajectory calculation employs 1-h

linear interpolation between 6-h analysis times, with the three-dimensional velocity components linearly interpolated in space and time to the parcel position.

*2.5.4 Impact of diabatic heating on the upper-tropospheric flow*

An important dynamical consideration for PREs is the impact of diabatically generated anticyclonic outflow resulting from latent heat release associated with both TC and PRE on the upper-tropospheric flow. This impact was diagnosed by analyzing the evolution of Ertel PV on constant pressure surfaces, evaluated as:

$$\mathrm{PV} = -g\frac{\partial\theta}{\partial p}\left(f + \frac{\partial v}{\partial x} - \frac{\partial u}{\partial y}\right) + g\left(\frac{\partial v}{\partial p}\frac{\partial\theta}{\partial x} - \frac{\partial u}{\partial p}\frac{\partial\theta}{\partial y}\right). \qquad (11)$$

The particular utility of this quantity arises from the fact that it is conserved following the flow in the absence of diabatic and frictional effects, a fact which allows for the assessment of PV nonconservation in regions of diabatic heating associated with convection (e.g., Brennan et al. 2008). Specifically, the Lagrangian rate of change of PV can be approximated as [adapted from Martin 2006a, his Eq. (9.22)]:

$$\frac{d}{dt}(PV) \approx -g(\zeta + f)\frac{\partial\dot{\theta}}{\partial p}, \qquad (12)$$

where $\dot{\theta}$ is the diabatic heating rate. Eq. (12) indicates that regions where $\dot{\theta}$ decreases (increases) with decreasing pressure correspond to regions of decreasing (increasing) PV. We therefore apply the interpretation of Eq. (12) to qualitatively determine regions of diabatic heating in regions where it is evident that PV is not conserved. As a supplementary tool, the irrotational component of the horizontal wind was calculated in order to examine the influence of the upper-tropospheric divergent outflow associated with regions of convection on the distribution of PV. This vector quantity was calculated

from the 1° GFS global analyses as:

$$\vec{V}_{\chi} = \nabla_p \chi, \tag{13}$$

where $\chi$ is the velocity potential, given by:

$$\nabla_p^2 \chi = \frac{\partial u}{\partial x} + \frac{\partial v}{\partial y}. \tag{14}$$

TABLE I: All PREs associated with Atlantic Basin TCs during 1988–2008. Listed are key details for each PRE: initiation time, geographic area, precipitation amounts, location relative to the TC track, and synoptic category. The numbers in the sixth column correspond to the numbers in Fig. 3.4. The initial PREs associated with the TCs in bold were those used for the composites. The synoptic categories are abbreviated as in the text; the UC designation refers to PREs that were unclassifiable. For the positions relative to the TC track, LOT refers to left of track, ROT refers to right of track, and AT refers to along track.

| **TC (Year)** | **PRE Initiation Time** | **Geographic Area** | **Precipitation Amount (mm)** | **Location Relative to TC Track** | **Synoptic Category (Number)** |
|---|---|---|---|---|---|
| **Chris (1988)** | 2100 UTC 28 Aug | PA/NY | 50–75 | LOT | SJ (1) |
| **Florence (1988)** | 1200 UTC 7 Sep | FL/GA/SC/NC | 50–75 | ROT | DC (1) |
| Gilbert (1988) | 1200 UTC 16 Sep | MS/AL/TN | 50–75 | ROT | UC (1) |
| Hugo (1989) | 1800 UTC 19 Sep | PA/NY/NJ/VA | 100–150 | ROT | UC (2) |
| **Marco (1990)** | 1200 UTC 10 Oct | GA/SC/NC | 200–350 | AT | SJ (2) |
| **Andrew (1992)** | 0600 UTC 26 Aug | IN/IL | 30–50 | LOT | SJ (3) |
| **Arlene (1993)** | 1200 UTC 18 Jun | KS/NE/IA | 50–75 | ROT | JR (1) |
| **Beryl (1994)** | 1200 UTC 15 Aug | GA/SC/NC/VA | 50–100 | AT | DC (2) |
| **Dean (1995)** | 0000 UTC 1 Aug | OK/KS/MO | 50–80 | ROT | SJ (4) |
| **Erin (1995)** | 0600 UTC 4 Aug | MO/IL | 40–60 | LOT | JR (2) |
| | 1500 UTC 4 Aug | OH/PA/NY | 40–60 | LOT | JR |
| **Opal (1995)** | 0000 UTC 3 Oct | TX/LA/AL/GA/NC/VA | 100–200 | AT | SJ (5) |
| Fran (1996) | 0500 UTC 4 Sep | NC | 75–100 | AT | UC (3) |
| **Danny (1997)** | 0000 UTC 23 Jul | NC | 100–150 | AT | DC (3) |
| | 0500 UTC 24 Jul | NJ/PA | 50–75 | LOT | DC |
| **Bonnie (1998)** | 0400 UTC 26 Aug | PA/NY/NJ/CT | 25–50 | LOT | SJ (6) |
| | 1200 UTC 26 Aug | NY/NJ/CT (off coast) | N/A | LOT | SJ |
| | 0300 UTC 27 Aug | NY/NJ/CT (off coast) | N/A | LOT | SJ |

TABLE I (cont.)

| TC (Year) | PRE Initiation Time | Geographic Area | Precipitation Amount (mm) | Location Relative to TC Track | Synoptic Category (Number) |
|---|---|---|---|---|---|
| **Bonnie (1998)** | 0400 UTC 26 Aug | PA/NY/NJ/CT | 25–50 | LOT | SJ (6) |
| | 1200 UTC 26 Aug | NY/NJ/CT (off coast) | N/A | LOT | SJ |
| | 0300 UTC 27 Aug | NY/NJ/CT (off coast) | N/A | LOT | SJ |
| Bret (1999) | 2000 UTC 23 Aug | NM/TX | 25–40 | ROT | UC (4) |
| **Floyd (1999)** | 1800 UTC 14 Sep | NC/NC/VA | 75–100 | LOT | SJ (7) |
| **Harvey (1999)** | 1600 UTC 20 Sep | GA/SC/NC | 50–70 | LOT | SJ (8) |
| **Helene (2000)** | 1700 UTC 20 Sep | GA/SC | 25–50 | AT | SJ (9) |
| | 0500 UTC 21 Sep | GA/SC | 50–75 | LOT | SJ |
| **Lili (2002)** | 1200 UTC 2 Oct | OK/KS/NE/IA | 100–170 | LOT | JR (3) |
| **Grace (2003)** | 0000 UTC 31 Aug | OK/KS/MO/IL/IN | 100–225 | LOT | JR (4) |
| Isabel (2003) | 1600 UTC 14 Sep | NC | N/A | AT | UC (5) |
| | 0700 UTC 15 Sep | PA/MD/NJ | 75–100 | ROT | UC |
| **Alex (2004)** | 1900 UTC 1 Aug | VA | 50–110 | LOT | DC (4) |
| | 1900 UTC 2 Aug | VA | 100–130 | LOT | DC |
| **Bonnie (2004)** | 0000 UTC 11 Aug | FL | 50–80 | AT | SJ (10) |
| | 0500 UTC 12 Aug | GA/NC/SC | 50–90 | LOT | SJ |
| | 1700 UTC 12 Aug | PA/NY | 125–150 | LOT | SJ |
| | 0300 UTC 13 Aug | ME | 50–75 | LOT | SJ |
| **Charley (2004)** | 0700 UTC 13 Aug | FL/GA/SC | 40–80 | LOT | SJ (11) |
| | 2100 UTC 13 Aug | NC/VA | 40–80 | LOT | SJ |
| **Gaston (2004)** | 1100 UTC 30 Aug | NY | 40–60 | LOT | SJ (12) |
| | 2000 UTC 30 Aug | NY/VT/NH/ME | 50–90 | LOT | SJ |
| **Frances (2004)** | 0400 UTC 8 Sep | NY/CT | 80–120 | ROT | SJ (13) |
| **Jeanne (2004)** | 0400 UTC 28 Sep | PA/NY/MA | 50–90 | LOT | DC (5) |
| **Matthew (2004)** | 1900 UTC 7 Oct | AS/MO/LA/TX | 150–225 | AT | SJ (14) |

TABLE I (cont.)

| TC (Year) | PRE Initiation Time | Geographic Area | Precipitation Amount (mm) | Location Relative to TC Track | Synoptic Category (Number) |
|---|---|---|---|---|---|
| **Dennis (2005)** | 1600 UTC 9 Jul | AL/GA/SC | 50–75 | AT | DC (6) |
| **Irene (2005)** | 0000 UTC 15 Aug | NY/CT/RI | 75–100 | LOT | SJ (15) |
| **Katrina (2005)** | 1800 UTC 28 Aug | KY/IN/OH | 75–100 | AT | DC (7) |
| | 0700 UTC 29 Aug | KY | 150–200 | AT | DC |
| | 0000 UTC 30 Aug | NY/PA | 50–75 | ROT | DC |
| | 0000 UTC 30 Aug | ME | 100–150 | ROT | DC |
| | 0000 UTC 31 Aug | MA/CT/ME | 75–125 | ROT | DC |
| **Ophelia (2005)** | 0300 UTC 15 Sep | NY/VT/NH | 30–50 | LOT | SJ (16) |
| | 1000 UTC 15 Sep | NY/CT/RI/MA | 50–80 | LOT | SJ |
| **Rita (2005)** | 2200 UTC 24 Sep | NE/IA/MN/WI | 100–200 | LOT | JR (5) |
| **Wilma (2005)** | 1800 UTC 23 Oct | GA/SC/NC | 75–125 | LOT | SJ (17) |
| **Alberto (2006)** | 1800 UTC 12 June | NC/SC | 50–90 | AT | DC (8) |
| **Ernesto (2006)** | 1800 UTC 30 Aug | NC/VA | 75–110 | AT | DC (9) |
| | 1200 UTC 31 Aug | NC/TN/KY/WV | 75–100 | LOT | DC |
| **Erin (2007)** | 2100 UTC 18 Aug | MN/IA/WI | 100–350 | LOT | JR (6) |
| **Ike (2008)** | 0000 UTC 12 Sep | OK/KS/MO/IL/IN | 100–200 | LOT | JR (7) |

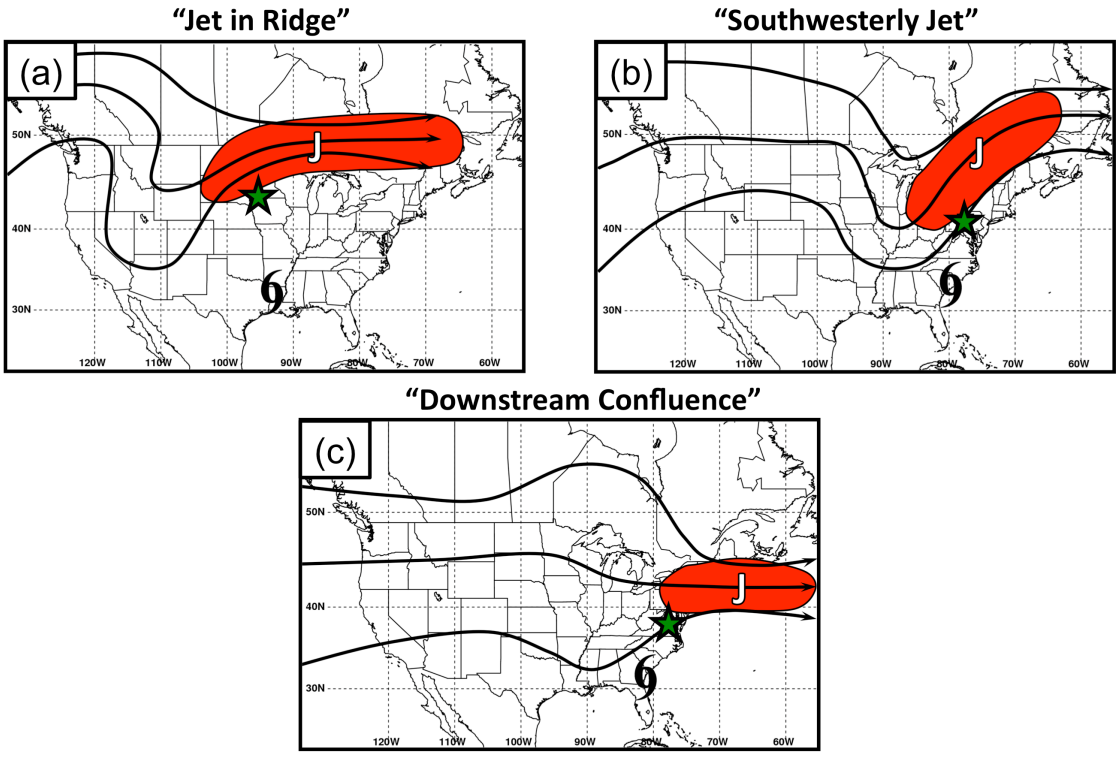


Figure 2.1: Schematic illustration of the 200-hPa flow configuration for the three synoptic patterns associated with PREs: (a) JR, (b) SJ, and (c) DC. The PRE and TC locations are marked with the green star and the tropical storm symbol, respectively. Schematic streamlines are shown in black, and the jet streak is indicated by the red shaded area, with the "J" symbol marking the location of maximum wind speed.

## 3. Climatology of PREs during 1988–2008

### 3.1 Overview

A total of 56 PREs associated with 38 Atlantic basin TCs were identified for the 1988–2008 period. The distribution of PREs and TCs, stratified by synoptic category (Fig. 3.1), indicates that SJ category PREs occurred most frequently, with 26 PREs associated with 17 TCs, while there were 16 DC category PREs associated with 9 TCs and 8 JR category PREs associated with 7 TCs. Additionally, 6 PREs associated with 5 TCs were unclassifiable (UC) based upon the stratification scheme used in this study. The ratios of PREs to TCs for the SJ and DC categories of ~1.5 and ~1.8, respectively, were large compared to that for the JR category (~1.1). It is, however, important to note that only a subset of the TCs associated with the SJ and DC categories (6 for the SJ category and 4 for the DC pattern) produced multiple PREs. For example, Table I shows that 5 PREs developed in advance of TC Katrina (2005; DC pattern), and 4 PREs developed in advance of TC Bonnie (2004; SJ pattern).

### 3.2 Monthly distribution

The monthly frequency distributions for the genesis of all Atlantic basin TCs and all PRE-producing TCs (PPTCs) during 1988–2008 (Fig. 3.2a) indicates that PPTCs most frequently formed in August and September, consistent with preferential genesis months of all Atlantic basin TCs. The genesis of PPTCs, however, was more concentrated in August and September than the genesis of all Atlantic basin TCs, with approximately 39% and 34% of PPTCs forming during the two months, respectively, versus approximately 27% and 31% for all Atlantic basin TCs. The monthly distribution of

PPTCs separated by synoptic category and binned by the PRE genesis month shows that PPTCs occurred with greatest frequency in August and September for each of the categories (Fig. 3.2b). PPTCs associated with the SJ category tended to occur in the latter part of the season, with none occurring prior to August, whereas PPTCs associated with the DC pattern occurred more frequently in the earlier part of the season, prior to September. For PPTCs in the JR pattern, there was no apparent skewness in the monthly frequency distribution.

## 3.3 Geographic distribution and favorable TC tracks

The geographic locations of the initial PRE for each TC and the associated TC tracks are shown in Fig. 3.3. The TCs associated with JR category PREs tended to make landfall along the western and central Gulf of Mexico coastline and either recurved over the central U.S. or dissipated shortly after landfall (Fig. 3.3a). The JR PREs all developed in the Midwest either while the parent TC moved northwestward over the Gulf of Mexico or as the parent TC recurved over the south-central U.S. (Fig. 3.3a).

For the SJ pattern, with the exception of TC Andrew (1992; 3 in Fig. 3.3b), TC Dean (1995; 4 in Fig. 3.3b), and TC Matthew (2004; 14 in Fig. 3.3c), TCs made landfall along the coastline of the eastern Gulf of Mexico or along the southeastern U.S. coastline and recurved over the southeastern U.S., along the East Coast, or over the eastern Gulf of Mexico (Figs. 3.3b,c). With the exception of 4 PREs (3, 4, 5, 14 in Figs. 3.3b,c) that developed in the central portion of the U.S., the SJ PREs generally developed in the eastern U.S. during or just after TC recurvature (Figs. 3.3b,c).

The DC category was generally associated with less pronounced TC recurvature than the TCs associated with the JR and SJ categories and had TC tracks that meandered (Fig. 3.3d), both attributes likely owing to the lack of a strong upstream trough and associated strong westerly steering flow in the environments of DC category PREs. The TCs associated with the DC category tended to make landfall along the central and eastern Gulf of Mexico coastline, and PREs preferentially developed in the southeastern U.S. (Fig. 3.3d).

Three of the UC PREs associated with TC Hugo (1989; 2 in Fig. 3.3e), TC Fran (1996; 3 in Fig. 3.3e), and TC Isabel (2003; 5 in Fig. 3.3e), respectively, developed along the Mid-Atlantic coast of the U.S. as the associated parent TCs moved northwestward over the Atlantic Ocean (Fig. 3.3e). These three TCs eventually made landfall along the southeastern U.S. coast and moved northwestward into the Ohio River Valley. The other two TCs associated with UC PREs, TC Gilbert (1988; 1 in Fig. 3.3e) and TC Bret (1999; 4 in Fig. 3.3e), made landfall along the western coastline of the Gulf of Mexico and produced PREs over Alabama and northwestern Texas, respectively (Fig. 3.3e).

A critical factor for forecasting the impact of PREs is the location of the PRE relative to the total observed track of the parent TC. This factor is important for determining if the TC will pass over the area previously affected by the PRE, a situation that poses a substantial risk for flooding (M. Jurewicz 2009, personal communication). Shown in Fig. 3.4, the relative frequency distribution of LOT, ROT, and AT PREs for each synoptic category indicates that the majority of PREs were LOT. Nearly 88% of JR PREs and 74% of SJ PREs were LOT, while the DC category exhibited a more even distribution with 25% of PREs occurring ROT, 31% occurring LOT, and 44% occurring

AT. Additionally, 2 of the 6 UC PREs and 20% of all SJ PREs were AT, while no AT PREs occurred in the JR pattern. The preference for PRE development to the left of, right of, or along the TC track for each category is likely a function of the environmental flow configuration within which the TC and PRE are embedded. Possible dynamical mechanisms to account for TC track-relative PRE positions will later be elucidated through composite analysis and case studies.

### 3.4 Other statistical properties

Box and whisker plots of the separation distance between the PRE and parent TC, PRE longevity, maximum PRE rainfall, and the lag time between PRE initiation and the passage of the TC over the latitude at which the PRE was intiated are shown in Fig. 3.5 for the three synoptic categories and for all PREs. The median separation distance for all PREs was 950 km, with maximum and minimum values of 2160 km and 415 km, respectively, both of which were associated with DC PREs (Fig. 3.5a). JR PREs were generally characterized by the largest separation distances, with a median value of 1100 km compared with 930 km and 790 km for the SJ and DC categories, respectively (Fig. 3.5a). For all PREs, the median longevity was 16 h, with the longest-lived PREs (48 h) occurring in the JR and SJ categories and the shortest-lived PRE (8 h) occurring in the SJ category (Fig. 3.5b). The JR category had the greatest median longevity (24 h), substantially larger than that for the SJ and the DC categories (15.5 h and 13.5, respectively; Fig. 3.5b). As indicated in Fig. 3.5c, the maximum rainfall totals produced by PREs ranged from 40 mm (SJ pattern) to 300 mm (JR pattern), and the highest rainfall totals were typically produced by JR PREs (median value of 180 mm). The SJ and DC

categories generally produced considerably smaller maximum rainfall totals, with median values for the two categories of 100 and 80 mm, respectively (Fig. 3.5c).

When calculating the lag time between the PRE initiation and the passage of the TC based upon the NHC Best Track dataset, it was apparent that for only a fraction of all PREs (39 out of 56) did the parent TC track extend through the latitude at which the PRE was initiated. Furthermore, the TC passed the latitude of PRE initiation for only 1 out of 8 JR PREs. Accordingly, box plots are only shown in Fig. 3.5d for the SJ and DC categories and for all PREs in the database. For the 39 PREs for which the NHC Best Track dataset indicated that the parent TC passed through the latitude of the PRE, the lag time ranged from 7 h (DC pattern) to 104 h (JR pattern; not shown) with a median value for all PREs of 51 h. The SJ category had a higher median lag time (54 h) than the DC category (45.5) and exhibited less spread (Fig. 3.5d).

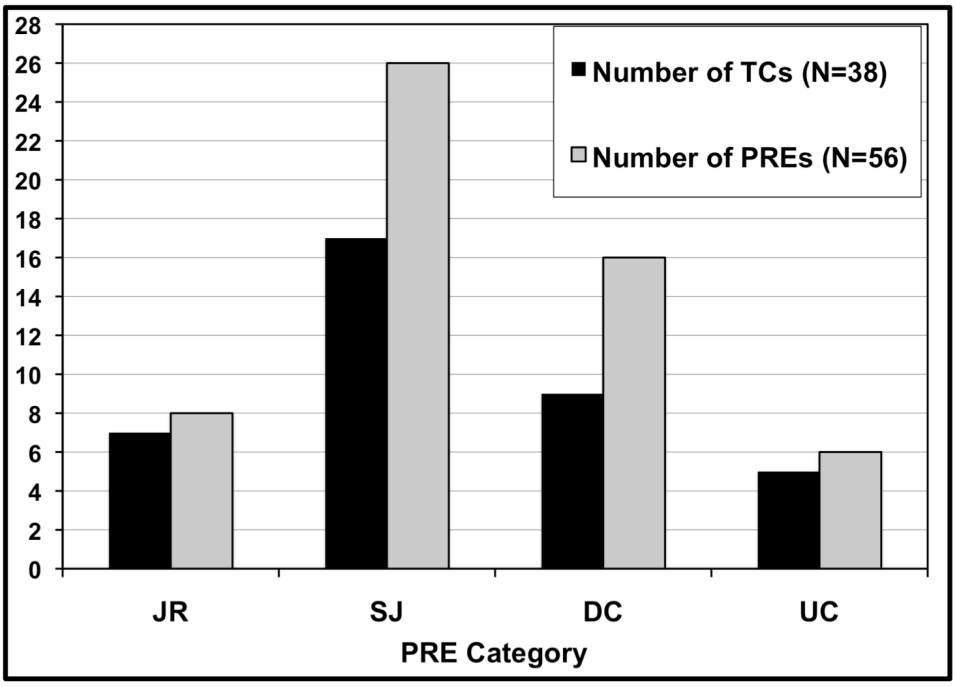


Figure 3.1: The distribution of all PREs and PPTCs during 1988–2008 stratified by synoptic pattern. The gray bars indicate the number of PREs for each pattern, whereas the black bars indicate the number of TCs.

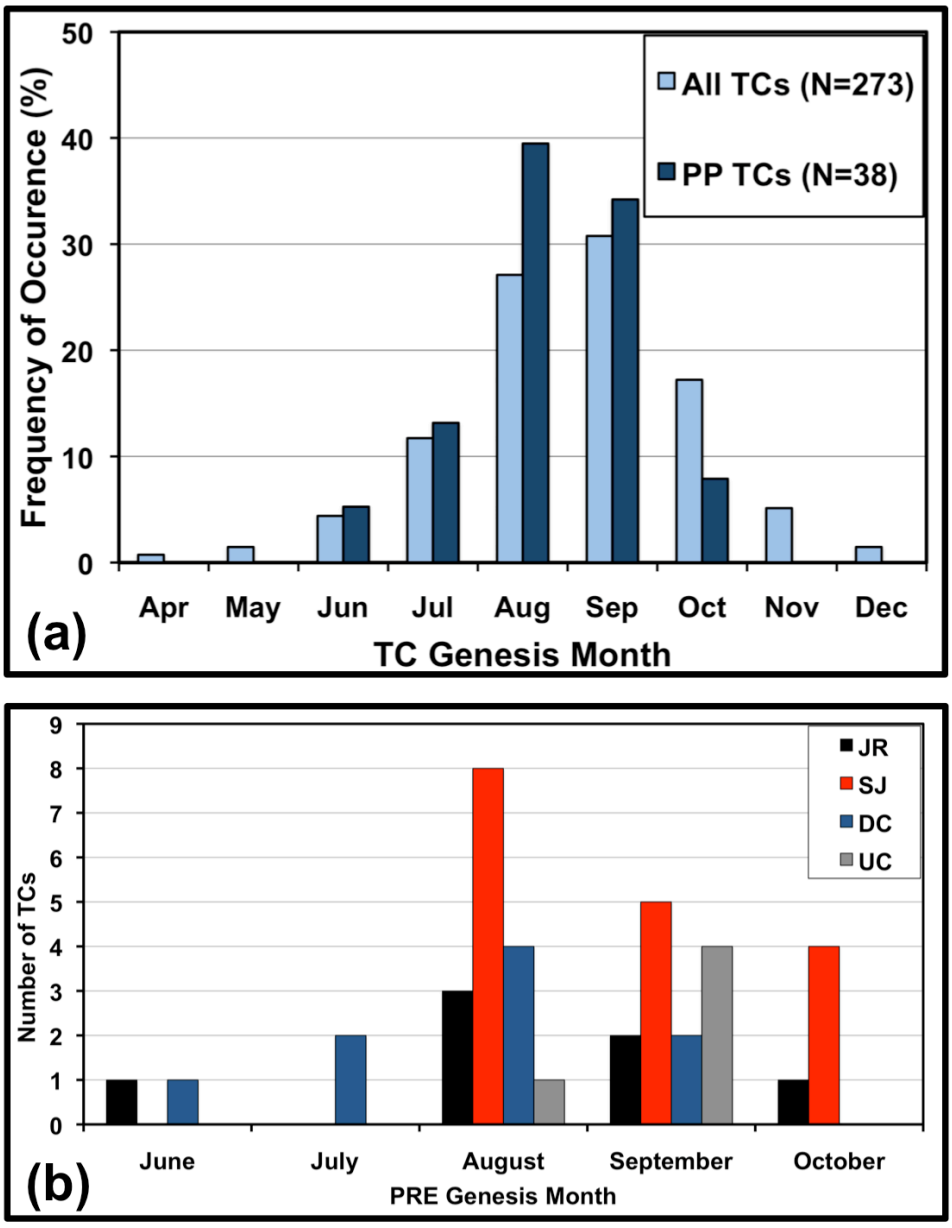


Figure 3.2: (a) Monthly relative frequency distribution of the genesis of all Atlantic basin TCs (light blue) and all PPTCs (dark blue) during 1988–2008, and (b) monthly absolute frequency distribution of PPTCs during 1988–2008 binned by PRE genesis month and separated by synoptic pattern. In panel (b), the bars are colored according to the legend.

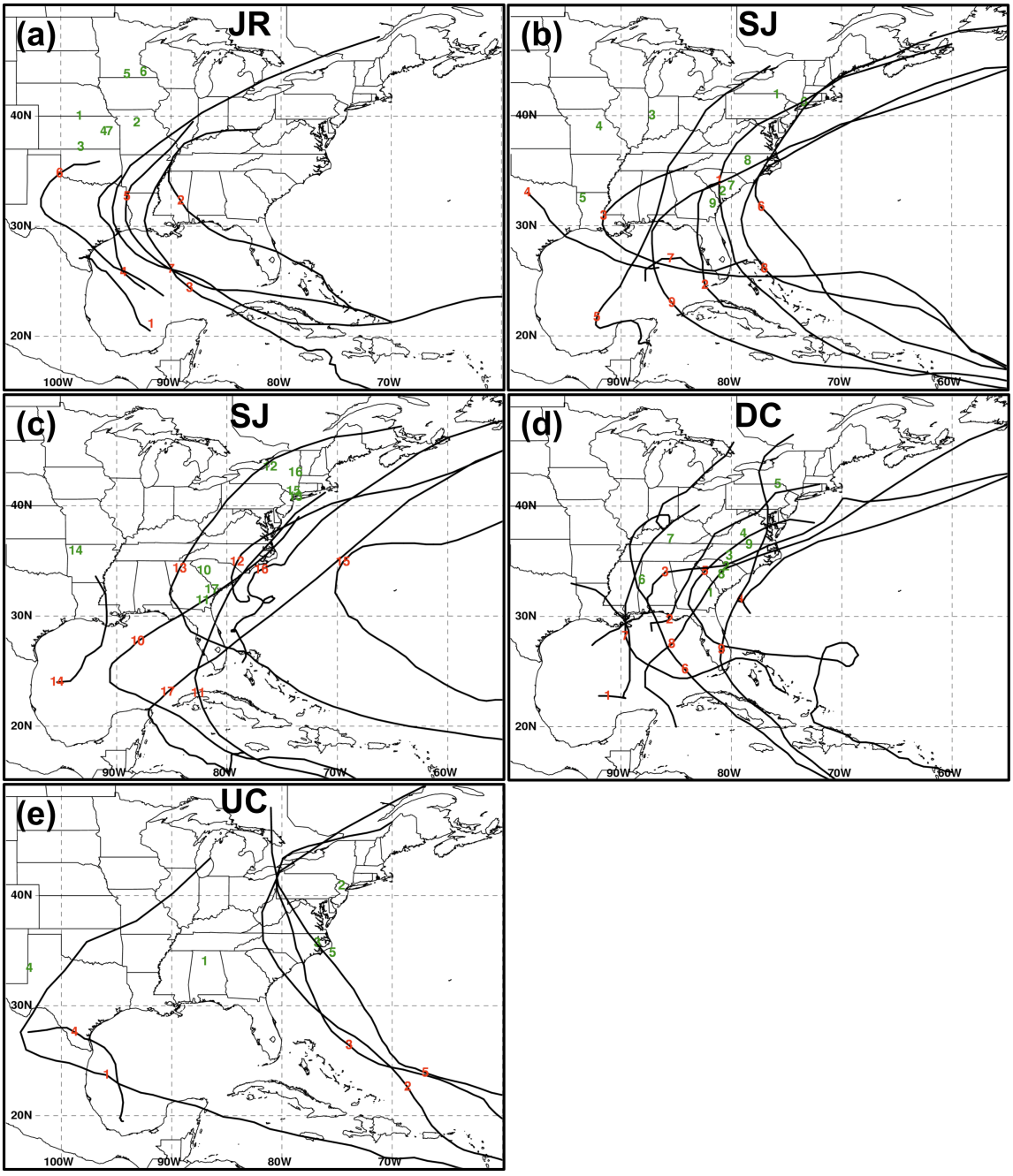


Figure 3.3: Plots of TC tracks along with the geographic locations of PREs (green numbers) and associated TCs (red numbers) at the time of PRE initiation for (a) the JR pattern, (b,c) the SJ pattern, (d) the DC pattern, and (e) UC PREs. In each of the panels, the PREs and parent TCs are numbered in chronological order, with each number corresponding to a PRE–TC pair. The numbers corresponding to each pair can be found in the last column of Table I. Only the location of initial PRE for each TC is plotted.

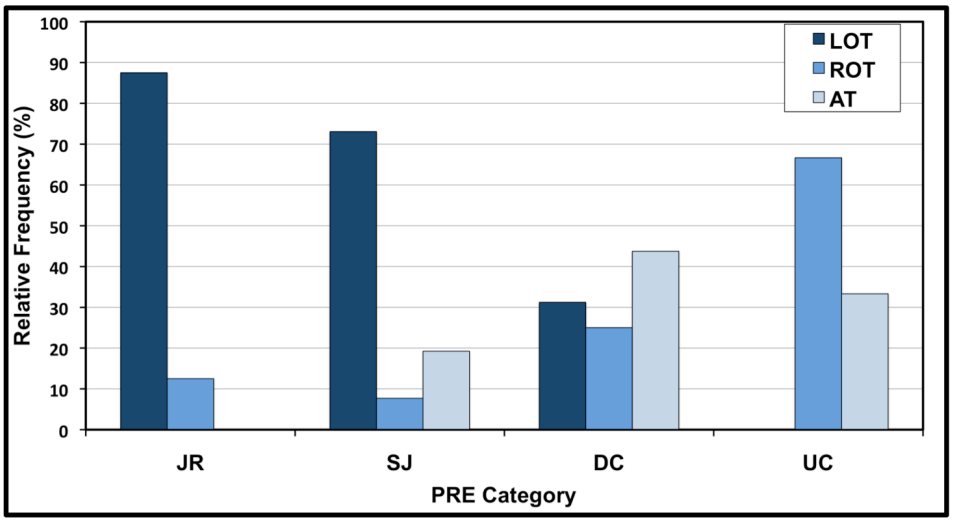


Figure 3.4: Relative frequency distribution of LOT (dark blue), ROT (sky blue), and AT (light blue) PREs for each synoptic pattern.

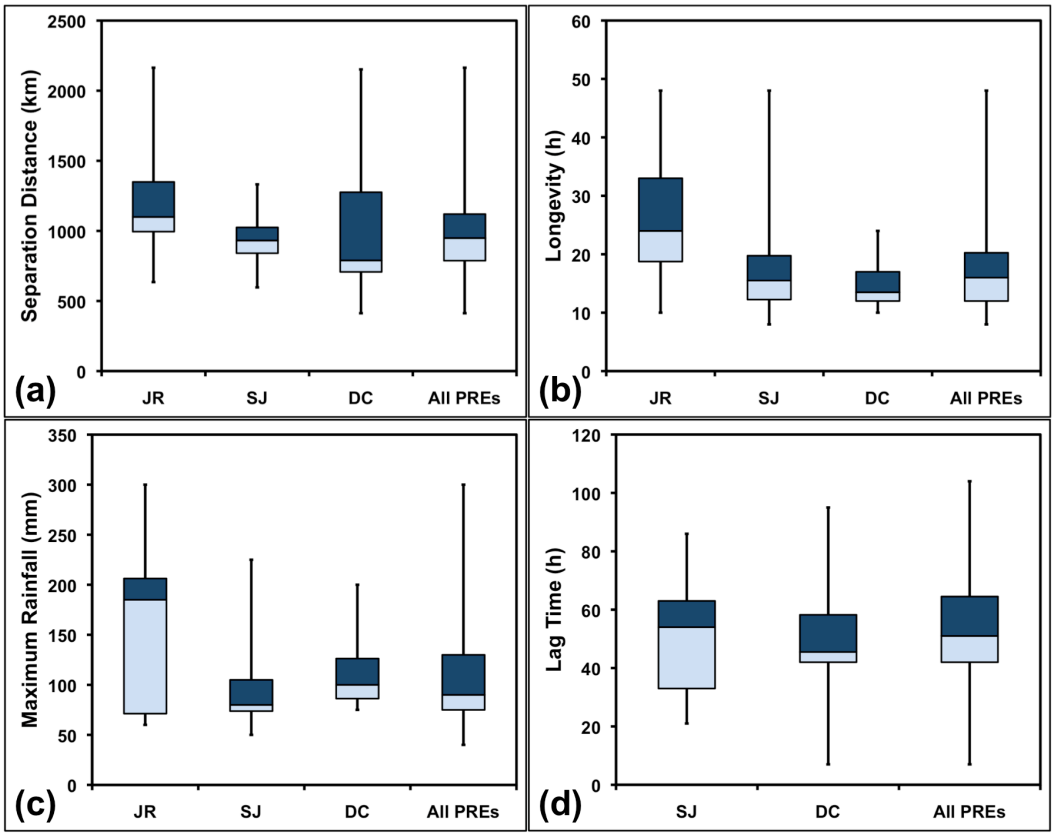


Figure 3.5: Box and whisker plots for each synoptic category and for all PREs showing (a) separation distance between the TC and PRE, (b) PRE longevity, (c) maximum PRE rainfall, and (d) lag time between PRE initiation and the passage of the TC over the latitude of PRE initiation. The whiskers indicate the maximum and minimum values, the top (bottom) of the box marks the third (first) quartile, and the line separating the light and dark blue denotes the median.

## 4. PRE-relative composite analysis

In order to depict the synoptic-scale environments within which PREs develop, PRE-relative composites are now presented for each of the three PRE categories. In the interest of brevity, composites are shown for T−12 h h, T−0 h h, and T+12 h h in order to elucidate the synoptic-scale flow conditions prior to and during the PRE. The objective of the following analysis is to assess: dynamical mechanisms for forcing of ascent in the PRE region, the transport of TC moisture to the PRE region, and the impact of diabatic heating associated with the PRE and the TC on the upper-tropospheric flow. To accomplish this objective, plots displaying the evolution of the synoptic-scale environment on the 200-hPa and 925-hPa surfaces, respectively representing the upper and lower troposphere, are shown for each PRE category.

### 4.1 JR category

#### *4.1.1 Synoptic-scale evolution*

The composite evolution for the JR category is shown in Fig. 4.1. The antecedent 200-hPa flow, depicted at T−12 h, is dominated by a broad ridge that extends to the northeast of the composite TC location and a positively tilted trough located upstream (Fig. 4.1a). An anticyclonically curved 200-hPa jet streak is situated on the poleward flank of the ridge, with its core positioned well downstream of the trough axis (Fig. 4.1a). At T−12 h, a southward advancing 925-hPa baroclinic zone with an attendant region of frontogenesis is located to the northwest of the PRE initiation location (Fig. 4.1b). A localized region of PW values > 44 mm is evident ahead of the baroclinic zone, while the

TC and its attendant moisture plume, with PW values > 44 mm, are situated on the southwestern flank of a 925-hPa anticyclone (Fig. 4.1b).

Between T−12 h and T−0 h, the TC moves northwestward in the direction of the southeasterly 925-hPa geostrophic flow that extends on the western flank of the anticyclone from the eastern side of the TC circulation into the PRE initiation region (Figs. 4.1d,f). This southeasterly geostrophic flow contributes to the poleward progression of the TC moisture plume (PW values > 44 mm) into the PRE initiation region (Fig. 4.1d). In the presence of the TC moisture plume, the PRE is intiated within the equatorward entrance region of the anticyclonically curved 200-hPa jet streak and along the zonally oriented 925-hPa baroclinic zone (Figs. 4.1c,d). Southeasterly 925-hPa geostrophic flow directed perpendicular to the baroclinic zone within the PRE initiation region contributes to warm-air advection and frontogenesis over the PRE initiation region (Figs. 4.1d).

From T−0 h to T+12 h, as frontogenesis and warm-air advection persist along the baroclinic zone (Figs. 4.1d,f), additional forcing for ascent is indicated by a region of divergence extending poleard and eastward of the PRE initiation location within the equatorward entrance region of the 200-hPa jet streak (Figs. 4.1c,e). At T+12 h, the TC moisture plume continues to extend into the PRE initiation region as the TC moves toward the northwest on the western flank of the 925-hPa anticyclone (Fig. 4.1f).

### *4.1.2 Impact of diabatic heating on the upper-tropospheric flow*

At T−12 h, a plume of low 250–200-hPa PV air extends poleward of the PRE initiation location toward the axis of the 200-hPa jet streak in connection with 200-hPa

irrotational wind vectors directed outward from a region of 700-hPa ascent centered just west of the PRE initiation location (Fig. 4.2a). This configuration of the irrotational winds is likely a reflection of divergent outflow associated with antecedent precipitation occurring prior to PRE initiation within the equatorward entrance region of the 200-hPa jet streak. At T−0 h and T+12 h, low-PV air, likely linked to diabatic heating associated with the PRE, extends from the PRE initiation region along the axis of the jet streak and contributes to a strengthened PV gradient within the jet streak (Figs. 4.2b,c). In association with the increased PV gradient, wind speeds within the core of the jet streak increase from 45–50 m $s^{-1}$ at T−12 h to > 50 m $s^{-1}$ at T−0 h and T+12 h (Figs. 4.2a–c).

Additionally at T−0 h and T+12 h, irrotational wind vectors, directed radially outward from the region of 700-hPa ascent overlying the PRE initiation location, point across PV contours from the region of low PV associated with the PRE toward the axis of high PV associated with the upstream trough (Figs. 4.2b,c). Within this configuration, the irrotational wind, which includes the diabatically driven divergent outflow associated with the PRE, acts to advect low-PV air poleward and contributes to the strengthening of PV gradients along the axis of the jet streak. The strengthened PV gradients are consistent with both the increase in maximum wind speeds and the strengthening of along-flow wind speed gradients within the jet entrance region at T−0 h and T+12 h (Figs. 4.2b, c). These flow changes within the jet streak are concomitant with the strengthening of 200-hPa divergence (Figs. 4.1a,c,e) and 700-hPa ascent (Figs. 4.2b,c) over the PRE initiation region between T−0 h and T+12 h.

## 4.2 SJ category

### *4.2.1 Synoptic-scale evolution*

The composite evolution for the SJ category is shown in Fig. 4.3. At T−12 h, a 200-hPa trough approaches the PRE initiation region from the west, while a ridge extends poleward and eastward of the northeastward-moving composite TC (Fig. 4.3a). A southwesterly 200-hPa jet streak is situated poleward of the PRE initiation location in association with the strong geopotential height gradient that forms between the trough and the ridge (Fig. 4.3a). The TC circulation approaches a 925-hPa baroclinic zone accompanying the advancing trough, while a plume of deep moisture (PW values > 40 mm) extends poleward from the TC in association with strong southeasterly 925-hPa geostrophic flow on the eastern flank of the TC circulation (Fig. 4.3b).

The PRE is initiated beneath a region of divergence within the equatorward entrance region of the 200-hPa jet streak downstream of the approaching trough axis (Fig. 4.3c). Concurrently, at 925 hPa the circulation of the northeastward-moving TC impinges upon the approaching baroclinic zone, establishing warm-air advection and frontogenesis over the PRE initiation region (Fig. 4.3d). Heavy rainfall is favored in the PRE initiation region as the TC moisture plume, with PW values > 44 mm, is transported poleward toward the region of implied lifting associated with low-level frontogenesis and upper-level divergence (Figs. 4.3c,d).

At 200 hPa, the continued eastward progression of the trough between T−0 h and T+12 h toward the slow-moving ridge extending to the northeast of the TC coincides with the strengthening of the southwesterly jet streak and an increase in divergence over the TC and the PRE initiation location (Figs. 4.3c,e). As the TC moves northeastward

between T−0 h and T+12 h, its circulation continues to interact with the 925-hPa baroclinic zone, resulting in strengthened frontogenesis over the PRE initiation region (Fig. 4.3f). Deep moisture, with PW values > 44 mm, continues to be transported into the PRE environment on the eastern flank of the TC circulation (Fig. 4.3f).

*4.2.2 Impact of diabatic heating on the upper-tropospheric flow*

At T−12 h, the 200-hPa jet streak is positioned poleward of the PRE initiation location in association with the 250–200-hPa PV gradient between the axis of high PV associated with the approaching trough and the low-PV outflow extending northeastward from the TC (Fig. 4.4a). The jet streak strengthens between T−12 h and T+12 h as the high-PV air associated with the trough advances to the east, and a plume of low-PV air, likely associated with diabatically driven outflow associated with the TC and PRE, extends poleward and eastward from the TC and the PRE initiation location along the axis of the jet streak (Figs. 4.4a–c).

Substantial divergent outflow associated with the PRE and TC is indicated at T−0 h and T+12 h by 200-hPa irrotational wind vectors that emanate outward from the maximum of 700-hPa ascent overlying both the TC and the PRE initiation location (Figs. 4.4b,c). The poleward and westward advection by the irrotational wind of low-PV air associated with the PRE and the TC toward the axis of high PV associated with the approaching trough leads to an increased PV gradient along the axis of the jet streak between T−0 h and T+12 h (Figs. 4.4b,c). The increased PV gradient contributes to strengthened maximum wind speeds (from 40–45 m $s^{-1}$ at T−0 h to 45–50 m $s^{-1}$ at T+12 h) and strengthened along-flow wind speed gradients within the jet entrance region (Figs.

4.4b,c). These flow changes associated with the jet streak between T−0 h and T+12 h coincide with the enhancement of 200-hPa divergence (Figs. 4.3a,c,e) and with the maintenance of 700-hPa ascent (Figs. 4.4a–c) over the TC and the PRE initiation location beneath the equatorward entrance region of the jet streak.

## 4.3 DC category

### *4.3.1 Synoptic-scale evolution*

The composite evolution for the DC category is shown in Fig. 4.5. At T−12 h, the 200-hPa flow configuration is dominated by a region of geostrophic confluence downstream of the PRE initiation location, with a jet streak situated between an eastward moving downstream trough and a downstream ridge extending northeastward from the composite TC location (Fig. 4.5a). Compared with the JR and SJ category composites, the 200-hPa geostrophic flow upstream of the TC is weaker, owing to the lack of a strong upstream trough. At 925-hPa, a trough is situated poleward and eastward of the PRE initiation location at T−12 h, while a zonally oriented baroclinic zone, positioned poleward of the PRE initiation location, trails behind this trough (Fig. 4.5b). A plume of moisture (PW values > 36 mm) extends from the TC location along the baroclinic zone toward the axis of the 925-hPa trough (Fig. 4.5b).

The PRE is initiated within the equatorward entrance region of the 200-hPa jet streak, downstream of a weak 200-hPa short-wave trough, and along the 925-hPa baroclinic zone, while a plume of moisture, characterized by PW values > 40 mm, advances poleward and eastward from the TC (Figs. 4.5c,d). Warm-air advection and frontogenesis at 925 hPa over the PRE initiation region are evident at T−0 h and T+12 h

as southerly geostrophic flow, situated between the circulation of the poleward-moving TC and a 925-hPa anticyclone to its east, impinges upon the 925-hPa baroclinic zone (Figs. 4.5d,f).

As the downstream trough moves eastward, confluent 200-hPa geostrophic flow is maintained poleward of the PRE initiation location between T−0 h and T+12 h (Figs. 4.5c,e). In conjunction with the persistent confluent flow, the equatorward entrance region of the 200-hPa jet streak and an attendant region of 200-hPa divergence remain positioned over the PRE initiation region at T+12 h(Fig. 4.5e). As the TC continues to move poleward between T−0 h and T+12 h, frontogenesis and warm-air advection at 925 hPa are maintained as the TC circulation interacts with the baroclinic zone (Fig. 4.5f). The moisture plume continues to advance northeastward from the TC along the baroclinic zone and extends toward a region of 925-hPa geostrophic confluence situated to the east of the PRE initiation location (Fig. 4.5f).

### *4.3.2 Impact of diabatic heating on the upper-tropospheric flow*

At T−12 h, the 200-hPa jet streak is situated poleward and eastward of the PRE initiation location between the region of high 250–200-hPa PV associated with the downstream trough and the region of low 250–200-hPa PV that extends to the northeast of the TC (Fig. 4.6a). As the axis of high PV associated with the downstream trough moves eastward at T−0 h and T+12 h, low-PV outflow associated with the TC and the PRE extends poleward toward the confluent jet entrance region (Figs. 4.6b,c). The poleward extension of low-PV air at T−0 h and T+12 h occurs as 200-hPa irrotational wind vectors, linked to the diabatically driven divergent outflow associated with TC and

PRE, point outward from the region of 700-hPa ascent overlying the TC and the PRE initiation location (Figs. 4.6b,c). The irrotational wind is directed from the region of low PV toward the region of high PV associated with the weak upstream short-wave trough (Figs. 4.6b,c). This configuration of the irrotational wind vectors indicates the poleward and westward advection of low-PV air, which contributes to the localized strengthening of the PV gradient within the entrance region of the jet streak between T−12 h and T+12 h (Figs. 4.6a–c). The locally strengthened PV gradient results in the slight backbuilding of the jet streak and acts to strengthen along-flow wind speed gradients within the jet entrance region (Figs. 4.6a–c). This evolution of the structure of the jet streak was concurrent with the enhancement of 200-hPa divergence (Figs. 4.5a,c,e) and 700-hPa ascent (Figs. 4.6a–c) at T−12 h and T+12 h within the equatorward entrance region of the jet streak.

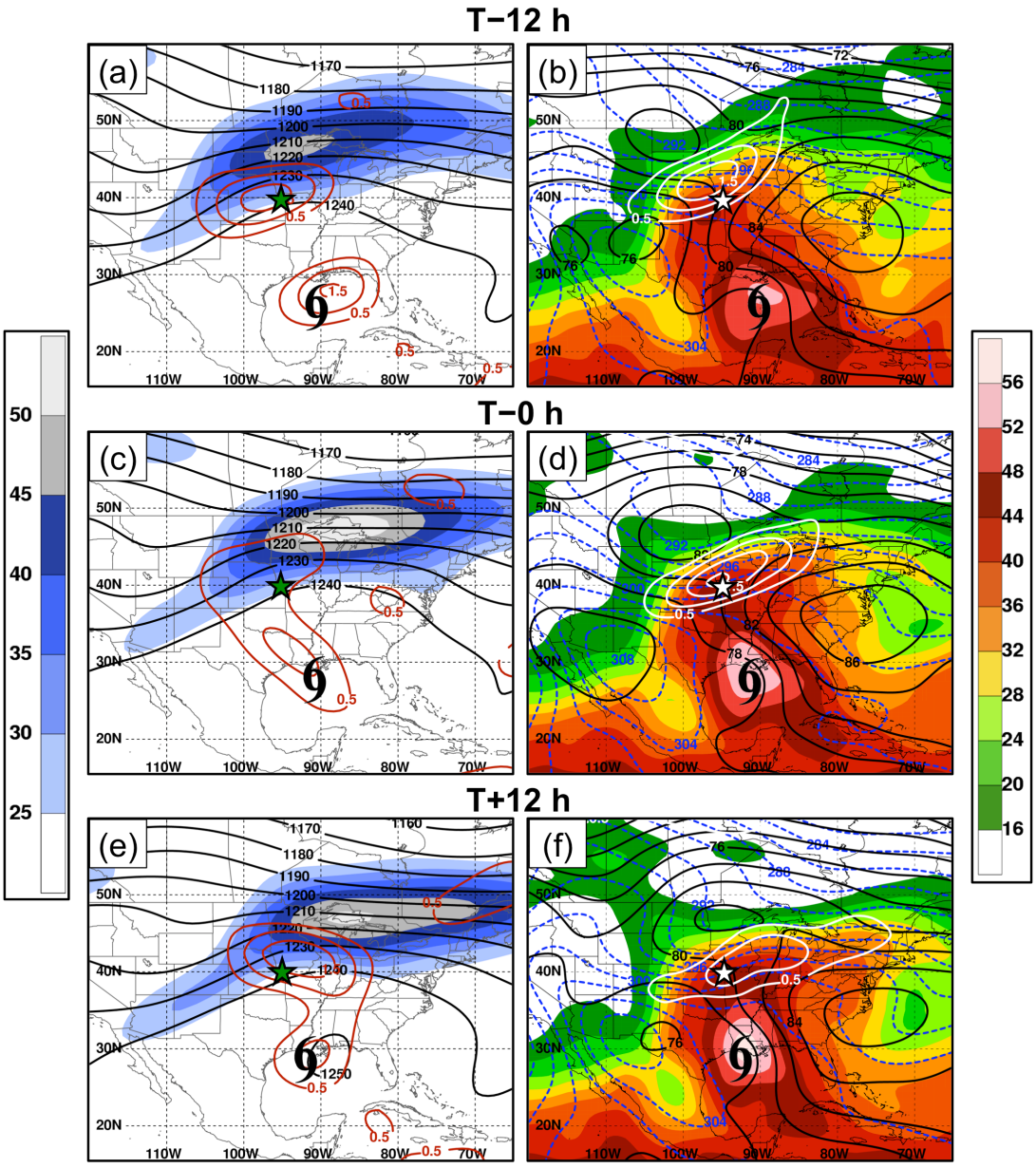


Figure 4.1: PRE-relative composites for 7 JR category PREs. The panels on the left show 200-hPa wind speed (shaded in m $s^{-1}$ according the color bar on the left), geopotential height (contoured in black every 10 dam), and positive divergence (contoured in red every 0.5 × $10^{-5}$ $s^{-1}$ starting at 0.5 × $10^{-5}$ $s^{-1}$) at (a) T−12 h, (c) T−0 h, and (e) T+12 h. The panels on the right show total PW (shaded in mm according to the colorbar on the right), as well as 925-hPa geopotential height (contoured in black every 2 dam), potential temperature (contoured in blue every 2 K), and Petterssen frontogenesis [contoured in white every 0.5 × $10^{-1}$ K (100 km)$^{-1}$ (3 h)$^{-1}$ starting at 0.5 × $10^{-1}$ K (100 km)$^{-1}$ (3 h)$^{-1}$] at (b) T−12 h, (d) T−0 h, and (f) T+12 h. The PRE initiation location is denoted by the green and white stars, and the composite TC location is marked by the tropical storm symbol.

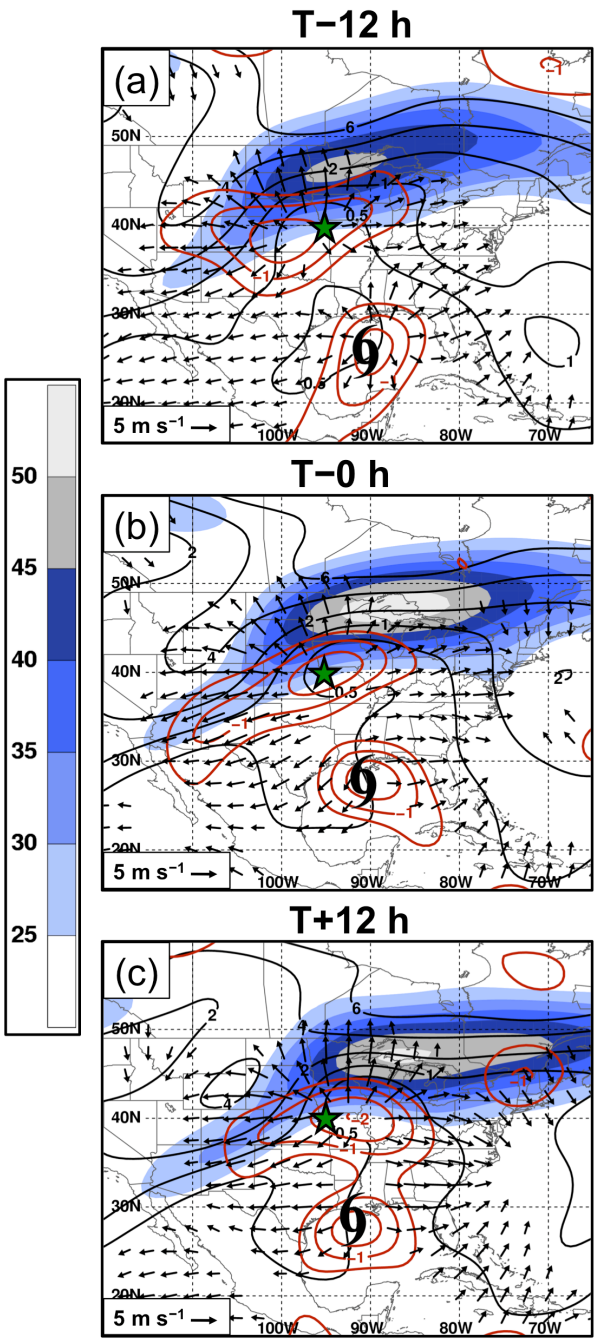


Figure 4.2: PRE-relative composites for 7 JR category PREs showing 200-hPa wind speed (shaded in m $s^{-1}$ according to the colorbar), 200-hPa irrotational wind vectors > 5 m $s^{-1}$, 700-hPa ascent (contoured in red every $0.5\times10^{-3}$ hPa $s^{-1}$ starting at $-0.5\times10^{-3}$ hPa $s^{-1}$), and 250–200-hPa PV (0.5, 1, 2, 4, and 6 PVU contours shown in black) at (a) T−12 h, (b) T−0 h, and (c) T+12 h. The PRE initiation location is denoted by the green star, and the composite TC location is marked by the tropical storm symbol.

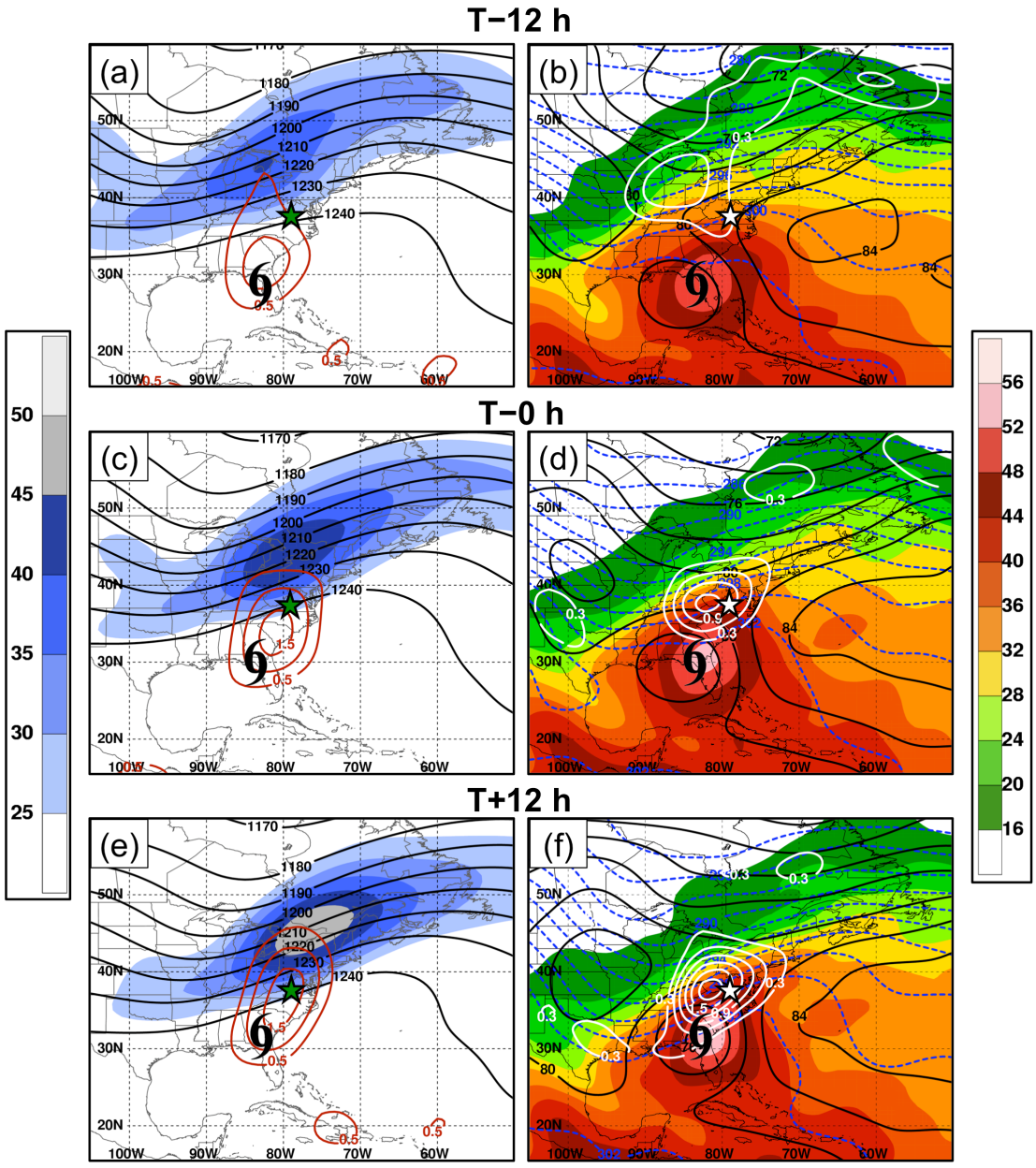


Figure 4.3: As in Fig. 4.1, except for 17 SJ category PREs, and frontogenesis in panels (b), (d), and (f) is contoured every $0.3\times10^{-1}$ K (100 km)$^{-1}$ (3 h)$^{-1}$ starting at $0.3\times10^{-1}$ K (100 km)$^{-1}$ (3 h)$^{-1}$.

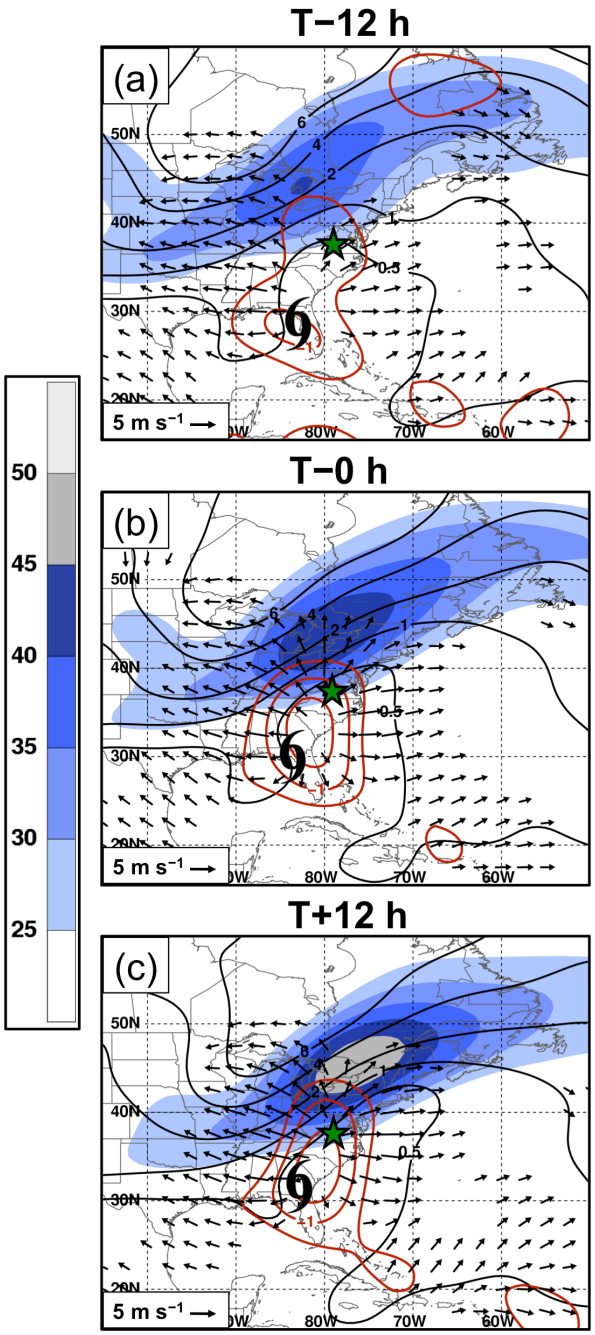


Figure 4.4: As in Fig. 4.2, except for 17 SJ category PREs.

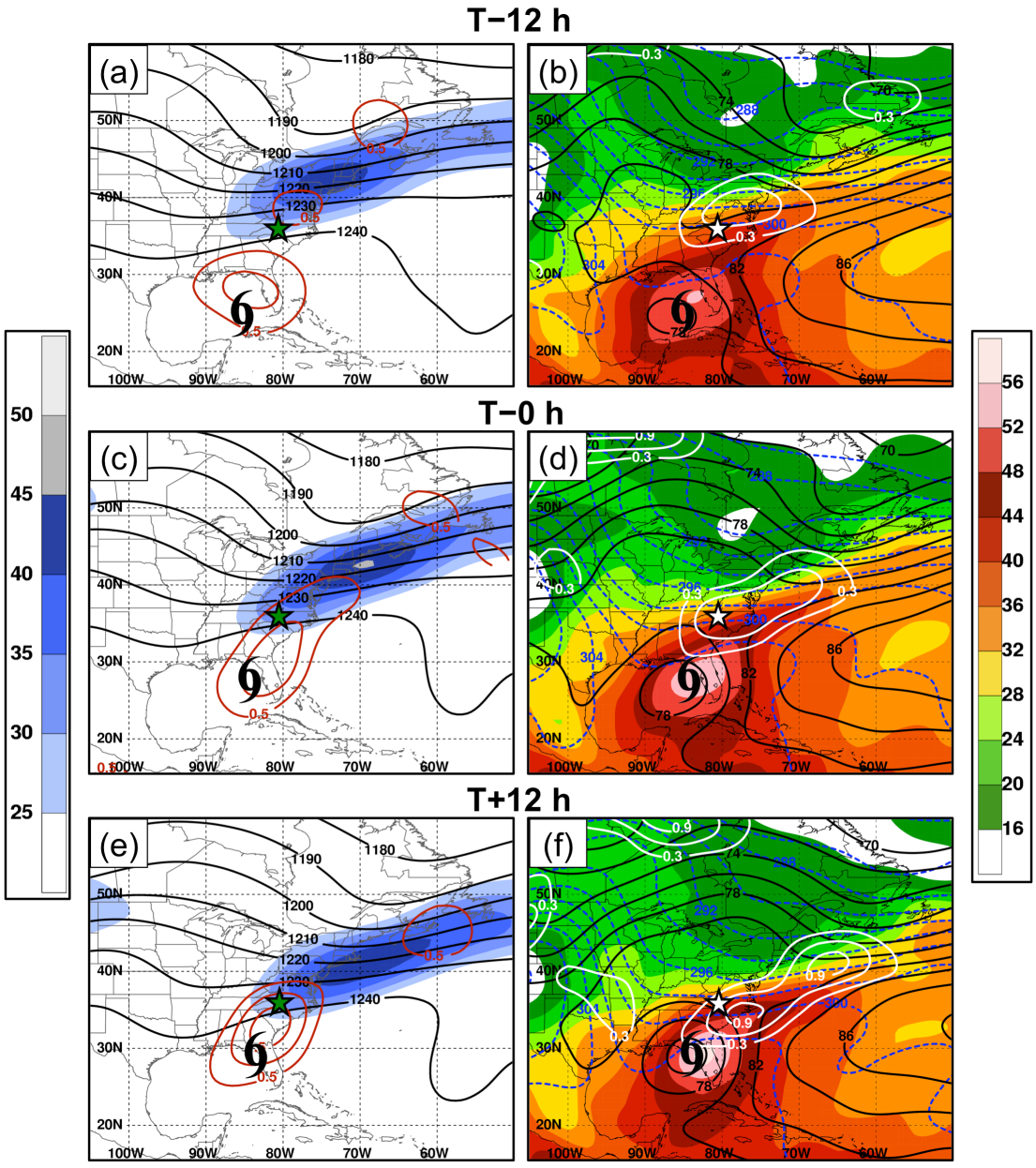


Figure 4.5: As in Fig. 4.3, except for 9 DC category PREs.

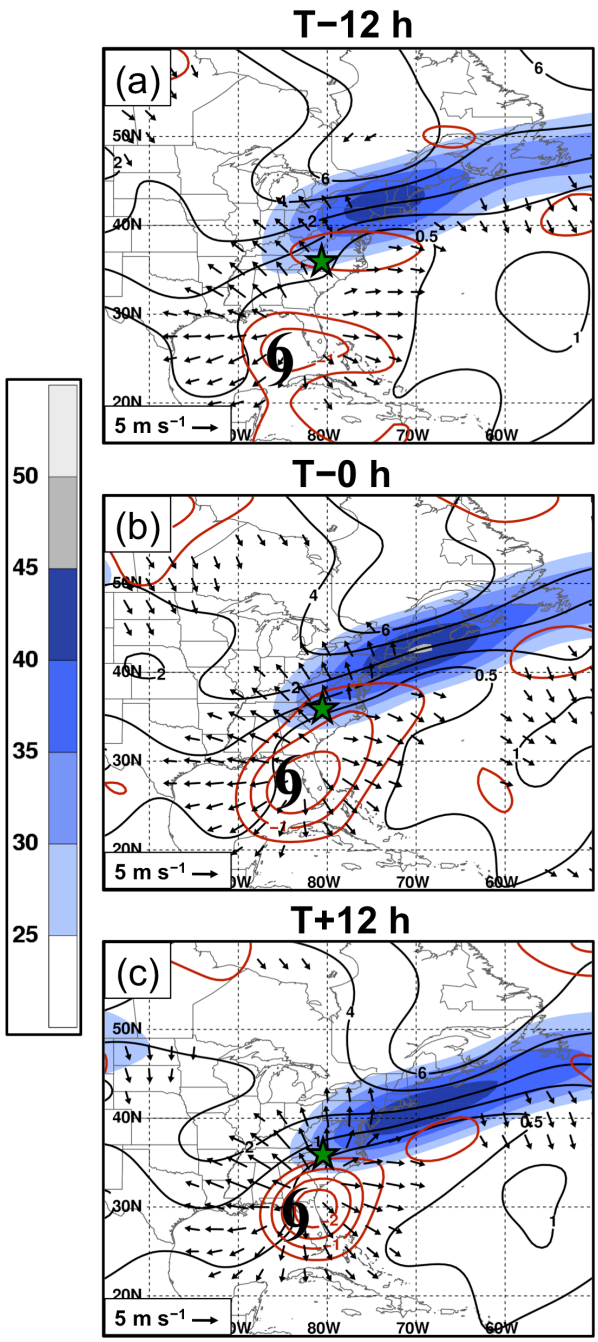


Figure 4.6: As in Fig. 4.2, except for 9 DC category PREs.

## 5. Case studies

### 5.1 PRE ahead of TC Rita (2005)

#### *5.1.1 Event overview*

A high-impact JR category PRE occurred on 25 September 2005 over southern Minnesota and northern Iowa ahead of TC Rita. The PRE developed at around 2200 UTC 24 September approximately 1100 km poleward of TC Rita, which had begun to recurve over the Texarkana region subsequent to making landfall along the Texas–Louisiana border at 0800 UTC 24 September (Fig. 5.1). The PRE was manifested as a slow-moving band of heavy, convective rainfall that stretched from northeastern Nebraska along the Minnesota–Iowa border into western Wisconsin, producing a large swath of rainfall totals in excess of 100 mm between 1200 UTC 24 and 0000 UTC 26 September (Fig. 5.1). An area of peak rainfall totals of 150–225 mm (Fig. 5.1) was centered in south-central Minnesota near the town of Wells, where 187 mm of rainfall were reported in the 24 h ending at 1200 UTC 25 September. The heavy rains resulted in flash flooding, adversely affecting various roadways, structures, and agricultural fields throughout southern Minnesota (see report online at http://climate.umn.edu/doc/journal/flash_floods/ff050924_25.htm).

#### *5.1.2 Radar observations*

At 0000 UTC 25 September, in its early stages of development, the PRE was manifested as a thin line of convection situated along the Minnesota–Iowa border and oriented parallel to westerly 20-m $s^{-1}$ 1000–500-hPa shear (Fig. 5.2a). Between 0000 UTC and 0600 UTC 25 September, the PRE grew in scale and became organized into an

MCS, manifested as a zonally oriented line of convective cells (reflectivity values > 50 dB*Z* ) over southern Minnesota with a large adjoining region of stratiform precipitation (reflectivity values 35–40 dB*Z)* (Figs. 5.2a–c). During 0000–0600 UTC 25 September, individual convective cells and adjoining stratiform precipitation within the PRE moved eastward over southern Minnesota and northern Iowa in the direction of the 1000–500-hPa shear. Concurrently, new convective cells and stratiform precipitation developed over eastern Nebraska, southeastern South Dakota, and southwestern Minnesota on the upshear flank of the PRE and subsequently moved eastward across southern Minnesota and northern Iowa (Figs. 5.2a–c). The mesoscale evolution of the PRE, resembling the "training line/adjoining stratiform" MCS archetype documented by Schumacher and Johnson (2005), afforded the continuous passage of convective cells and stratiform precipitation over southern Minnesota and northern Iowa and resulted in persistent heavy rainfall over the region.

Between 0900 UTC and 1200 UTC 25 September, the PRE began to slowly move toward the east and was manifested as a large region of heavy stratiform precipitation (reflectivity values 35–40 dB*Z*) trailing behind a leading southwest–northeast-oriented convective line (Figs. 5.2d,e). The large trailing stratiform region of precipitation allowed for heavy rainfall to persist over southern Minnesota and northern Iowa despite the eastward movement of the leading convective line. As the PRE moved toward the east after 1200 UTC 25 September, the convective and stratiform precipitation began to dissipate, losing its coherent linear organization by 1500 UTC 25 September (Fig. 5.2f).

*5.1.3 Synoptic-scale environment*

The synoptic-scale conditions at 0000 UTC 25 September, near the time of PRE initiation, are depicted in Fig. 5.3. The 200-hPa flow was characterized by a broad region of geostrophic confluence over the Upper Midwest and central Canada between an eastward-moving trough over western Manitoba and a ridge extending poleward of TC Rita across the central U.S. (Fig. 5.3a). Within the broad region of confluence, strong westerly/southwesterly flow (40–50 m $s^{-1}$) extended from the Great Plains across east-central Canada and the northeastern U.S. on the poleward flank of the broad ridge, with two diffuse jet streaks evident: one situated over eastern Ontario and western Quebec downstream of the axis of the trough over Manitoba and another stretching from the Great Lakes toward the Mid-Atlantic coast, likely related to the anticyclonic outflow associated with TC Rita (Fig. 5.3a). The PRE was positioned near the equatorward entrance region of the jet streak situated over Ontario and Quebec.

At 925 hPa, the PRE was positioned along a baroclinic zone that extended from Colorado into southern Minnesota (Fig. 5.3b). Along the baroclinic zone, a large gradient of potential temperature was present over eastern Colorado and Nebraska in association with a region of cold air damming east of the Rocky Mountains (Fig. 5.3b). Southerly 925-hPa geostrophic flow, situated between a lee trough centered in eastern Colorado and an anticyclone centered over the northeastern U.S., extended from the eastern flank of the TC Rita circulation toward the PRE region, with warm-air advection and frontogenesis established at the intersection of the southerly flow with the baroclinic zone over Nebraska, Iowa, and Minnesota (Fig. 5.3b). Coincident with this region of 925-hPa warm-air advection and 925-hPa frontogenesis, a region of 700-hPa Q-vector

convergence, indicating QG forcing for ascent, extended from eastern Wyoming into the PRE region over southern Minnesota and northern Iowa (Fig. 5.3c). The region of **Q**-vector convergence was located on the warm side of a 700-hPa baroclinic zone that stretched from Wyoming to central Minnesota, with QG frontogenesis indicated within the PRE region by **Q** vectors directed across the isentropes from cold to warm air (Fig. 5.3c).

A region of deep moisture, characterized by PW values > 50 mm, associated with TC Rita was situated over the south-central U.S., while a broad moisture plume, with PW values > 30 mm, extended poleward from TC Rita across the Midwest (Fig. 5.3b). During the previous 12 h (not shown), the moisture plume, emanating poleward from TC Rita, began to merge with an antecedent moisture strip situated along the baroclinic zone stretching across the upper Midwest, establishing deep moisture (PW values 35–45 mm) within the PRE region by 0000 UTC 25 September (Fig. 5.3b). An atmospheric sounding from Omaha, Nebraska (OAX), at 0000 UTC 25 September (Fig. 5.4a) reflects these moist conditions, with a PW value of 36 mm, and reveals the presence of moderate instability just south of the PRE region, with 1103 J $kg^{-1}$ of convective available potential energy (CAPE). Additionally, veering winds from the surface up to 500 hPa at OAX indicate the presence of warm-air advection in the vicinity of the PRE (Fig. 5.4a). A sounding from Chanhassen, Minnesota (MPX), at 0000 UTC 25 September (Fig. 5.4b) indicates that, to the north of the PRE region, the environment was characterized by deep moisture, with a PW value of 37 mm, as well as a nearly moist neutral temperature profile between 800 hPa and 250 hPa.

*5.1.4 Processes leading to heavy rainfall*

5.1.4.1 Lifting mechanisms

A time–height section of NOAA profiler winds at Slater, Iowa (SLA) (Fig. 5.5), located just to the south of the PRE region, indicates that between 0000 UTC 25September and 0600 UTC 25 September, coincident with the nocturnal development and organization of the PRE (Figs. 5.2a–c), the winds between 925 hPa and 850 hPa veered from southeasterly to southerly and strengthened from 10 m $s^{-1}$ to approximately 15 m $s^{-1}$. The veering and strengthening of the low-level winds at SLA during 0000–0600 UTC 25 September coincided with the development of strong southerly 925-hPa flow (wind speeds 15–20 m $s^{-1}$) extending from the circulation of TC Rita across the Central Plains toward the 925-hPa baroclinic zone situated along the Minnesota–Iowa border (Figs. 5.6a–c). As the southerly 925-hPa flow strengthened and became oriented perpendicular to the baroclinic zone during 0000–0600 UTC 25 September, frontogenesis and warm-air advection strengthened along the Minnesota–Iowa border, coinciding with the rapid growth and organization of the PRE on the cool side of the baroclinic zone (Figs. 5.6a–c). Between 0600 UTC and 1200 UTC 25 September, the PRE moved southeastward toward the warm side of the baroclinic zone as the southerly 925-hPa winds continued to veer and became aligned parallel to the baroclinic zone (Figs. 5.6c,d). The veering of the 925-hPa flow resulted in the weakening of frontogenesis and warm-air advection along the baroclinic zone (Fig. 5.6d), likely contributing to the observed dissipation of the PRE over the subsequent 3 h (Fig. 5.2f).

Vertical cross sections taken from north to south through the centroid of the PRE indicate that the development of the PRE between 0000 UTC and 0600 UTC 25

September occurred as southerly flow ascended over the low-level baroclinic zone in the presence of a poleward stream of deep moisture emanating from TC Rita (Figs. 5.7a,b). By 0600 UTC 25 September, frontogenesis had strengthened markedly at low levels within the baroclinic zone, while deep, vigorous ascent had developed over the PRE region (Fig. 5.7b). A vertical cross section taken through the PRE at 1200 UTC 25 September indicates a continued poleward stream of deep moisture from TC Rita and the reduction in low-level frontogenesis indicated in Fig. 5.6d. Deep, vigorous ascent over the PRE region extended along a poleward-sloping region of frontogenesis between 850 hPa and 250 hPa (Fig. 5.7c).

5.1.4.2 Moisture contributions from TC Rita

Concurrent with the veering and strengthening of the southerly low-level flow at SLA during 0000–0600 UTC 25 September (Fig. 5.5), a corridor of strong southerly 1000–700-hPa vertically integrated moisture flux (VIMF) developed across the Central Plains, extending from the TC Rita circulation toward the PRE region (Figs. 5.8a–c). During 0000–0600 UTC 25 September, the strong VIMF resulted in the poleward progression of a plume of moisture, with 1000–700-hPa PW values > 28 mm, from TC Rita into the PRE region (Figs. 5.8a–c). As the moisture plume progressed into the PRE region, it merged with an antecedent strip of moisture, with 1000–700-hPa PW values 32–40 mm, along the baroclinic zone (Figs. 5.8a–c). During 0300–0600 UTC 25 September, VIMF convergence was maximized over Nebraska, northwestern Iowa, and southwestern Minnesota at the terminus of the corridor of southerly VIMF (Figs. 5.8b,c) and persisted on the upshear flank of the PRE (cf. Figs. 5.2b,c). The maximized VIMF

convergence, located within a convectively unstable environment (not shown) and in the presence of forcing for ascent (Figs. 5.6b,c), favored the continuous development of convective and stratiform precipitation on the upshear flank of the PRE (Fig. 5.2b,c), thereby helping to preclude the eastward movement of the PRE.

By 1200 UTC 25 September, 1000–700-hPa PW values 28–40 mm were in place through a large region extending from the TC Rita circulation into the PRE region (Fig. 5.8d). Consistent with the veering of the low-level flow at SLA between 0600 UTC and 1200 UTC 25 September (Fig. 5.5), the VIMF vectors within the PRE region veered from southerly to southwesterly, while the locus of maximized VIMF convergence shifted to the east of the PRE (Fig. 5.8d). The eastward shift of VIMF convergence likely contributed to the observed eastward movement of the PRE during 0600–1200 UTC 25 September (Figs. 5.2c–e)

Two sets of five 36-h backward kinematic air parcel trajectories ending at 0600 UTC 25 September were computed in order to establish the source regions for air parcels entering the PRE region (Fig. 5.9). The first set of trajectories was computed from 850 hPa on the warm side of the 925-hPa baroclinic zone (dashed blue line in Fig. 5.9) along which the PRE developed, and the second set was computed from 700 hPa on the cool side of the baroclinic zone. The trajectories indicate that parcels entering the PRE region originated within two distinct regions of moisture at 1800 UTC 23 September: 1) the poleward flank of the TC Rita moisture plume over Arkansas, Mississippi, and Alabama and 2) an antecedent strip of moisture stretching across the central U.S from Oklahoma to Illinois (Fig. 5.9). Figure 5.9 also indicates that the parcels ending at 700 hPa on the cool side of the baroclinic zone ascended (indicated by decreasing air parcel pressure) as they

entered the PRE region, consistent with the ascent over the baroclinic zone indicated in Fig. 5.7b.

5.1.4.3 Impact of diabatic heating on the upper-tropospheric flow

The development and organization of the PRE during 0000–0600 UTC 25 September in the presence of warm-air advection, frontogenesis, and low-level moisture flux from TC Rita coincided with the rapid development of a strong anticyclonically curved 200-hPa jet streak poleward of the PRE region (Figs. 5.10a,b). The development of the jet streak occurred in conjunction with a substantial reduction of 250–200-hPa PV over and directly poleward of the PRE, with PV values decreasing from 1–2 PVU at 0000 UTC 25 September to < 0.5 PVU at 0600 UTC 25 September (Figs. 5.10a,b). This reduction in PV, likely the result of the vertical redistribution of PV through diabatic heating associated with latent heat release within the PRE, occurred as strong 200-hPa irrotational flow emanated outward from a region of maximized 700-hPa ascent over the PRE region (Fig. 5.10b). The irrotational wind vectors, linked to diabatically generated divergent outflow associated with the PRE, were directed from the region of low PV overlying the PRE region toward an axis of high PV associated with an eastward-moving trough over Manitoba and Ontario (Fig. 5.10b). This configuration of the irrotational wind resulted in the advection of low-PV air poleward and westward of the PRE region, leading to the development of a strong PV gradient poleward and westward of the PRE region (Fig. 5.10b). A strong, concentrated jet streak, characterized by strong along-flow wind speed gradients, developed over northern Minnesota and southern Ontario along this strong PV gradient. The PRE was positioned directly beneath the equatorward

entrance region of this jet streak, a configuration suggesting enhanced forcing for ascent over the PRE (Fig. 5.10b). During 0600–1200 UTC 25 September (Figs. 5.10b,c), the jet streak continued to strengthen, with maximium wind speeds increasing from 60–65 m $s^{-1}$ at 0600 UTC 25 September to 75–80 m $s^{-1}$ at 1200 UTC 25 September, while the PRE remained situated within the equatorward entrance region.

The likely impact of diabatic heating on the vertical redistribution of PV is illustrated by vertical cross sections taken from north to south through the jet streak, PRE, and TC, which show a substantial reduction of PV above a region of deep ascent that developed between 0000 UTC and 1200 UTC 25 September (Figs. 5.11a,b). The reduction of PV aloft resulted in the lifting of the tropopause, leading to the development of strong horizontal PV gradients and to an increase in wind speeds in the upper troposphere directly poleward of the PRE (Fig. 5.11b). Additionally, the potential temperature gradient increased between 500 hPa and 250 hPa poleward of the region of deep ascent from 0000 UTC to 1200 UTC 25 September (Figs. 5.11a,b). The enhanced upper-tropospheric potential gradient was coincident with the region of strong frontogenesis between 700 hPa and 250 hPa that had developed by 1200 UTC 25 September (Fig. 5.7d) and was consistent with increased wind speeds within the jet streak (Figs. 5.10c, 5.11b).

## 5.2 PRE ahead of TC Ernesto (2006)

### *5.2.1 Event overview*

A particularly high-impact DC category PRE occurred over North Carolina and Virginia during 30–31 August 2006 ahead of TC Ernesto. The high-impact nature of this

event resulted not only from the heavy, convective rainfall associated with the PRE, but also from the subsequent passage of TC Ernesto rain shield over the PRE region during the 24 h following the dissipation of the PRE. The passage of the TC produced heavy rainfall throughout central and eastern North Carolina and Virginia over soils previously saturated by the PRE rainfall. The cumulative impact of the two heavy rainfall events associated with the PRE and TC Ernesto, respectively, resulted in widespread flash flooding throughout North Carolina and Virginia during 30 August–2 September 2006 (NCDC 2006).

During 1200 UTC 30 August–1200 UTC 31 August, the TC Ernesto PRE produced multiple local rainfall maxima of 50–100 mm throughout central and eastern North Carolina and Virginia within a broad region of rainfall totals > 20 mm (inset in Fig. 5.12). As TC Ernesto tracked poleward along the southeastern U.S. coast on 1 September, it produced widespread heavy rainfall throughout North Carolinia and Virginia, with the highest rainfall totals (100–250 mm) observed during 1200 UTC 30 August–1200 UTC 1 September along the coasts of these two states (Fig. 5.12). Particularly hard hit were towns near the Albemarle Sound in northeastern North Carolina, where approximately 100 mm of rain fell in association with the PRE and another 150 mm of rain subsequently fell with the passage of TC Ernesto. Concurrent with the passage of TC Ernesto over eastern North Carolina and Virginia on 1 September, a second PRE developed directly to the northwest of the TC over West Virginia, eastern Kentucky, eastern Tennessee, and western North Carolina, accounting rainfall totals of 70–90 mm over these regions (Fig. 5.12).

*5.2.2 Synoptic-scale environment*

The synoptic-scale conditions at 1800 UTC 30 August 2006, approximately the time of PRE initiation, are shown in Fig. 5.13. Bearing a substantial resemblance to the pattern depicted in the PRE-relative 200-hPa composites for the DC category (Figs. 4.5a,c,e), the 200-hPa flow was dominated by a region of geostrophic confluence associated with a trough-over-ridge pattern situated downstream and poleward of TC Ernesto over the northeastern U.S. (Fig. 5.13a). A 200-hPa jet streak with slight anticyclonic curvature was situated within this region of confluence, with maximum wind speeds of 60–70 m $s^{-1}$ located over Maine at the base of the downstream trough (Fig. 5.13a). The PRE developed within the equatorward entrance region of this jet streak and downstream of the axis of a weak short-wave trough situated over the east-central U.S. (Fig. 5.13a).

In association with the 200-hPa trough situated over the northeastern U.S., a 925-hPa cyclone was located off the coast of Newfoundland, with a trailing 925-hPa baroclinic zone stretching southwestward from the cyclone center toward the eastern U.S. coast (Fig. 5.13b). Deep moisture, characterized by PW values > 50 mm, extended poleward from the vicinity of TC Ernesto along the southeastern U.S. coast and stretched eastward along the trailing baroclinic zone (Fig. 5.13b). Weak cold-air advection driven by northerly geostrophic flow along the baroclinic zone over North Carolina and Virginia established a weakly defined region of cold-air damming on the east side of the Appalachian Mountains over North Carolina and Virginia (Fig. 5.13b). The PRE developed in the presence of PW values of 55–60 mm within a region of weak 925-hPa frontogenesis that stretched across North Carolina and Virginia along the baroclinic zone

(Fig. 5.13b). Weak frontogenesis within the PRE region is also manifested at 700 hPa by **Q** vectors over North Carolina and Virginia pointing across isentropes from cold to warm air (Fig. 5.13c). While frontogenesis was present within the PRE region, QG forcing for ascent, diagnosed by **Q**-vector convergence at 700 hPa, was quite weak at the time of PRE initiation (Fig. 5.13c).

*5.2.3 Processes leading to heavy rainfall*

5.2.3.1 Lifting mechanisms

In a moist environment characterized by weak forcing for ascent at low and midlevels (Fig. 5.13b,c), precipitation associated with the PRE developed over central North Carolina and rapidly became organized during 1800 UTC 30 August–0000 UTC 31 August. The PRE was organized as a large region of heavy stratiform rainfall (reflectivity values > 35 dB*Z*) with embedded convective cells (reflectivity values > 50 dB*Z*) that extended over a large portion of North Carolina and Virginia during this 6-h period (Fig. 5.14a–c). The initial development of convection associated with the PRE occurred at approximately 1800 UTC 30 August in the presence of 10-m wind speed convergence on the warm side a 2-m (hereafter surface) thermal boundary to the east of a region of the cold-air damming along the Appalachian Mountains over western North Carolina and Virginia (Figs. 5.14a,b). Atmospheric soundings at 1800 UTC 30 Augut from Greensboro, North Carolina (GSO, Fig. 5.15a), and Newport, North Carolina (MHX, Fig. 5.15b), indicate that the environment in which the PRE developed was characterized by moderate to strong conditional instability, with respective CAPE values

of 1753 J $kg^{-1}$ and 3462 J $kg^{-1}$, and by deep moisture, with respective PW values of 54 mm and 53 mm.

The growth and organization of the PRE into a large region of convective and stratiform precipitation during 1800 UTC 30 August–0000 UTC 31 August was coincident with the formation of a pronounced surface cold pool extending over South Carolina, North Carolina, and Virginia to the east of the Appalachian Mountains (Figs. 5.14b,c). The colocation of the cold pool with the region of convective and stratiform precipitation associated with the PRE indicates the likely role of evaporative cooling associated with falling precipitation for the formation of cold pool. The presence a layer of relatively dry air between 900 hPa and 700 hPa in a sounding from GSO at 0000 UTC 31 August (Fig. 5.15c) suggests that favorable conditions for the evaporation of falling precipitation were present within the PRE region.

The cold pool formation associated with the PRE reinforced a weak antecedent cold pool over North Carolina and Virginia associated with the aforementioned region of cold-air damming east of the Appalachian Mountains, establishing a surface thermal boundary over central South Carolina and eastern North Carolina (Figs. 5.14b,c). During 2100 UTC 30 August–0000 UTC 31 August, southerly 10-m flow extending poleward of TC Ernesto impinged upon the surface thermal boundary (Figs. 5.14b,c). Vertical cross sections through the PRE and the cold pool at 2100 UTC 30 August (Fig. 5.16a) and 0000 UTC 31 August (Fig. 5.16b) indicate that southerly low-level flow ascended over a region of baroclinicity on the equatorward edge of the cold pool in the presence of low-level frontogenesis and within a poleward stream of deep moisture, initiating deep ascent beneath the equatorward entrance region of an upper-tropospheric jet streak. The

configuration depicted in the cross sections (Figs. 5.16a,b) illustrates the importance of lift over a region of baroclinicity at the edge of the cold pool, induced by evaporational cooling, as a focus for the development and maintenance of heavy precipitation over North Carolina and Virginia.

By 0600 UTC 31 August, 10-m winds had weakened from 5–10 m $s^{-1}$ at 0000 UTC 31 August to < 2.5 m $s^{-1}$ along the North Carolina coast and had became oriented nearly parallel to the surface thermal boundary as TC Ernesto advanced poleward (Fig. 5.14d). These changes in the 10-m wind were likely associated with both reduced ascent over the cold pool and decreased low-level frontogenesis along the surface thermal boundary (not shown), likely contributing to the observed weakening and dissipation of the convective and stratiform precipitation associated with the PRE during 0000–0600 UTC 31 August (Figs. 5.14d).

5.2.3.2 Moisture contributions from TC Ernesto

The development and organization of the PRE during 1800 UTC 30 August–0000 UTC 31 August occurred within an expansive plume of deep moisture, with PW values > 45 mm, extending poleward and eastward from TC Ernesto (Figs. 5.17a–c). The transport of deep moisture into the PRE region occurred in the form of a corridor of strong poleward 1000–100-hPa VIMF extending from the eastern flank of the TC Ernesto circulation toward the PRE region (Figs. 5.17a–c). The heaviest precipitation during 2100 UTC 30 August–0000 UTC 31 August (cf. Fig. 5.14) was focused within a region of maximized VIMF convergence and coincided with a strip of PW values of 50–65 mm over North Carolina and Virginia (Figs. 5.17b,c). During 0000–0600 UTC 31 August,

the VIMF vectors veered from southwesterly to westerly-southwesterly within the PRE region, coinciding with a reduction of VIMF convergence (Figs. 5.17c,d) and coinciding with the observed weakening of the PRE (Figs. 5.14c,d).

In order to establish source regions for air parcels entering the PRE region at low and upper levels, 36-h backward kinematic air parcel trajectories ending in the PRE region at 925 hPa (Fig. 5.18a) and 400 hPa (Fig. 5.18b) at 0000 UTC 31 August were computed. Air parcels ending at 925 hPa originated on the poleward flank of the TC Ernesto moisture plume and within a region of deep moisture over Georgia and the Florida panhandle (Fig. 5.18a). Air parcels ending at 400 hPa originated within the TC Ernesto moisture plume as well as along the coast of the Gulf of Mexico within a region of deep moisture (Fig. 5.18b). The trajectory analysis indicates two distinct source regions of deep moisture for the PRE: 1) within and on the poleward flank of the TC Ernesto moisture plume, 2) over the southeastern U.S. along the Gulf of Mexico coast. Air parcel trajectories originating within the TC Ernesto moisture plume and ending at both 925 hPa (Fig. 5.18a) and 400 hPa (Fig. 5.18b) exhibit anticyclonic curvature, consistent with motion on the western flank of a ridge downstream of the TC. The backward trajectories ending at 400 hPa (Fig. 5.18b) are also confluent over the PRE region, reflecting the confluent upper-level jet entrance region directly poleward of the PRE (Fig. 5.13a).

5.2.3.3 Impact of diabatic heating on the upper-tropospheric flow

As the PRE became organized as a large region of convective and stratiform precipitation during 1800 UTC 30 August–0000 UTC 31 August, the 200-hPa jet streak

poleward of the PRE developed strong along-flow wind speed gradients within its confluent entrance region while concurrently developing pronounced anticyclonic curvature directly poleward of the PRE (Figs. 5.19a,b). These flow changes within the jet streak occurred as a plume of low 250–200-hPa PV air extended poleward and westward of the PRE region in conjunction with the development of considerable divergent outflow associated with the PRE (Fig. 5.19a,b), as manifested at 0000 UTC 31 August by 200-hPa irrotational winds emanating radially outward from a maximum of 700-hPa ascent over the PRE region (Fig. 5.19b). By 0000 UTC 31 August, the advection of low-PV air by the divergent PRE outflow towards the axis of high PV associated with a weak upstream short-wave trough resulted in locally strengthened PV gradient directly poleward and westward of the PRE, acting to backbuild the jet streak and contributing to increased along-flow wind speed gradients within the entrance region of the jet streak (Fig. 5.19b).

*5.2.4 Processes contributing to an along-track PRE*

As discussed in section 5.2.1, a factor that made this PRE a particularly high-impact event is that it was followed by a second episode of heavy precipitation directly associated with TC Ernesto. In order to understand the processes leading to this second episode of heavy rainfall directly associated with the TC, it is necessary to address the following two questions: 1) what caused the TC to track along the eastern U.S. coast and to eventually move inland over North Carolina and Virginia, and 2) what were the mechanisms that led to heavy precipitation as the TC passed over North Carolina and Virginia. The following two sections will suggest possible answers to these questions.

5.2.4.1 Synoptic-scale influences on the track of TC Ernesto

During 1200 UTC 31 August–0000 UTC 1 September, TC Ernesto moved along the eastern U.S. coast in the direction of the 200-hPa nondivergent flow downstream of a weak short-wave trough and on the western flank of a downstream ridge (Figs. 5.20a–d). During 1200 UTC 31 August–0000 UTC 1 September, TC Ernesto reached the equatorward entrance region of the 200-hPa jet streak, and substantial divergent outflow developed, as manifested by 200-hPa irrotational wind vectors emanating outward from the maximum of 700-hPa ascent associated with the TC (Fig. 5.20b,d). Between 1200 UTC 31 August and 1200 UTC 1 September, the divergent outflow pattern associated with TC Ernesto contributed to the advection of low 250–200-hPa PV outward from the poleward-moving TC (Figs. 5.20d,f). This outflow of low-PV air occurred in conjunction with ridge amplification, evident in the 200-hPa streamfunction field, and a concurrent enhancement of anticyclonic flow poleward and westward of TC Ernesto (Figs. 5.20c,e). During 0000–1200 UTC 1 September, the ridge amplification appears to have precluded the eastward progression of the weak upstream short-wave trough and aided in maintaining southerly nondivergent 200-hPa flow along the east coast of the U.S. in the vicinity of TC Ernesto (Figs. 5.20c–f). This southerly nondivergent 200-hPa flow, in turn, likely contributed to persistent southerly steering flow over TC Ernesto, causing the TC to move poleward along the coast and to eventually track over North Carolina and Virginia.

Also, it is important to note that as TC Ernesto moved poleward during 0000–1200 UTC 1 September, the persistent low-PV outflow contributed to the maintenance of

a strong PV gradient poleward of the TC along the axis of the jet streak (Figs. 5.20d,f). During the 12-h period, the PV gradient along the axis of the jet streak was maximized off the coast of New England and decreased westward toward the eastern Great Lakes wind speed, thereby maintaining strong along-flow wind speed gradients within the jet entrance region directly poleward of TC Ernesto (Figs. 5.20d,f). The position of the TC beneath the equatorward entrance region of the jet streak favored persistent strong ascent over the TC (Figs. 5.20d,f) and is consistent with the heavy precipitation observed as TC Ernesto moved over eastern North Carolina and Virginia during 0000–1200 UTC 1 September (Fig. 5.12). Klein (2007, 61–66) documented the importance of lift within the equatorward entrance region of the jet streak for the production of heavy precipitation as TC Ernesto tracked across the mid-Atlantic region of the U.S.

5.2.4.2 Mesoscale distribution of the TC Ernesto rainfall

While the upper-tropospheric flow allowed TC Ernesto to track along the eastern coast of the U.S. and to make landfall in North Carolina, mesoscale processes were important for focusing heavy rainfall during 1200 UTC 31 August–1200 UTC 1 September over central and eastern North Carolina and Virginia. As TC Ernesto moved poleward along the coast of South Carolina between 1200 UTC 31 August and 0000 UTC 1 September, stratiform precipitation extended poleward of the storm center (Fig. 5.21a–c). This stratiform precipitation was focused over central and eastern South and North Carolina on the cool side of a surface thermal boundary associated with both the remnant PRE cold pool and continued cold-air damming on the east side of the Appalachians Mountains (Figs. 5.21a–c). This precipitation was associated with low-level warm-air

advection as southeasterly 10-m flow on the northeastern flank of the TC circulation impinged upon the surface thermal boundary (Figs. 5.21a–c). Also of note during this 12-h period, a distinct region of heavy precipitation developed over eastern Kentucky, West Virginia, and western North Carolina along the spine of the Appalachian Mountains (Figs. 5.21a–c). This region of precipitation constituted the development of the second PRE in response to moist easterly flow associated with the TC Ernesto circulation ascending over elevated terrain.

As TC Ernesto moved poleward during 0000–0600 UTC 1 September, making landfall in southeastern North Carolina, the strong cyclonic circulation of the TC began to distort the surface isentropes (Figs. 5.21c,d). Strong (10–20 m $s^{-1}$) southeasterly and easterly 10-m flow on the eastern side of the TC Ernesto circulation resulted in strong warm-air advection over coastal North Carolina and Virginia (Figs. 5.21c,d). Inland over central North Carolina and Virginia, strong cold-air advection was driven by northeasterly flow parallel to the spine of the Appalachian Mountains on the on the western side of the TC circulation (Figs. 5.21c,d). By 0600 UTC 1 September, this thermal advection pattern associated with the TC circulation had established a strong surface potential temperature gradient over eastern North Carolina and Virginia (Fig. 5.21d). Klein (2007, 66–68) showed that heavy precipitation associated with TC Ernesto was focused within a region of forcing for ascent associated with strong low-level frontogenesis and **Q**-vector convergence along this surface thermal boundary. By 0600 UTC 1 September, a broad region of heavy stratiform and convective precipitation extended poleward from the center of TC Ernesto over central and eastern North Carolina

and Virginia along and on the cool side of the surface thermal boundary, with the heaviest precipitation concentrated over coastal North Carolina (Fig. 5.21d).

## 5.3 PRE ahead of TC Wilma (2005)

### *5.3.1 Event overview*

TC Wilma (2005) is the most intense hurricane ever recorded in the Atlantic basin, reaching a minimum central pressure of 882 hPa on 19 October 2005 (Beven and Coauthors 2008). During 21–24 October 2005, TC Wilma produced widespread flooding and wind damage over the Yucatan Peninsula, Cuba, and southern Florida (Beven and Coauthors 2008). During 23–24 October as TC Wilma translated northeastward across southeastern Gulf of Mexico (Fig. 5.22), its outer circulation began interacting with a midlatitude baroclinic zone situated along the southeastern U.S. coast. This interaction resulted in the development of a SJ category PRE, manifested as a band of convective and stratiform rainfall situated along the coast of Georgia and South Carolina. During 24–25 October, TC Wilma accelerated poleward along the eastern U.S. coast and weakened (Fig. 5.22) while continuing to interact with the baroclinic zone. TC Wilma became extratropical at 0000 UTC 26 October, subsequently merging with a midlatitude disturbance south of Nova Scotia and developing into a deep (~988 hPa central pressure) extratropical cyclone during 26–27 October (Beven and Coauthors 2008).

The largest rainfall totals (radar estimates of 50–100 mm; not shown) associated with the PRE were largely focused over the coastal waters adjacent to Georgia, South Carolina, and North Carolina, with only 10–50 mm of rainfall occurring onshore (Fig. 5.22). Because the heaviest precipitation was mainly focused over coastal waters, this

PRE was not a particularly high-impact event relative to the PREs associated with TC Rita (2005) and the TC Ernesto (2006). Despite its low-impact nature, the TC Wilma PRE case is of considerable scientific interest because it involved the development of a PRE in response to the direct interaction of the TC Wilma circulation with a midlatitude baroclinic zone preceding the ET of the TC. This case therefore demonstrates the linkage that can exist between PREs and the ET process (e.g., Klein et al. 2000; Atallah and Bosart 2003).

### *5.3.2 Satellite and radar observations*

#### 5.3.2.1 Satellite observations

Infrared (IR) satellite observations at 1800 UTC 23 October indicate an expansive cloud shield extending poleward from TC Wilma along the eastern U.S. coast toward a midlatitude cyclonic system situated south of Nova Scotia (Fig. 5.23a). As a secondary feature, a cluster of clouds and deep convection associated with Tropical Storm (TS) Alpha was situated between Cuba and Haiti (Fig. 5.23a). During the subsequent 18 h, convection associated with TC Wilma intensified, and a well-defined eye developed as the TC moved northeastward across southern Florida (Figs. 5.23b–d). Concurrently, the large poleward-extending cloud shield adjoined to TC Wilma expanded while beginning to envelop the TS Alpha cloud cluster (Figs. 5.23b–d). The cloud structure depicted in the IR imagery during 1800 UTC 23 October–1200 UTC 24 October (Figs. 5.23a–d) closely resembled "step 1" of the transformation stage of ET documented by Klein et al. (2000; their Fig. 5), wherein the circulation of a poleward-moving TC first begins to

interact with a preexisting midlatitude baroclinic zone and develops large asymmetries in its cloud structure.

5.3.2.2 Radar observations

At 1800 UTC 23 October, the developing PRE, situated within the expansive cloud shield that extended poleward from TC Wilma (Fig. 5.23a), was linearly organized and oriented parallel to the Georgia and South Carolina coastlines (Fig. 5.24a). During 1800 UTC 23 October–0600 UTC 24 October, the PRE expanded in size and intensified, developing an elongated band of radar reflectivity values of 35–45 dB*Z* (Figs. 5.24a–d). As this expansion and intensification occurred, the PRE shifted toward the coast, with incursions of heavy rainfall occurring into eastern Georgia and eastern South Carolina (Figs. 5.24c,d). Between 0600 UTC and 1200 UTC 24 October, the PRE expanded poleward toward the North Carolina coast as TC Wilma crossed southern Florida (Figs. 5.24d,e).

During 1200–1800 UTC 24 October, the PRE appeared to merge with the TC Wilma rain shield, no longer constituting a separate region of rainfall and therefore, according to the methodology used in this study, no longer technically qualifying as a PRE (Figs. 5.24e,f). It is important to appreciate, however, that it is impossible to fully assess the structural evolution of the PRE due to the limitations of U.S. coastal radar coverage. Having merged with the TC rain shield by 1800 UTC 24 October, the ex-PRE was still manifested as a coherent region of stratiform and convective precipitation stretching along the southeastern and mid-Atlantic coastlines of the U.S. (Fig. 5.24f).

*5.3.3 Synoptic-scale environment*

The synoptic-scale conditions at 1800 UTC 23 October, the time of PRE initiation, are shown in Fig. 5.25. The conditions present at 200 hPa (Fig. 5.25a) and 925 hPa (Fig. 5.25b) are quite similar to those exhibited by the SJ composites (Fig. 4.3). The 200-hPa flow was dominated by a high-amplitude positively tilted trough over the central U.S. situated upstream of northeastward-moving TC Wilma (Fig. 5.25a). Downstream of the trough axis, a straight southwesterly jet streak, with maximum wind speeds of 75–80 m $s^{-1}$, was situated along the eastern U.S. coast poleward of TC Wilma (Fig. 5.25a). The PRE developed within the equatorward entrance region of this jet streak poleward and eastward of TC Wilma (Fig. 5.25a).

The focus for PRE development at 925 hPa was a baroclinic zone associated with a slow-moving cold front that trailed behind a strong 925-hPa midlatitude cyclone located off the coast of New England (Fig. 5.25b) beneath the poleward exit region of the 200-hPa jet streak (Fig. 5.25a). Warm-air advection and frontogenesis were established within the PRE region as southerly geostrophic flow on the eastern flank of the TC Wilma circulation impinged upon the baroclinic zone situated along the coast of Florida, Georgia, and South Carolina (Fig. 5.25b). At 700 hPa, QG forcing for ascent, indicated by a region of **Q**-vector convergence, was maximized on the northeastern side of TC Wilma just to the west of the PRE region (Fig. 5.25c). Additionally, 700-hPa **Q** vectors within the PRE region pointing across the isentropes from cold to warm air indicate the presence of QG frontogenesis (Fig. 5.25c), coinciding with the frontogenesis present at 925 hPa (Fig. 5.25b).

A plume of deep moisture, characterized by PW values > 50 mm, extended poleward and eastward from the TC Wilma circulation along the southeastern U.S. coast and through a broad region over the western North Atlantic Ocean on the warm side of the 925-hPa baroclinic zone (Fig. 5.25b). Embedded within the moisture plume were two PW maxima, respectively associated with TC Wilma and TS Alpha (Fig. 5.25b). As will be discussed later in section 5.3.4.2, both of these storms likely contributed deep moisture to the environment of the PRE. Inland along the eastern U.S. coast on the cool side of the 925-hPa baroclinic zone, conditions were considerably drier, with PW values of 10–15 mm (Fig. 5.25b). The juxtaposition of the moist and dry air masses resulted in a strong PW gradient across the baroclinic zone. The PRE developed northeastward of TC Wilma in the presence of PW values of 50–60 mm on the moist side of this PW boundary (Fig. 5.25b).

### *5.3.4 Processes leading to heavy rainfall*

#### 5.3.4.1 Lifting mechanisms

The development and growth of the PRE during 1800 UTC 23 October–1200 UTC 24 October occurred as the 850-hPa cyclonic circulation associated with TC Wilma interacted with an 850-hPa baroclinic zone that trailed behind a midlatitude cyclone situated off the coast of New England south of Newfoundland (Figs. 5.26a–d). Between 1800 UTC 23 October and 0600 UTC 24 October, as TC Wilma translated into the eastern Gulf of Mexico, southerly flow on the eastern flank of the TC circulation impinged upon the baroclinic zone, establishing warm-air advection over northern Florida and along the Georgia coast (Figs. 5.26a–c). Cold-air advection associated with

northerly and northwesterly 850-hPa flow was also present over Alabama, Georgia, and South Carolina on the cool side of the 850-hPa baroclinic zone (Figs. 5.26a–c). The juxtaposition of cold-air advection and warm-air advection along the baroclinic zone resulted in an enhanced potential temperature gradient and enhanced baroclinicity within the PRE region.

By 0600 UTC 24 October, the TC Wilma circulation had begun to strongly impinge upon the baroclinic zone, producing overlapping bands of strong warm-air advection and frontogenesis stretching along the southeastern U.S. coast over the PRE region (Fig. 5.26c). Additionally, southerly flow on the western flank of an 850-hPa anticyclone to the east of TC Wilma helped to establish an elongated region of warm-air advection that extended along the baroclinic zone well poleward and eastward of the PRE region (Fig. 5.26c). This elongated region of warm-air advection was colocated with the large cloud shield, shown in Fig. 5.23c, that extended from TC Wilma poleward along the eastern U.S. coast. A vertical cross section taken through the PRE at 0600 UTC 24 October shows that poleward low-level flow ascended along the poleward sloping low-level baroclinic zone (consistent with 850-hPa warm-air advection) in the presence of frontogenesis and within a plume of moisture extending from TC Wilma (Fig. 5.27). Above the low-level baroclinic zone, ascent extended from 700 hPa to 250 hPa beneath the equatorward entrance region of the upper-tropospheric jet streak situated poleward of the PRE region (Fig. 5.27).

During 0600–1200 UTC 24 October, the TC Wilma circulation moved northeastward across southern Florida and began to become embedded in the 850-hPa baroclinic zone situated along the southeastern U.S. coast, establishing a region of strong

warm-air advection that extended poleward from the center of TC Wilma along the baroclinic zone (Figs. 5.26c,d). The locus of maximum warm-air advection and frontogenesis shifted poleward along the North Carolina coast (Figs. 5.26c,d), likely contributing to the observed poleward expansion of the heavy precipitation associated with the PRE (Figs. 5.24d,e).

5.3.4.2 Moisture contributions from TC Wilma and TS Alpha

During 1800 UTC 23 October–0600 UTC 24 October, a corridor of strong poleward 1000–100-hPa VIMF, extending along the eastern flank of the TC Wilma circulation from the Caribbean toward the southeastern U.S. coast, contributed to the poleward progression of deep moisture plumes, with PW values of 55–60 mm, from TC Wilma and TS Alpha, respectively, toward the PRE region (Figs. 5.28a–c). By 0600 UTC, these two plumes of deep moisture had merged within the PRE region, and strong VIMF convergence had developed along the Georgia, South Carolina, and North Carolina coastlines (Fig. 5.28c). This region of maximum VIMF convergence coincided with the heaviest precipitation associated with the PRE, depicted in the radar imagery in Fig. 5.24d. Between 0600 UTC and 1200 UTC 24 October, the combined TC Wilma and TS Alpha moisture plumes (PW values of 55–60 mm) in place over the PRE region surged farther poleward along the southeastern U.S. coast, while VIMF convergence intensified along the North Carolina coast. This poleward surge of the moisture and concomitant intensification of VIMF convergence likely contributed to the observed poleward expansion of the PRE along the North Carolina coast (Figs. 5.24d,e).

Fifteen 36-h backward kinematic air parcel trajectories ending in the PRE region at 600 hPa at 0600 UTC 24 October were computed in order to determine the source regions of air parcels entering the PRE region. The trajectories indicate that air parcels entering the PRE region at 0600 UTC 24 October originated over the Caribbean Sea within a region of deep moisture (PW values of 45–60 mm) that was in place at 1800 UTC 22 October on the eastern flank of TC Wilma and to the northwest of TS Alpha (Fig. 5.29). Air parcels ending on the western flank and near the center of the PRE generally originated at lower levels on the eastern flank of the TC Wilma moisture plume and subsequently accelerated poleward, ascending as they entered the PRE region (Fig. 5.29). Air parcels ending to the south and east of the PRE (e.g., trajectories 4, 5, and 10) originated at midlevels to the northwest of TS Alpha and exhibited little vertical displacement as they entered the PRE region (Fig. 5.29). The air parcels originating northwest of TS Alpha remained moist, with relative humidity and mixing ratio values remaining relatively constant at ~75% and ~6 g $kg^{-1}$, respectively, along their trajectories (not shown).

5.3.4.3 Impact of diabatic heating on the upper-tropospheric flow

Between 1800 UTC 23 October and 1800 UTC 24 October, the development of the PRE and its subsequent merger with TC Wilma (Figs. 5.24a–e) occurred in conjunction with substantial changes in the structure, orientation, and strength of the 200-hPa jet streak situated poleward of the PRE region during this time period (Fig. 5.30). At 1800 UTC 23 October, the developing PRE was situated within the equatorward entrance region of the previously mentioned straight southwesterly jet streak, with 200-hPa

irrotational flow in the entrance region directed poleward and westward toward the cyclonic shear side of the jet streak (Fig. 5.30a). During 1800 UTC 23 October–0600 UTC 24 October, as the PRE expanded and intensified (Figs. 5.24a–d), strong diabatically driven divergent outflow from the PRE developed (Figs. 5.30a,b), as manifested by strong irrotational flow emanating from a band of strong 700-hPa ascent over the PRE region (Figs. 5.30a,b). Meanwhile, pronounced divergent outflow associated with northeastward-moving TC Wilma was present to the southwest of the PRE region (Figs. 5.30a,b).

The amalgamation of the divergent outflow configurations respectively associated with TC Wilma and the PRE during the period between 1800 UTC 23 October and 0600 UTC 24 October established poleward and westward advection of low 250–200-hPa PV air from the vicinity of the TC and PRE along the axis of the jet streak (Figs. 5.30a,b). In association with this negative advection of PV, the jet streak developed anticyclonic curvature, and PV gradients along the axis of the jet streak were strengthened (Figs. 5.30a,b). By 0600 UTC 24 October, the strengthened PV gradients had led to increased wind speeds within the jet streak, accompanied by strengthened along-flow wind speed gradients within the entrance region (Fig. 5.30b). The evolution of the jet streak in response to the PRE and TC outflow occurred in conjunction with the development of the band of strong ascent associated with the intensifying PRE (Figs. 5.30a,b).

Between 0600 UTC and 1800 UTC 24 October, in response to the continued poleward and westward advection of low-PV air by the divergent outflow from TC Wilma and the PRE, the jet streak continued to strengthen and acquired pronounced anticyclonic curvature (Figs. 5.30b–d). Meanwhile, an axis of high PV associated with a

deep trough approached the jet streak from the west (Figs. 5.30b–d). The approach of this axis of high PV, combined with the low-PV outflow (and concomitant ridge amplification) associated with TC Wilma and the PRE, acted to strengthen the PV gradient along the axis of the jet streak, leading to a substantial increase in maximum wind speeds, from 75–80 m $s^{-1}$ at 0600 UTC to 90–95 m $s^{-1}$ at 1800 UTC, and to strengthened along-flow wind speed gradients in the entrance region (Figs. 5.30b–d). During 0600–1800 UTC 24 October, the strengthening of along-flow wind speed gradients and the development of pronounced anticyclonic curvature along the jet streak were coincident with the enhancement and broadening of ascent along and to the east of the North Carolina coast (Figs. 5.30b–d). This enhanced ascent, in turn, was linked to the observed expansion and intensification of the heavy precipitation associated with the PRE along the North Carolina coast during this time period (Figs. 5.24d–f).

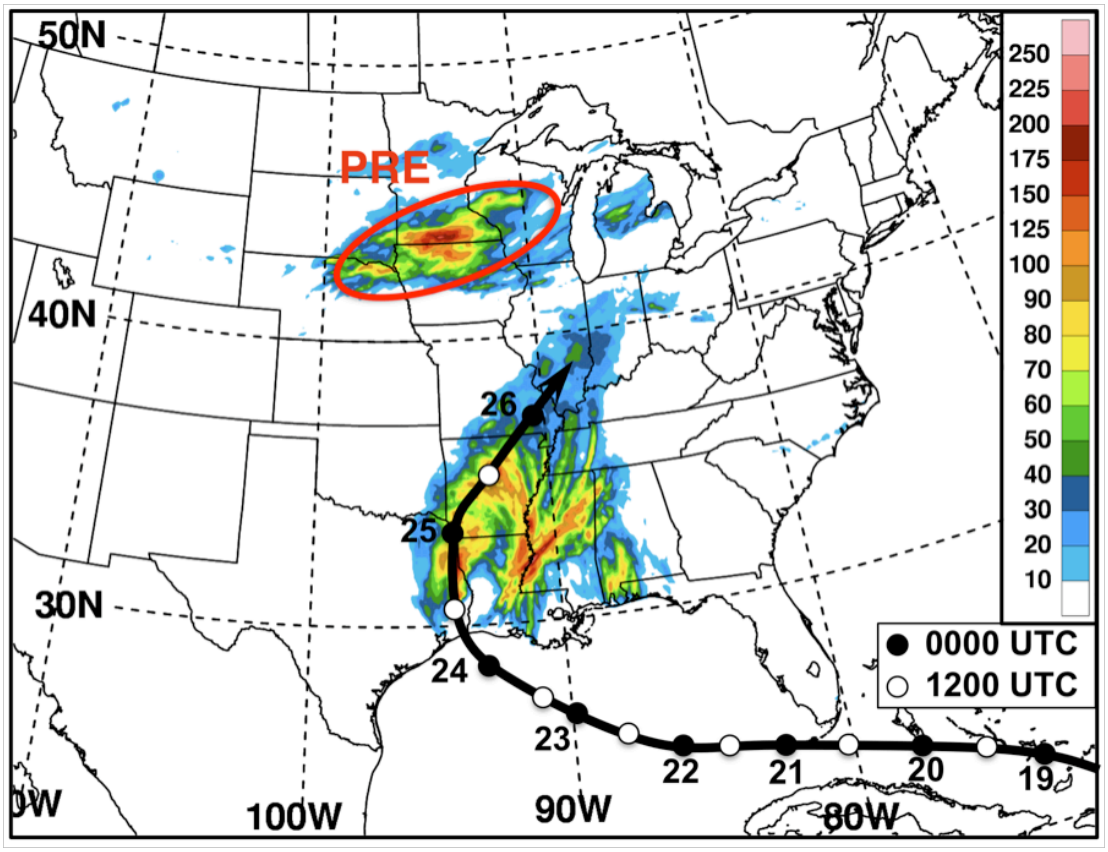


Figure 5.1: The NHC Best Track positions for TC Rita during 19–26 September 2005 overlaid on the NPVU QPE analysis (shaded in mm according to the color bar) for 1200 UTC 24 September–0000 UTC 26 September 2005. The filled (unfilled) circles denote the 0000 UTC (1200 UTC) TC positions.

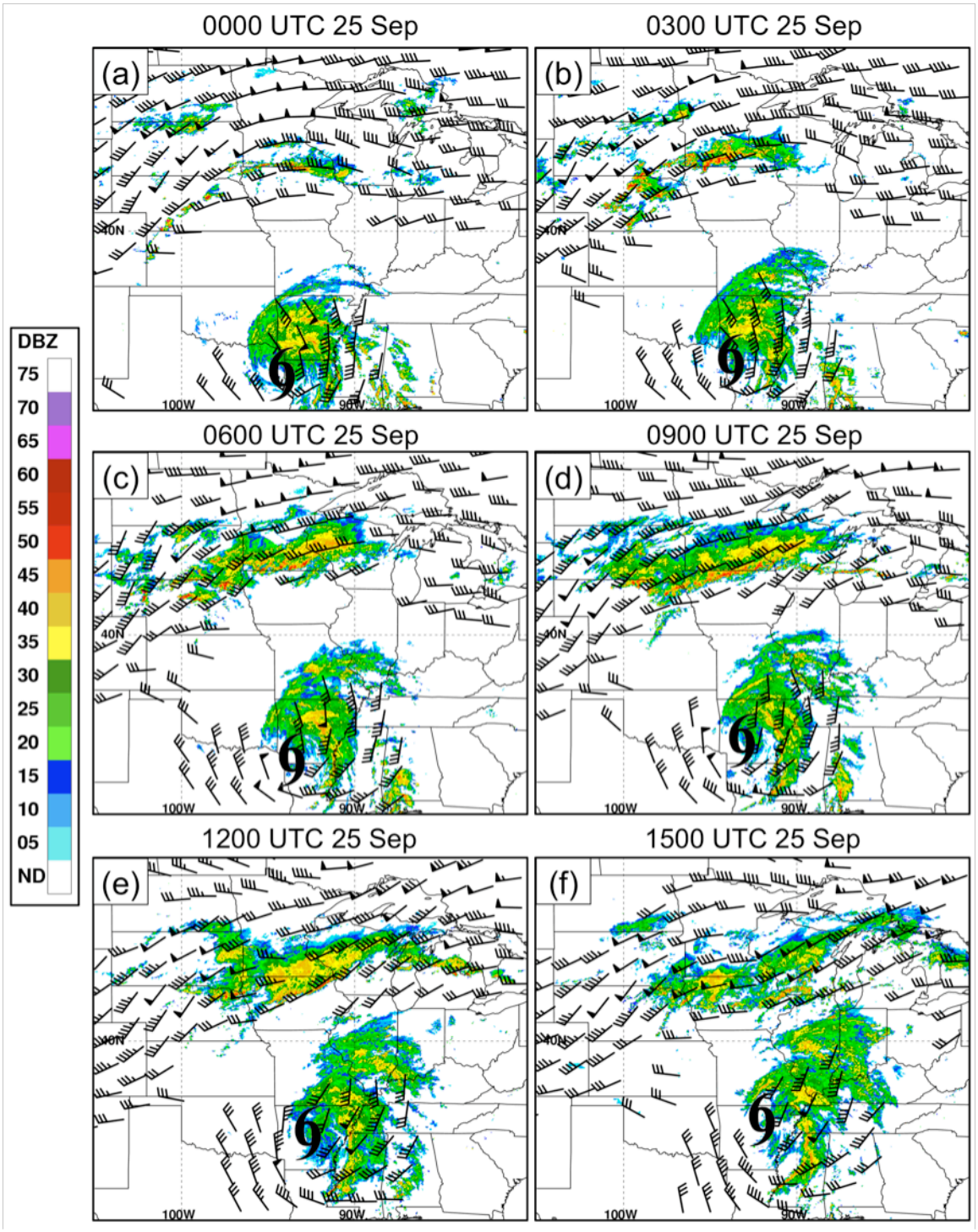


Figure 5.2: WSI NOWrad radar reflectivity mosaics (shaded every 5 dBZ ) and 1000–500-hPa vertical wind shear ≥ 15 m $s^{-1}$ (half barb: 2.5 m $s^{-1}$; full barb: 5 m $s^{-1}$; pennant: 25 m $s^{-1}$) calculated from the NCEP 20-km RUC analyses at (a) 0000 UTC, (b) 0300 UTC, (c) 0600 UTC, (d) 0900 UTC, (e) 1200 UTC, and (f) 1500 UTC 25 September 2005. The TC location is denoted by the tropical storm symbol.

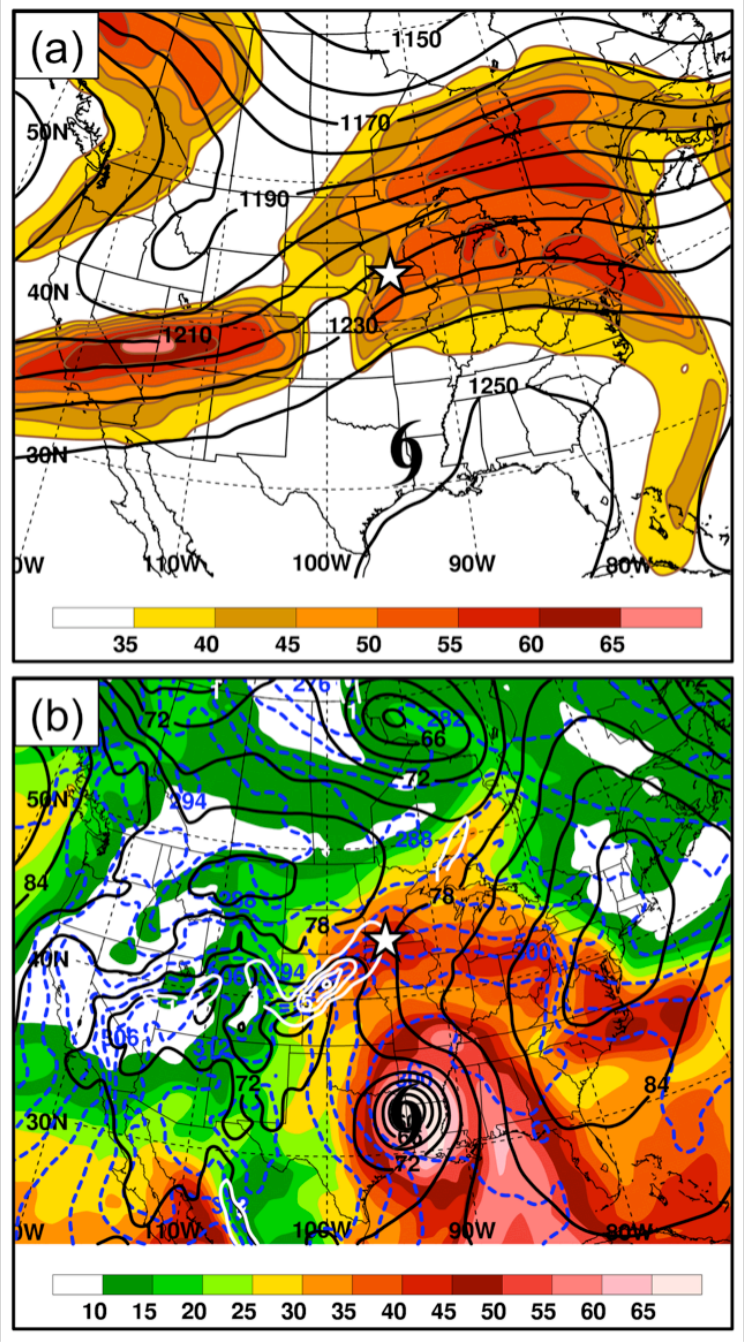


Figure 5.3: NCEP 1° GFS analysis at 0000 UTC 25 September of: (a) 200-hPa geopotential height (contoured in black every 10 dam) and wind speed (shaded in m $s^{-1}$ according to the color bar); (b) total PW (shaded in mm according to the color bar) overlaid with 925-hPa geopotential height (contoured in black every 3 dam), potential temperature (contoured in blue every 3 K), and Petterssen frontogenesis [contoured in white every 2 K $(100\ km)^{-1}$ $(3\ h)^{-1}$ starting at 1 K $(100\ km)^{-1}$ $(3\ h)^{-1}$]; and (c) 700-hPa geopotential height (contoured in black every 3 dam), potential temperature (contoured in red every 3 K), **Q** vectors ($10^{-11}$ K $m^{-1}$ $s^{-1}$; reference vector at the bottom of the panel), and **Q**-vector divergence (shaded in $10^{-15}$ K $m^{-2}$ $s^{-1}$ according to the color bar). The TC and PRE locations are denoted by the tropical storm symbol and the star, respectively.

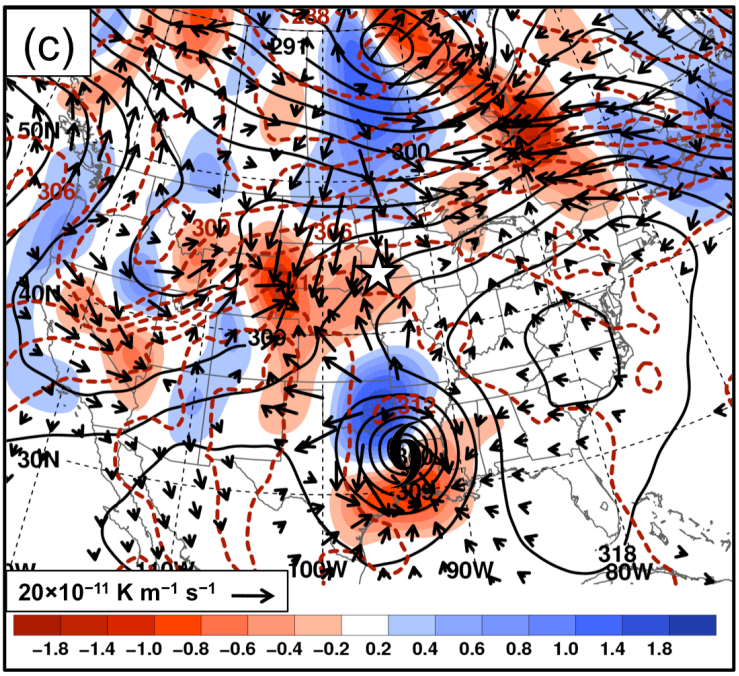
(c)
288
291
50N
300
306
305
306
40N
309
312
30N
309
318
80W
70W
90W
20×10⁻¹¹ K m⁻¹ s⁻¹
−1.8 −1.4 −1.0 −0.8 −0.6 −0.4 −0.2 0.2 0.4 0.6 0.8 1.0 1.4 1.8

*Fig. 5.3 (cont.)*

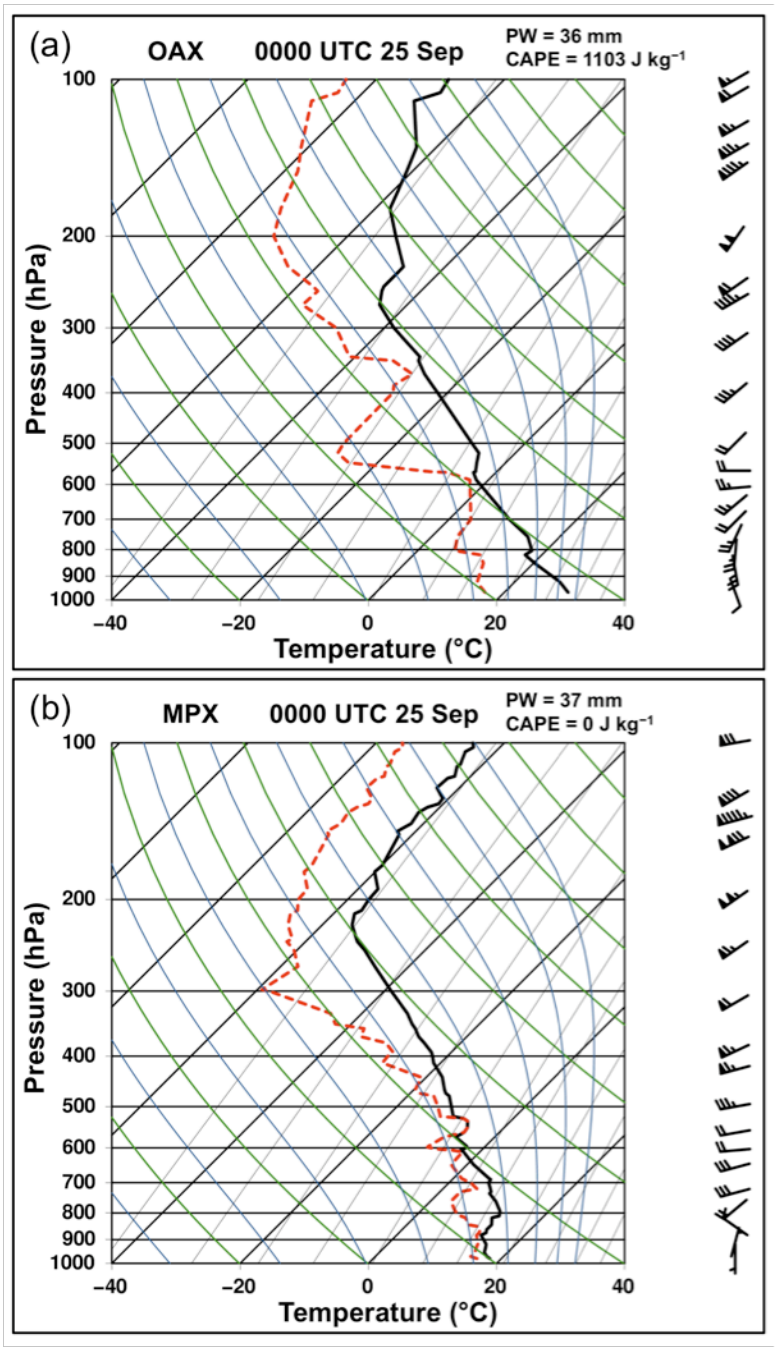


Figure 5.4: Skew *T*–log *p* plots showing temperature (black line in °C), dewpoint (dashed red line in °C), and wind (barbs in m $s^{-1}$ according to the convention in Fig. 5.2) at 0000 UTC 25 September 2005 for (a) Omaha, NE (OAX), and (b) Chanhassen, MN (MPX). The PW and CAPE values for each location are indicated at the top of each panel.

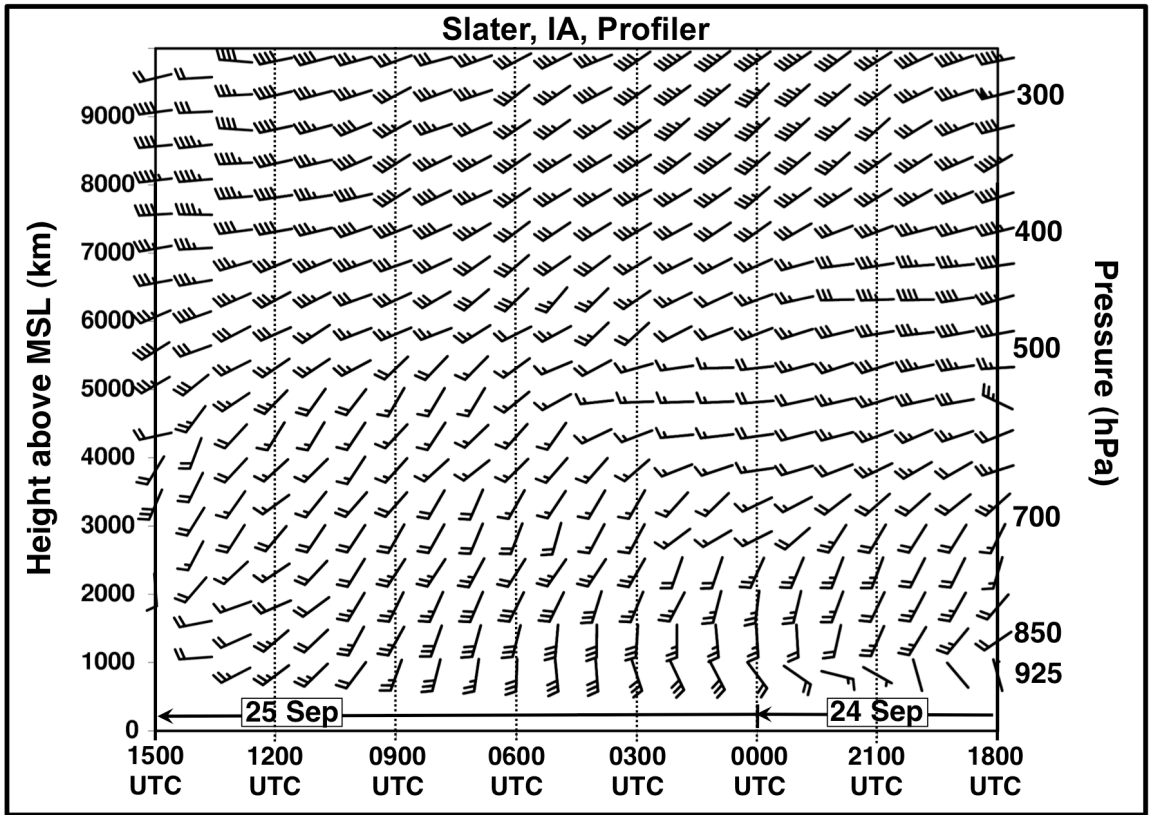


Figure 5.5: Time–height (km MSL) section showing NOAA profiler winds (barbs in m $s^{-1}$ according to the convention in Fig. 5.2) at Slater, IA (SLA) during 1800 UTC 24 September–1500 UTC 25 September 2005. Time (UTC) goes from right to left.

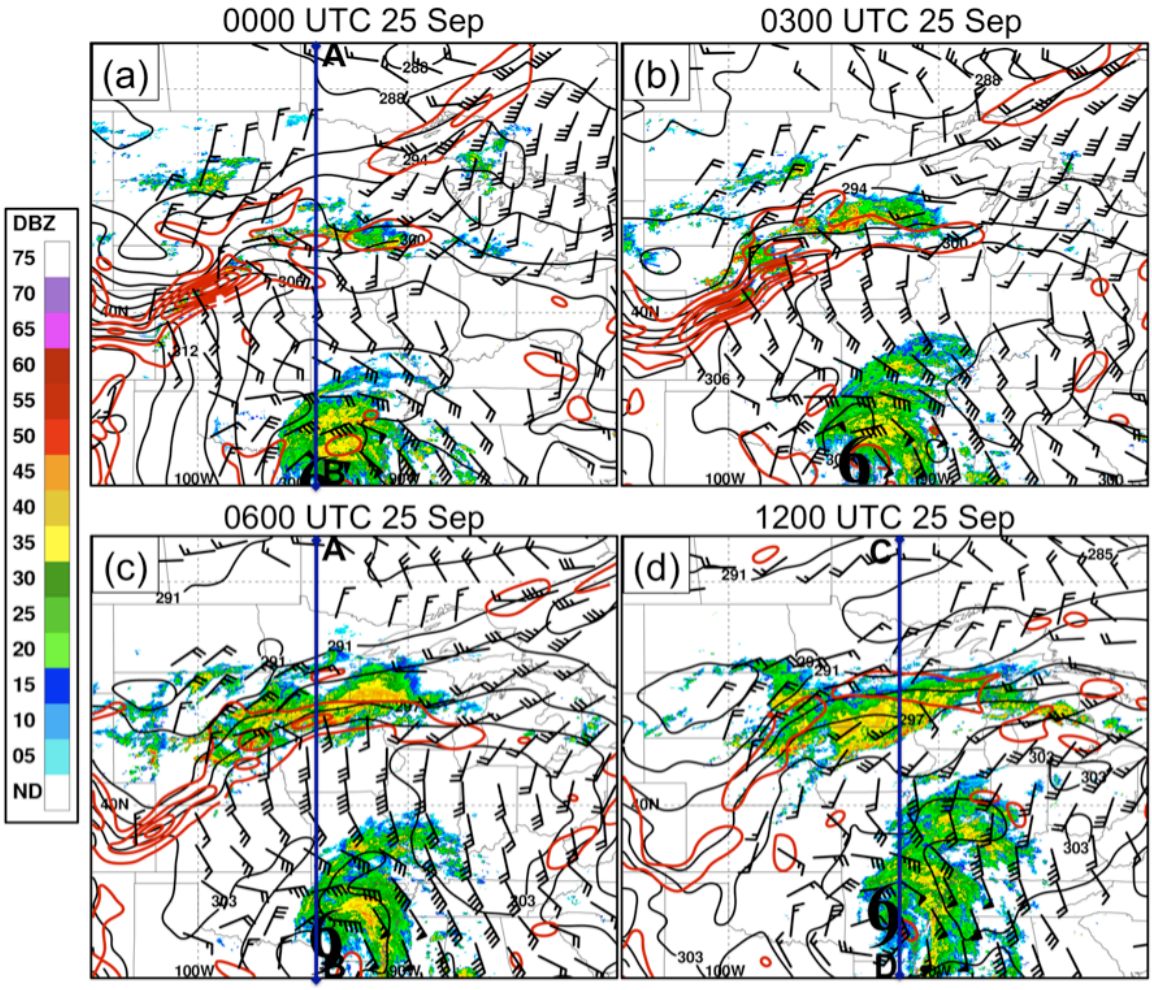


Figure 5.6: NCEP 20-km RUC analyses of 925-hPa potential temperature (contoured in gray every 3 K), Petterssen frontogenesis [contoured in red every 3 K (100 km)$^{-1}$ (3 h)$^{-1}$ starting at 1 K (100 km)$^{-1}$ (3 h)$^{-1}$], and winds ≥ 7.5 m s$^{-1}$ (barbs according to the convention in Fig. 5.2) overlaid on WSI NOWrad radar reflectivity mosaics (shaded in dB*Z* according to the color bar) at (a) 0000 UTC, (b) 0300 UTC, (c) 0600 UTC, and (d) 1200 UTC September 2005. Cross sections A–B and C–D are indicated in panels (c) and (d). The TC location is denoted by the tropical storm symbol.

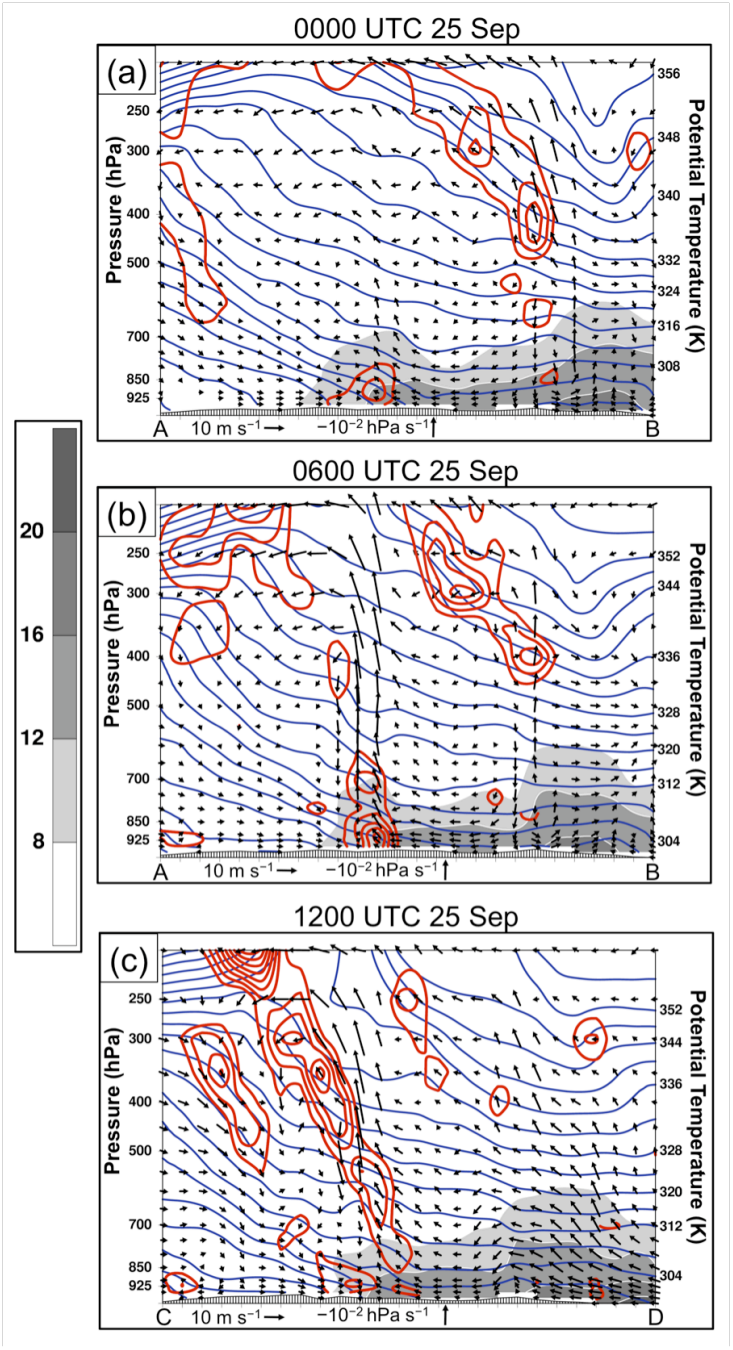


Figure 5.7: Vertical cross sections generated from the NCEP 1° GFS analyses showing potential temperature (contoured in blue every 3 K), Petterssen frontogenesis [contoured in red every 2 K (100 km)$^{-1}$ (3 h)$^{-1}$ starting at 1 K (100 km)$^{-1}$ (3 h)$^{-1}$], mixing ratio (shaded in g kg$^{-1}$ according to the color bar), and the flow in the plane of the cross section (vectors with the horizontal component in m s$^{-1}$ and the vertical component in hPa s$^{-1}$; reference vectors are at the bottom of each panel) at (a) 0000 UTC, (b) 0600 UTC, and (c) 1200 UTC 25 September 2005. The cross-section locations are indicated in Figs. 5.6a,c,d, respectively.

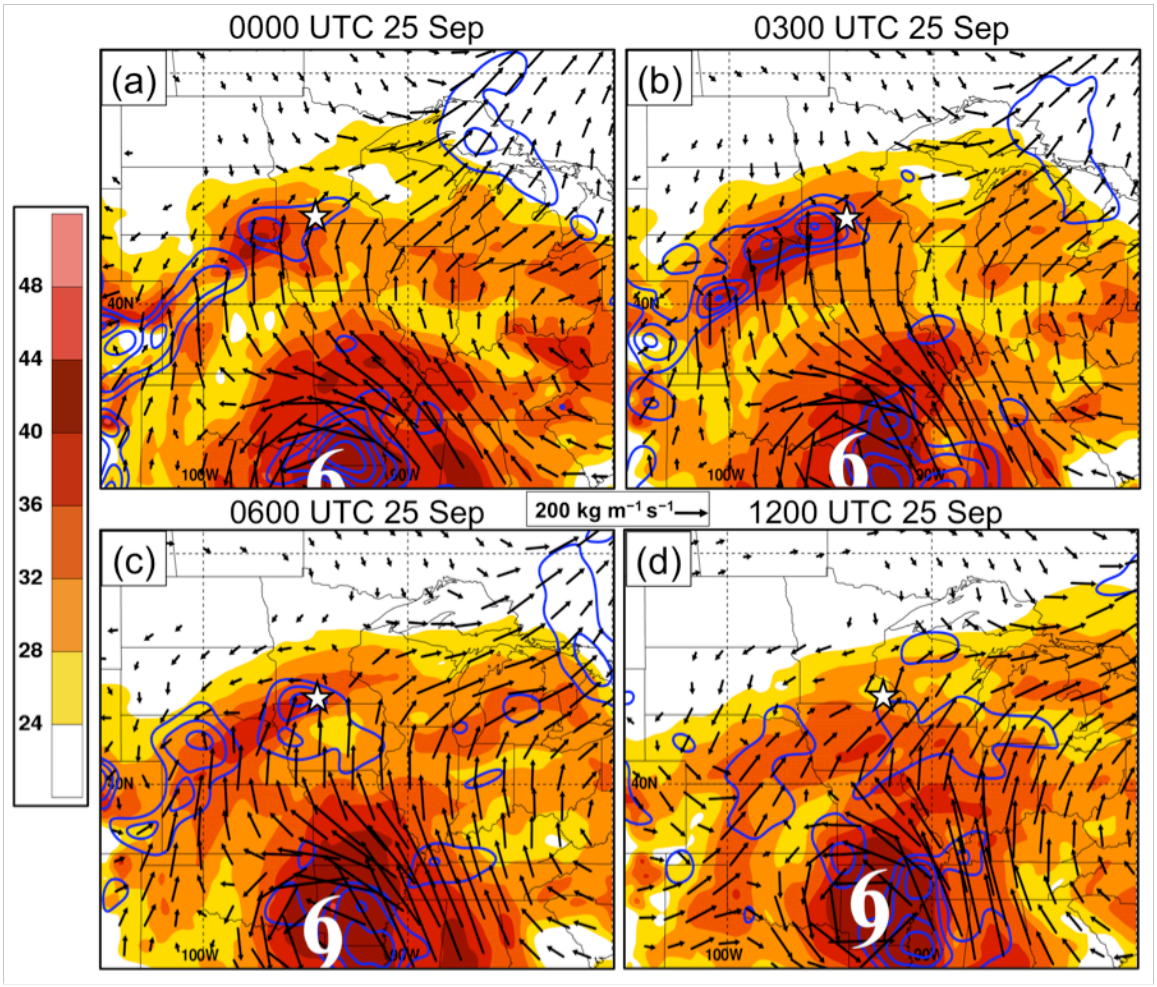


Figure 5.8: 1000–700-hPa PW (shaded in mm according to the color bar), VIMF vectors (kg $m^{-1}$ $s^{-1}$; reference vector in the center), and VIMF convergence (contoured in blue every $5 \times 10^{-4}$ kg $m^{-2}$ $s^{-1}$ starting at $-5 \times 10^{-4}$ kg $m^{-2}$ $s^{-1}$) generated from the 20-km RUC analyses at (a) 0000 UTC, (b) 0300 UTC, (c) 0600 UTC, and (d) 1200 UTC September 2005. The centroid of the PRE is marked by the white star, and the TC location is denoted by the tropical storm symbol.

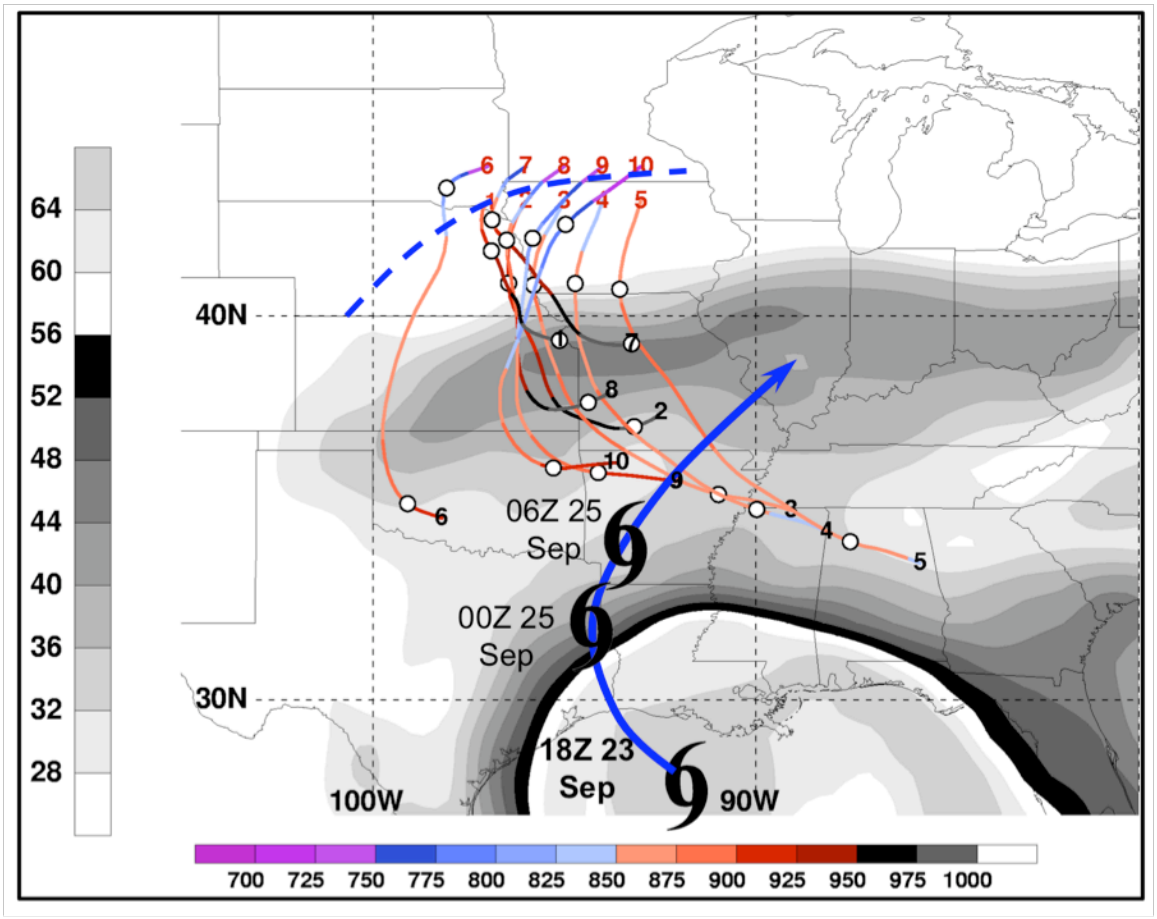


Figure 5.9: Ten 36-h backward kinematic air parcel trajectories ending within the PRE region at 0600 UTC 25 September 2005 overlaid on the NCEP 1° GFS total PW analysis at 1800 UTC 23 September 2005 (shaded in mm according to the color bar on the left). The red (black) numbers denote the ending (beginning) point of each trajectory. Trajectories 1–5 begin at 850 hPa and trajectories 6–10 begin at 700 hPa. The white circles mark the 0000 UTC 25 September and 0000 UTC 24 September air parcel positions. The air parcel pressure values (hPa) are shaded according to the color bar at the bottom. For reference, the track of TC Rita subsequent to 1800 UTC 23 September 2005 is indicated by the blue arrow, and the positions of TC Rita at 1800 UTC 23 September, 0000 UTC 25 September, and 0600 UTC September 2005 are marked by the tropical storm symbols. The dashed blue line indicates the location of the 925-hPa baroclinic zone at 0600 UTC 25 September.

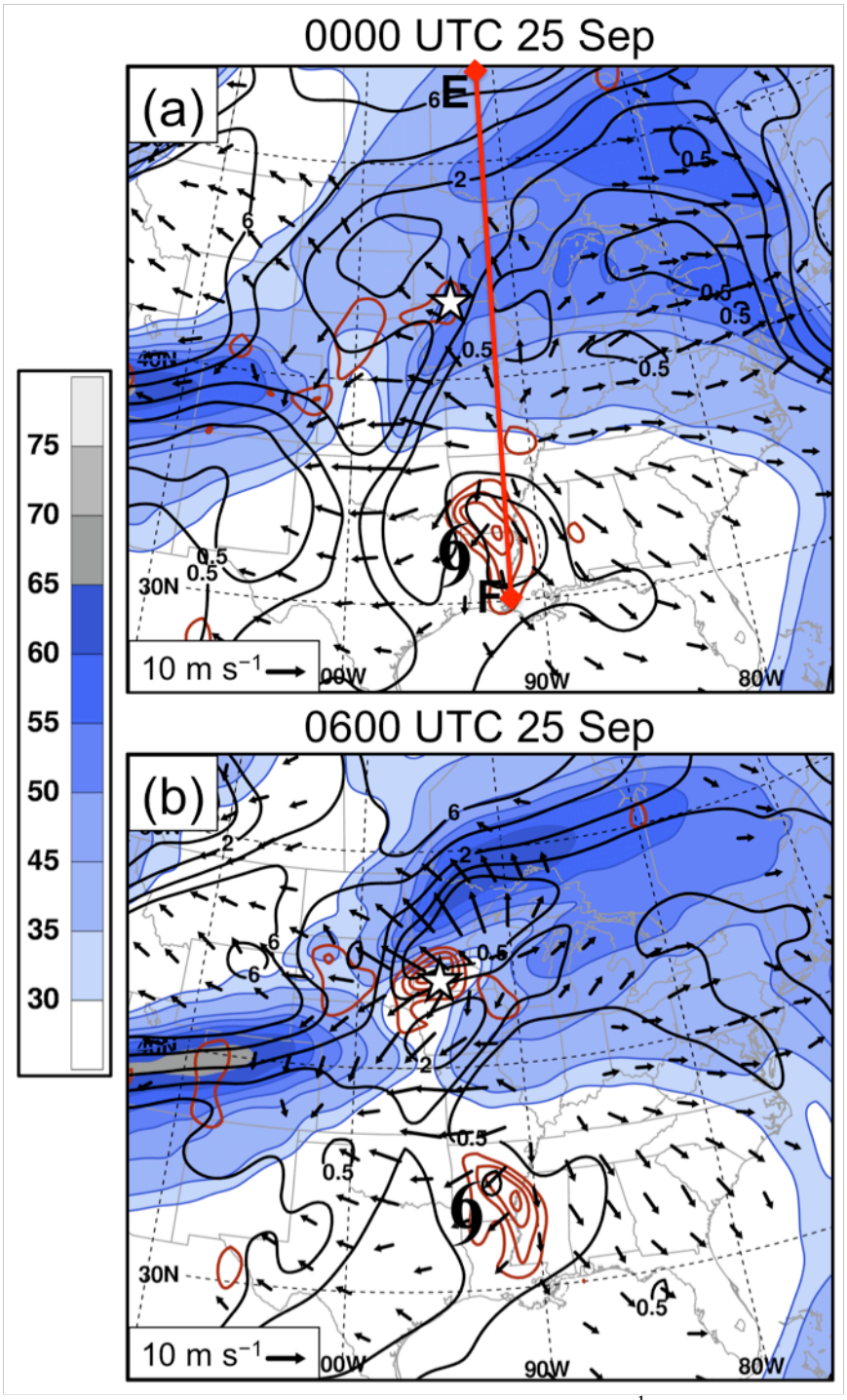


Figure 5.10: 200-hPa irrotational wind vectors (> 5 m $s^{-1}$; reference vector is at the bottom of each panel), 200-hPa wind speed (shaded in m $s^{-1}$ according to the color bar ), 700-hPa ascent (contoured in red every $5 \times 10^{-3}$ hPa $s^{-1}$ starting at $-5 \times 10^{-3}$ hPa $s^{-1}$), and 250–200-hPa PV (0.5, 1, 2, 4, and 6 PVU contours shown in black) generated from the NCEP 1° GFS analyses at (a) 0000 UTC, (b) 0600 UTC, and (c) 1200 UTC 25 September 2005. The TC and PRE locations are denoted by the tropical storm symbol and the star, respectively. Cross-section E–F is indicated in panels (a) and (c).

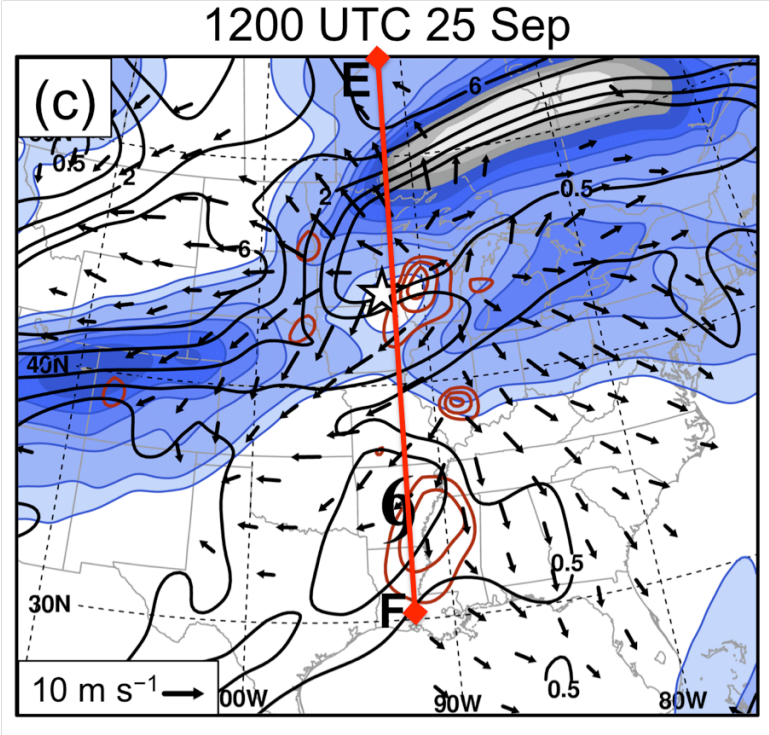


*Fig. 5.10 (cont.)*

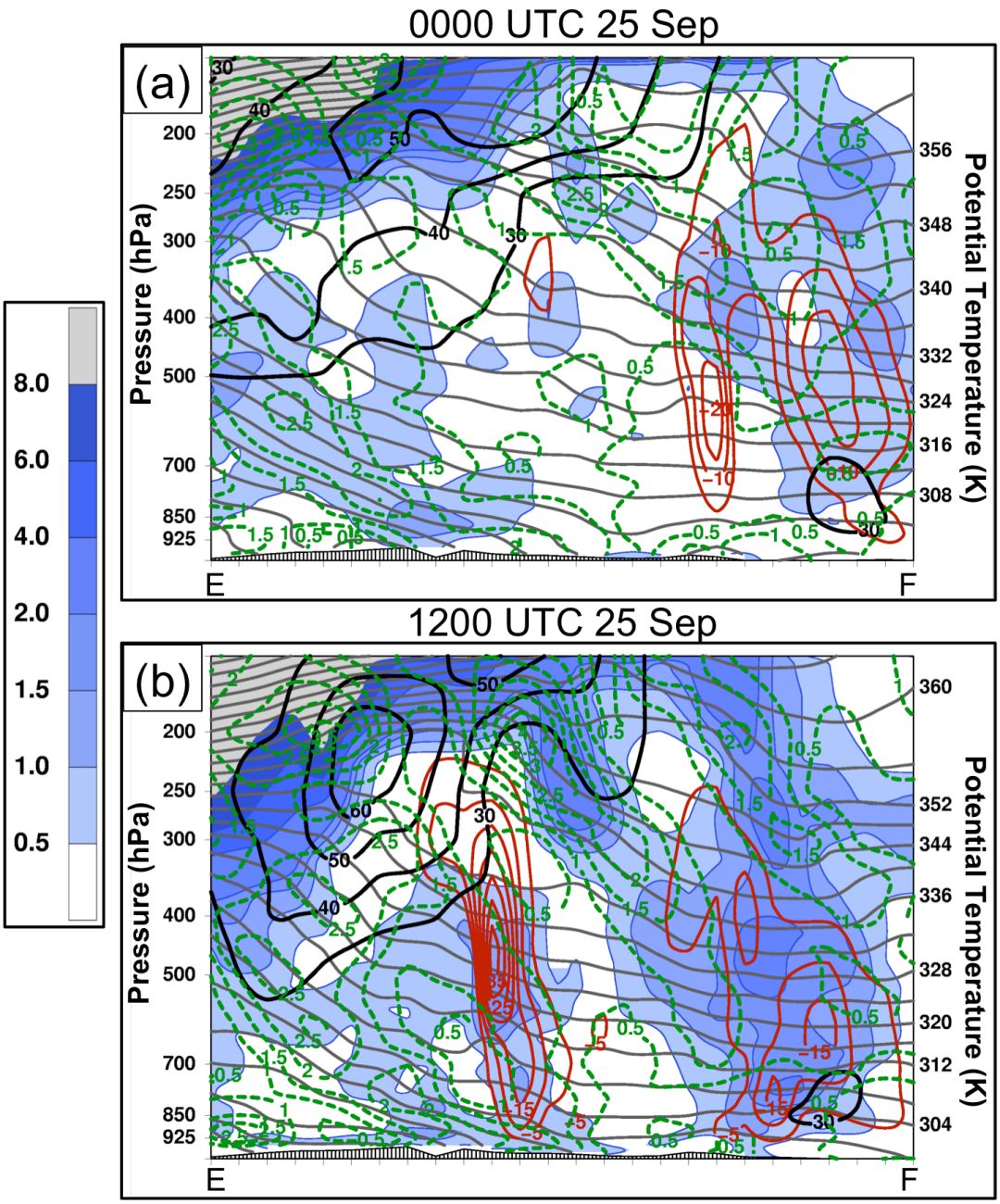


Figure 5.11: Vertical cross sections generated from the NCEP 1° GFS analyses showing potential temperature (contoured in gray every 3 K), ascent (contoured in red every 5 × $10^{-3}$ hPa $s^{-1}$ starting at −5 × $10^{-3}$ hPa $s^{-1}$), PV (shaded in PVU according to the color bar), and horizontal wind speed (contoured in black every 10 m $s^{-1}$ starting at 30 m $s^{-1}$) at (a) 0000 UTC and (b) 1200 UTC 25 September 2005. Panel (b) also shows positive 12-h potential temperature changes (contoured in green every 0.5 K starting at 1 K and every 1 K starting at 3 K) between 0000 UTC and 1200 UTC 25 September. The cross-section location is indicated in Figs. 5.10a,c.

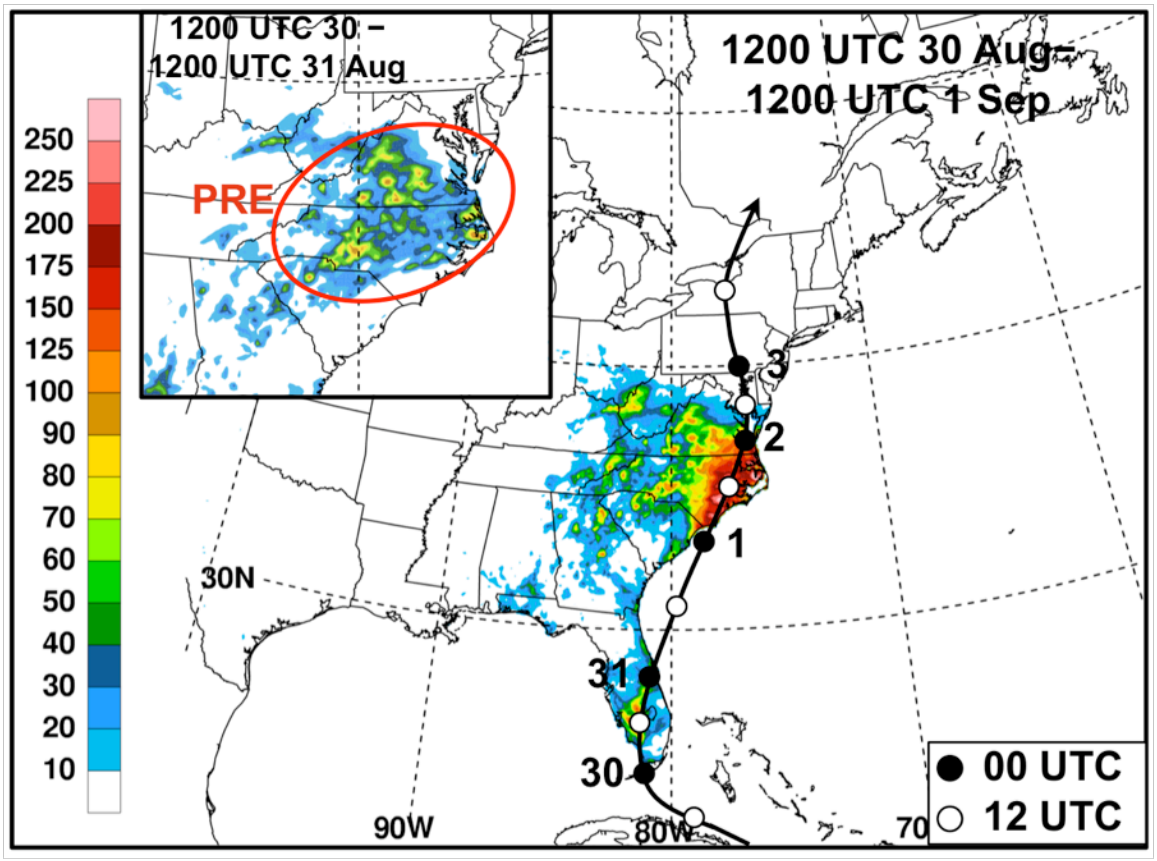


Fig. 5.12: The NHC Best Track positions for TC Ernesto during 29 August–3 September 2006 overlaid on the NPVU QPE analysis (shaded in mm according to the color bar) for 1200 UTC 30 August–1200 UTC 1 September 2006. The filled (unfilled) circles denote the 0000 UTC (1200 UTC) TC positions. The inset in the upper-left corner shows NPVU QPE analysis (shaded in mm according to the color bar) for 1200 UTC 30–1200 UTC 31 August 2006.

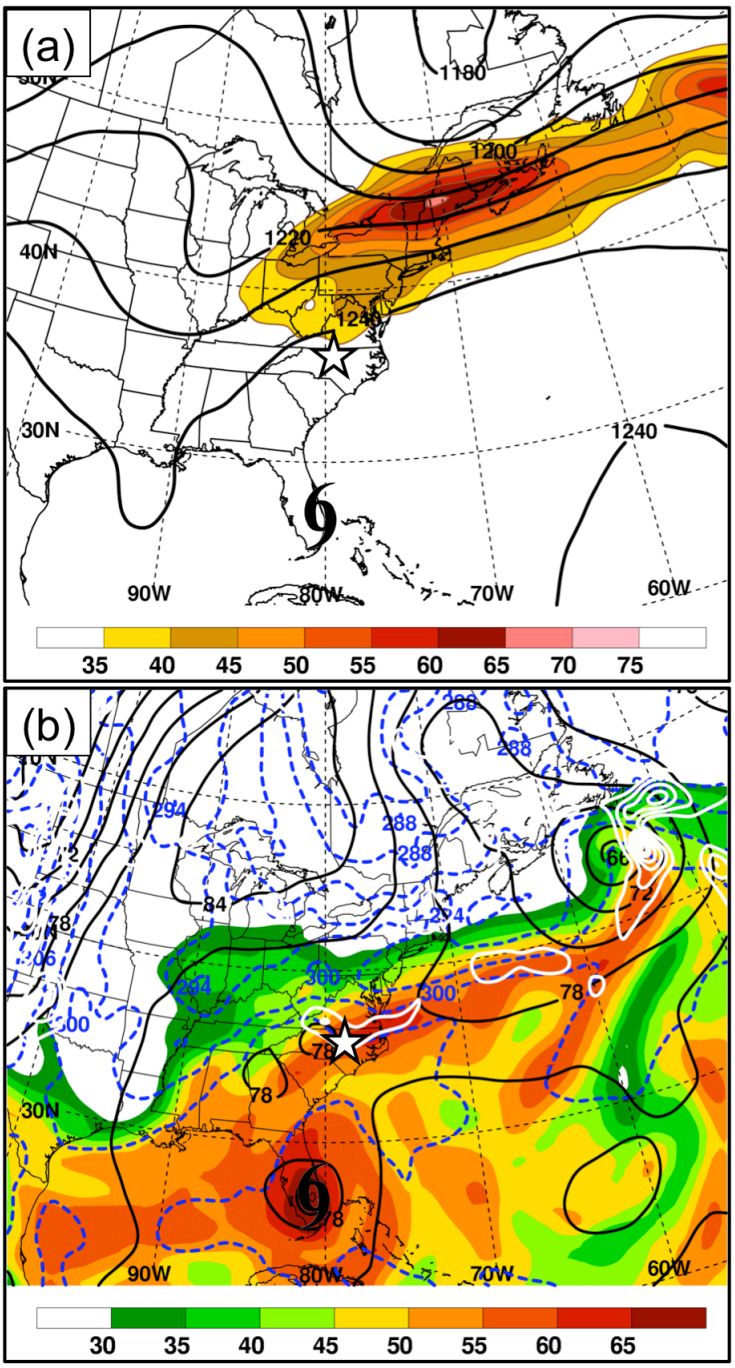


Figure 5.13: As in Fig. 5.3, except for 1800 UTC 30 August 2006.

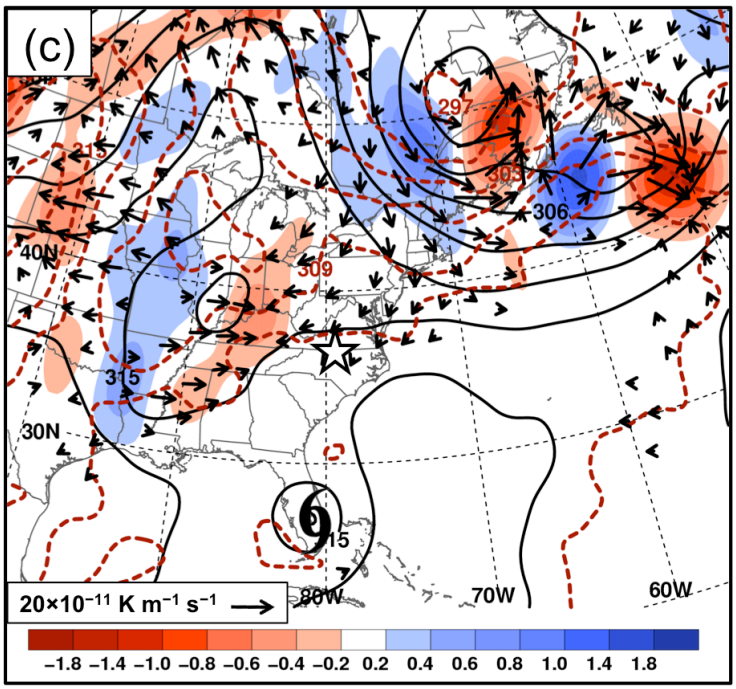
(c)
297
303
306
40N
309
315
30N
6
15
80W
70W
60W
20×10⁻¹¹ K m⁻¹ s⁻¹
−1.8 −1.4 −1.0 −0.8 −0.6 −0.4 −0.2 0.2 0.4 0.6 0.8 1.0 1.4 1.8

*Fig. 5.13 (cont.)*

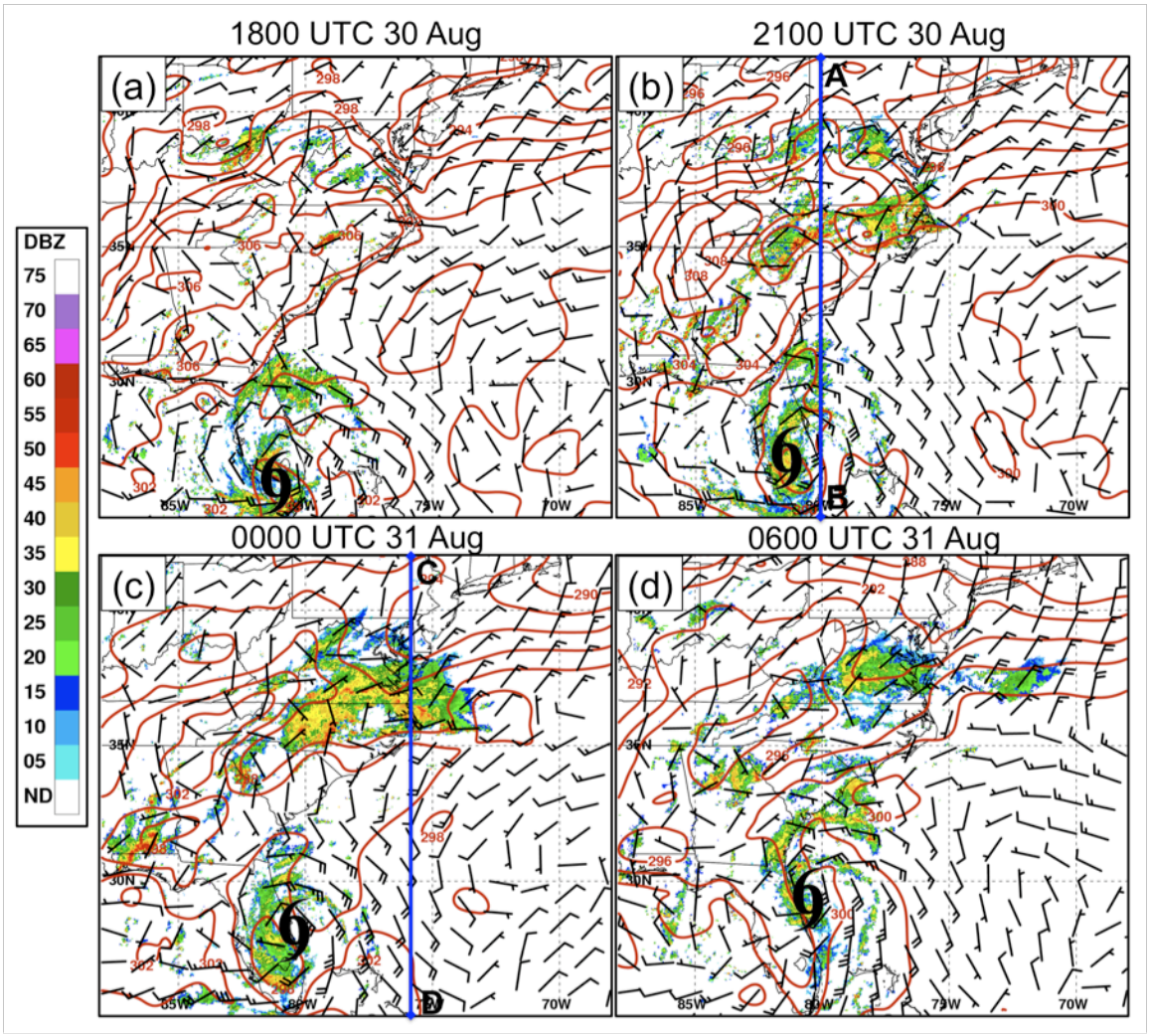


Figure 5.14: NCEP 20-km RUC analyses of 2-m potential temperature (contoured in red every 2 K) and 10-m winds (barbs in m $s^{-1}$ according to the convention in Fig. 5.2) overlaid on WSI NOWrad radar reflectivity mosaics (shaded in dB*Z* according to the color bar) at (a) 1800 UTC 30 August, (b) 2100 UTC 30 August, (c) 0000 UTC 31 August, and (d) 0600 UTC 31 August 2006. Cross sections A–B and C–D are indicated in panels (b) and (c), respectively. The TC location is denoted by the tropical storm symbol.

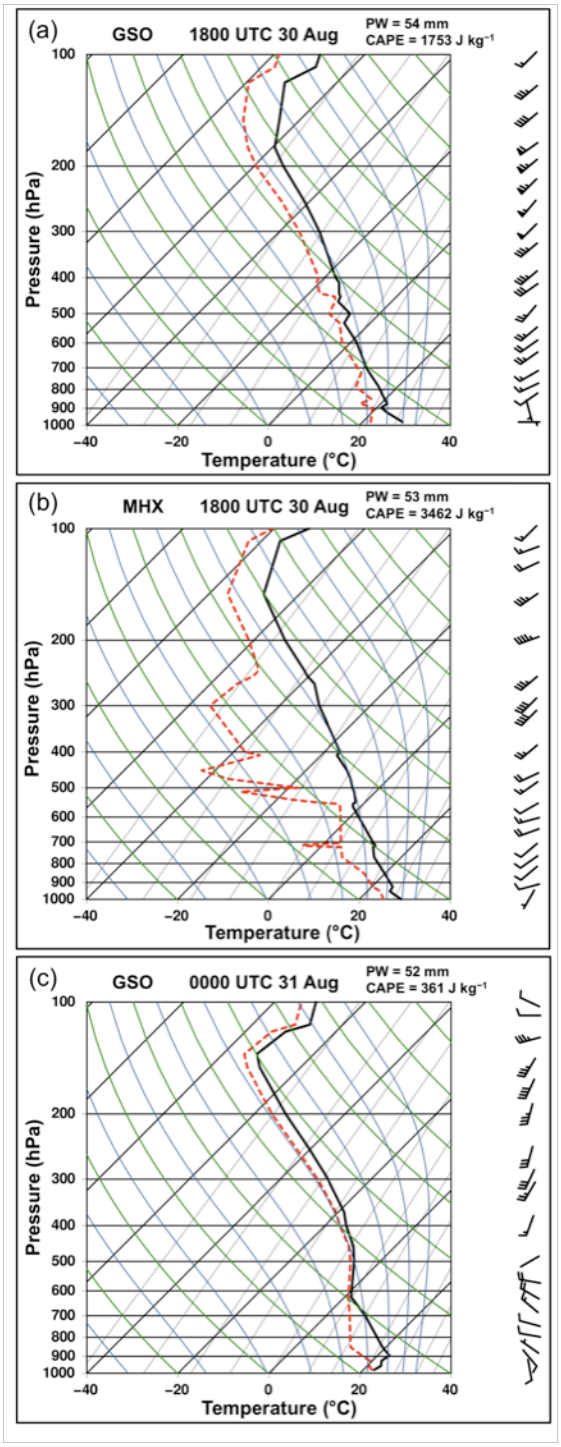


Figure 5.15: Skew *T*–log *p* plots showing temperature (black line in °C), dewpoint (dashed red line in °C), and winds (barbs in m $s^{-1}$ according to the convention in Fig. 5.2) at 1800 UTC 30 August 2006 for (a) Greensboro, NC (GSO), and (b) Newport, NC (MHX), and at (c) 0000 UTC 31 August 2006 for GSO. The PW and CAPE values for each location are indicated at the top of each panel.

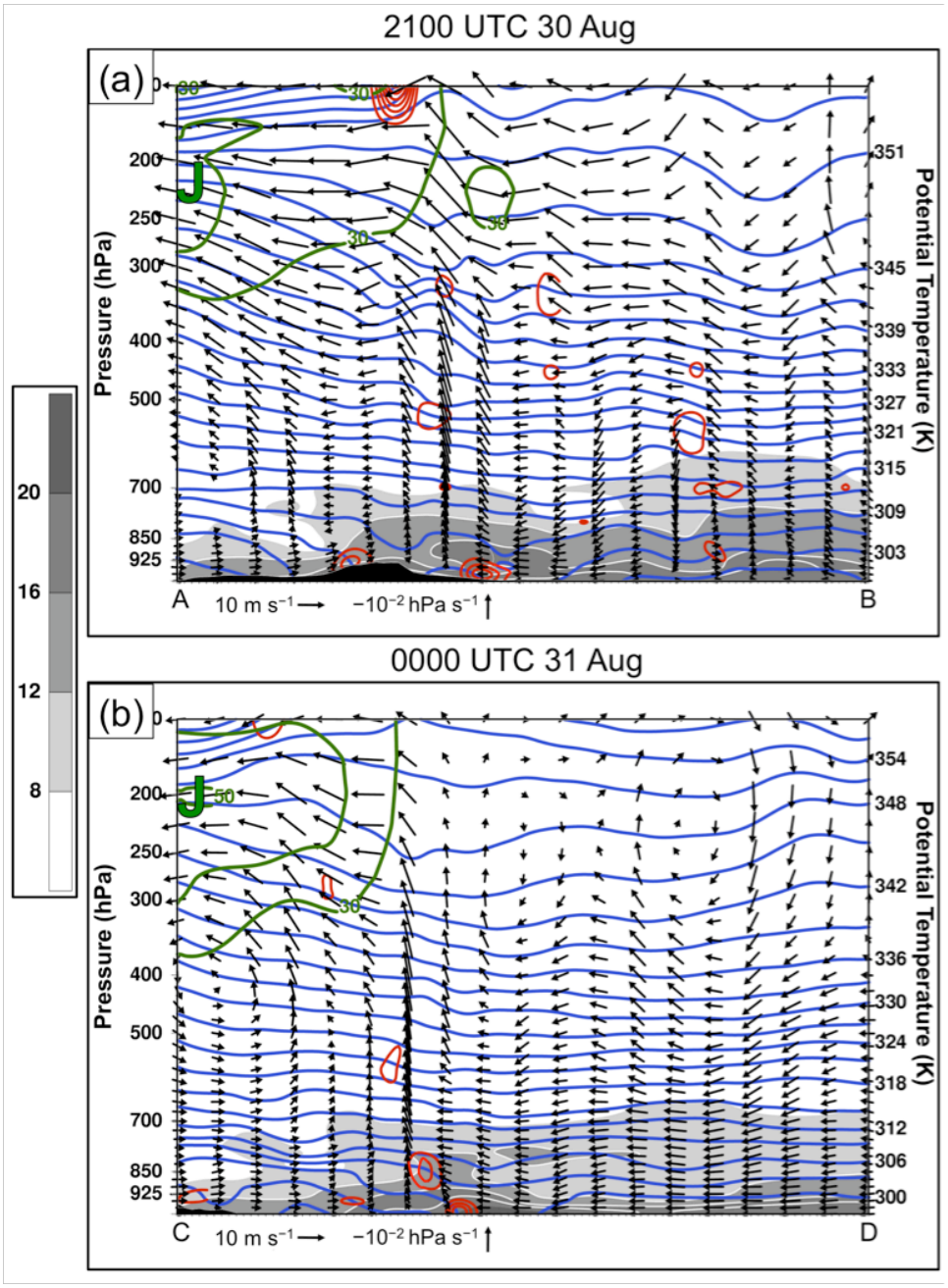


Figure 5.16: Vertical cross sections generated from the NCEP 20-km RUC analyses showing potential temperature (contoured in blue every 3 K), Petterssen frontogenesis [contoured in red every 2 K (100 km)$^{-1}$ (3 h)$^{-1}$ starting at 1 K (100 km)$^{-1}$ (3 h)$^{-1}$], mixing ratio (shaded in g kg$^{-1}$ according to the color bar), horizontal wind speed (contoured in green every 10 m s$^{-1}$ starting at 30 m s$^{-1}$), and the flow in the plane of the cross section (vectors with the horizontal component in m s$^{-1}$ and the vertical component in hPa s$^{-1}$; reference vectors are at the bottom of each panel) at (a) 1800 UTC 31 August and (b) 0000 UTC 31 August 2006. The green "J" indicates the location of maximum horizontal wind speed. The cross section locations are indicated in Figs. 5.14b,c, respectively.

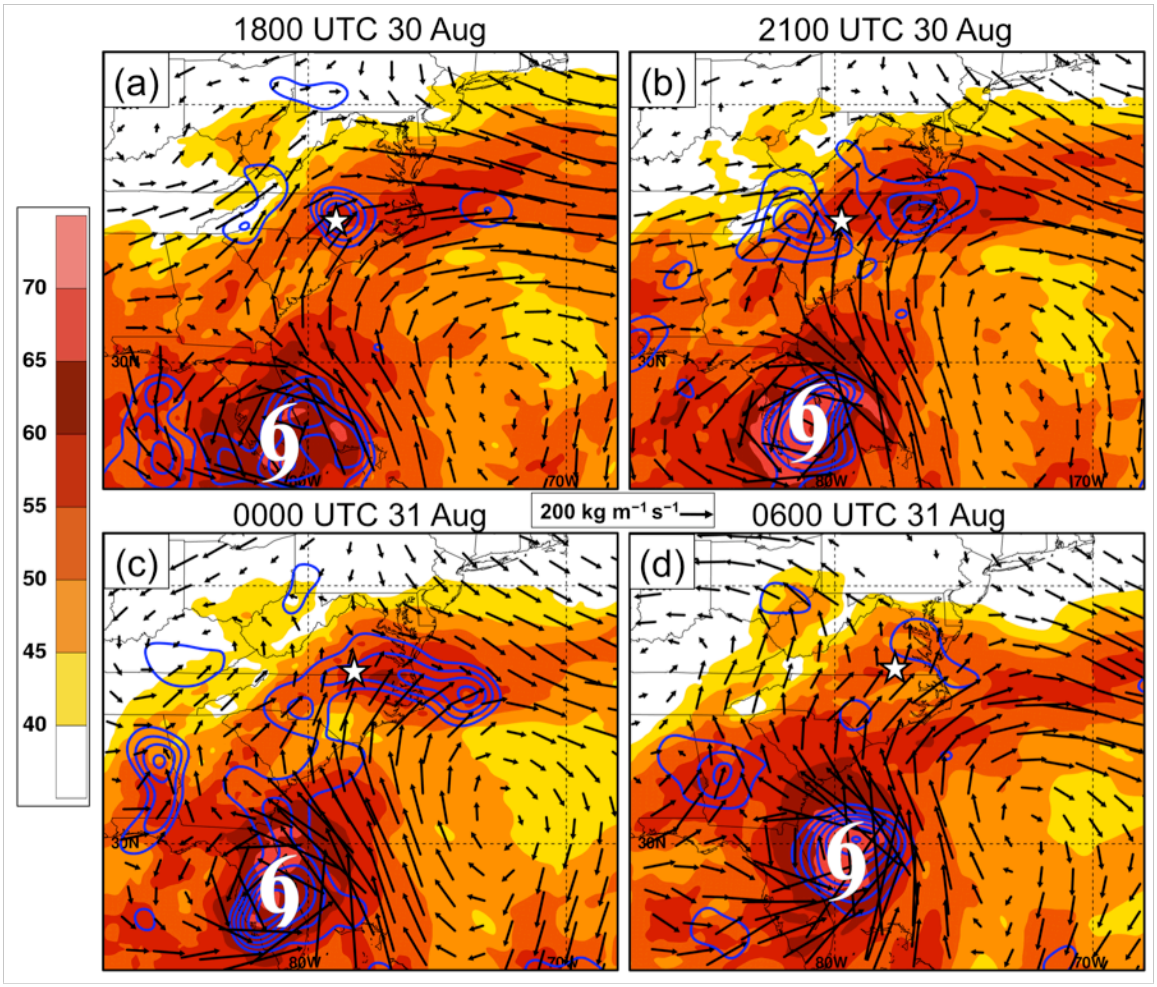


Figure 5.17: Total PW (shaded in mm according to the color bar) and 1000–100-hPa VIMF vectors (kg $m^{-1}$ $s^{-1}$; reference vector in the center) and VIMF convergence (contoured in blue every $5 \times 10^{-4}$ kg $m^{-2}$ $s^{-1}$ starting at $-5 \times 10^{-4}$ kg $m^{-2}$ $s^{-1}$) generated from the 20-km RUC analyses at (a) 1800 UTC 30 August, (b) 2100 UTC 30 August, (c) 0000 UTC 31 August, and (d) 0600 UTC 31 August 2006. The centroid of the PRE is marked by the white star, and the TC location is denoted by the tropical storm symbol.

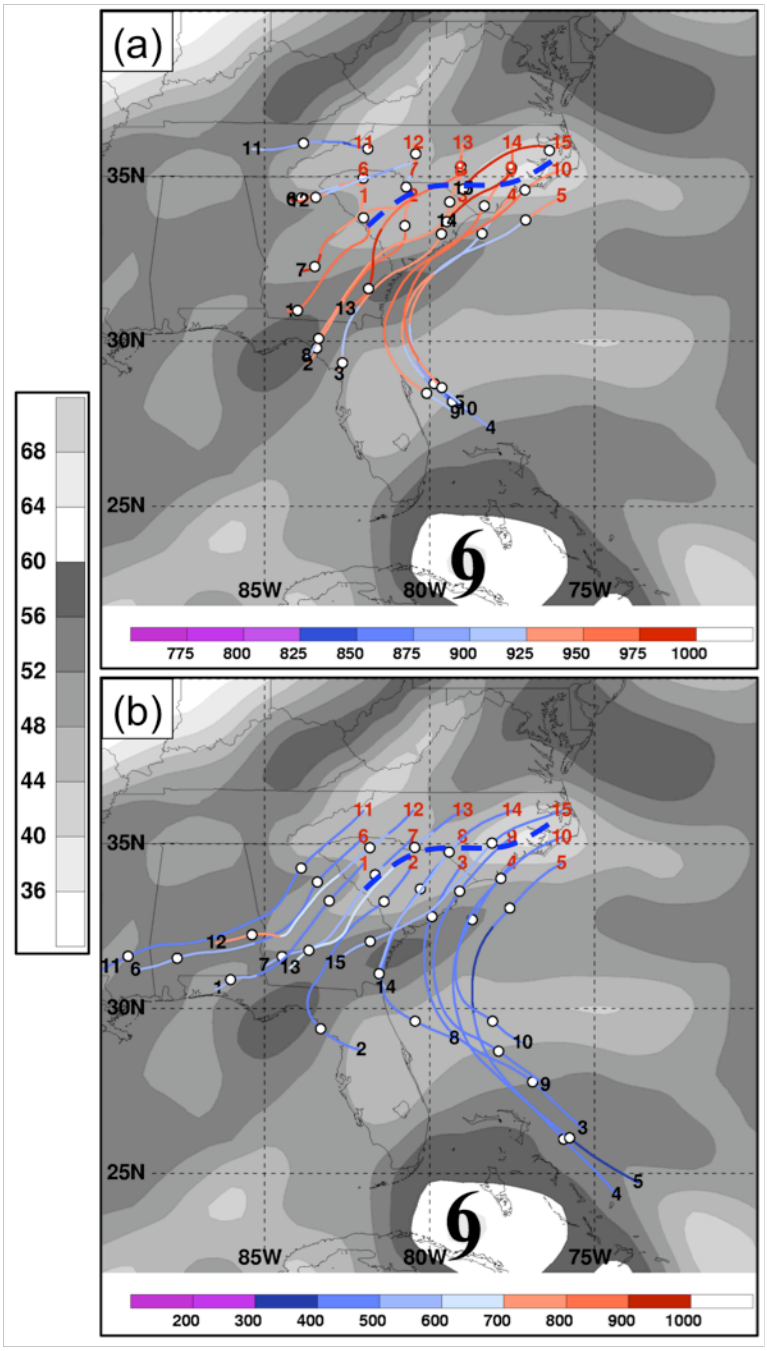


Figure 5.18: Two sets of fifteen 36-h backward kinematic air parcel trajectories ending within the PRE region at (a) 925 hPa and (b) 400 hPa at 0000 UTC 31 August 2006 overlaid on the NCEP 1° GFS total PW analysis at 1200 UTC 29 August 2006 (shaded in mm according to the color bar on the left). The air parcel pressure values (hPa) are shaded according to the color bar at the bottom of each panel. The red (black) numbers denote ending (beginning) point of each trajectory. The position of the surface thermal boundary associated with the PRE cold pool at 0000 UTC 31 August is indicated by the dashed blue line. The position of TC Ernesto at 1200 UTC 29 August 2006 is indicated by the tropical storm symbol.

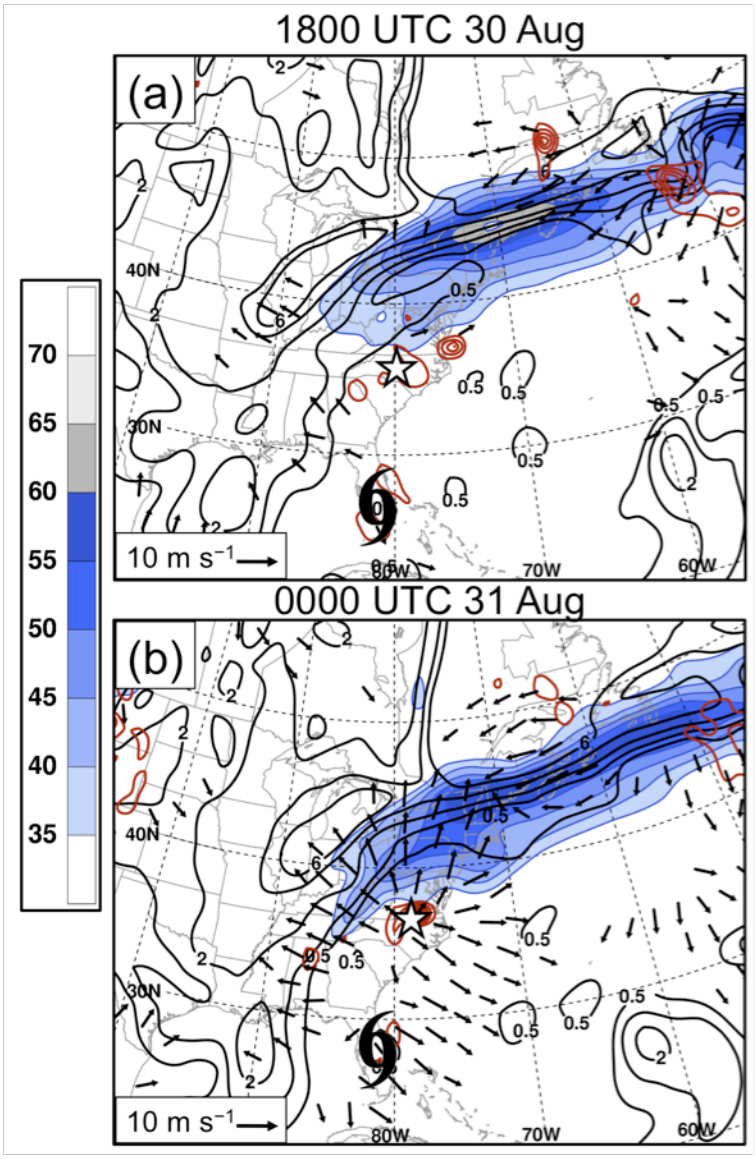


Figure 5.19: As in Fig. 5.10, except for (a) 1800 UTC 30 August and (b) 0000 UTC 31 August 2006.

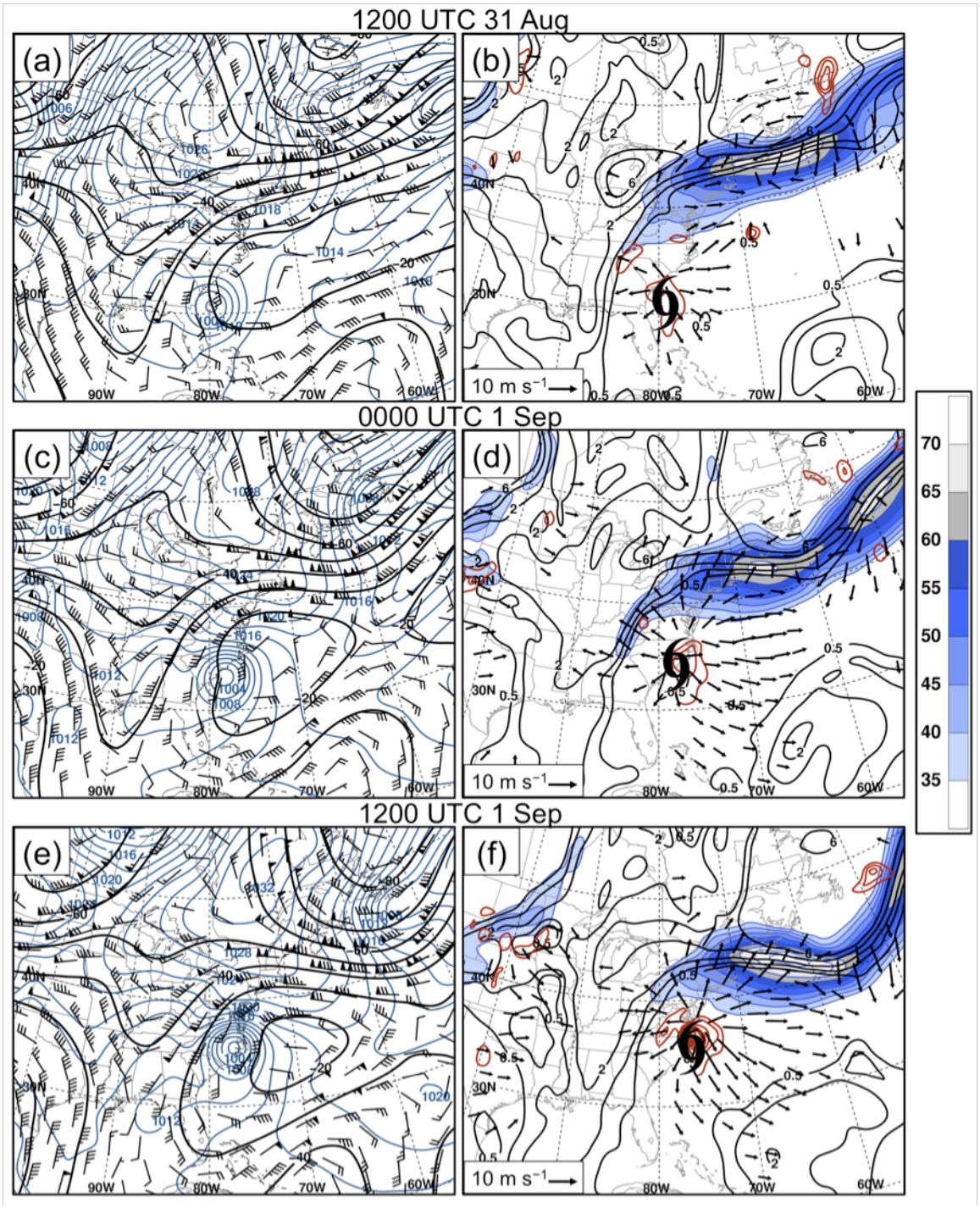


Figure 5.20: Panels on the left show 200-hPa streamfunction (contoured in black every 10 x $10^6$ $m^2$ $s^{-1}$), nondivergent winds (barbs in m $s^{-1}$ according to the convention in Fig. 5.2), and sea level pressure (contoured in blue every 2 hPa) generated from the NCEP 1° GFS analyses at (a) 1200 UTC 31 August, (c) 0000 UTC 1 September, and (e) 1200 UTC 1 September 2006. Panels on the right are the same as in Fig. 5.10, except for (b) 1200 UTC 31 August, (d) 0000 UTC 1 September, and (f) 1200 UTC 1 September 2006.

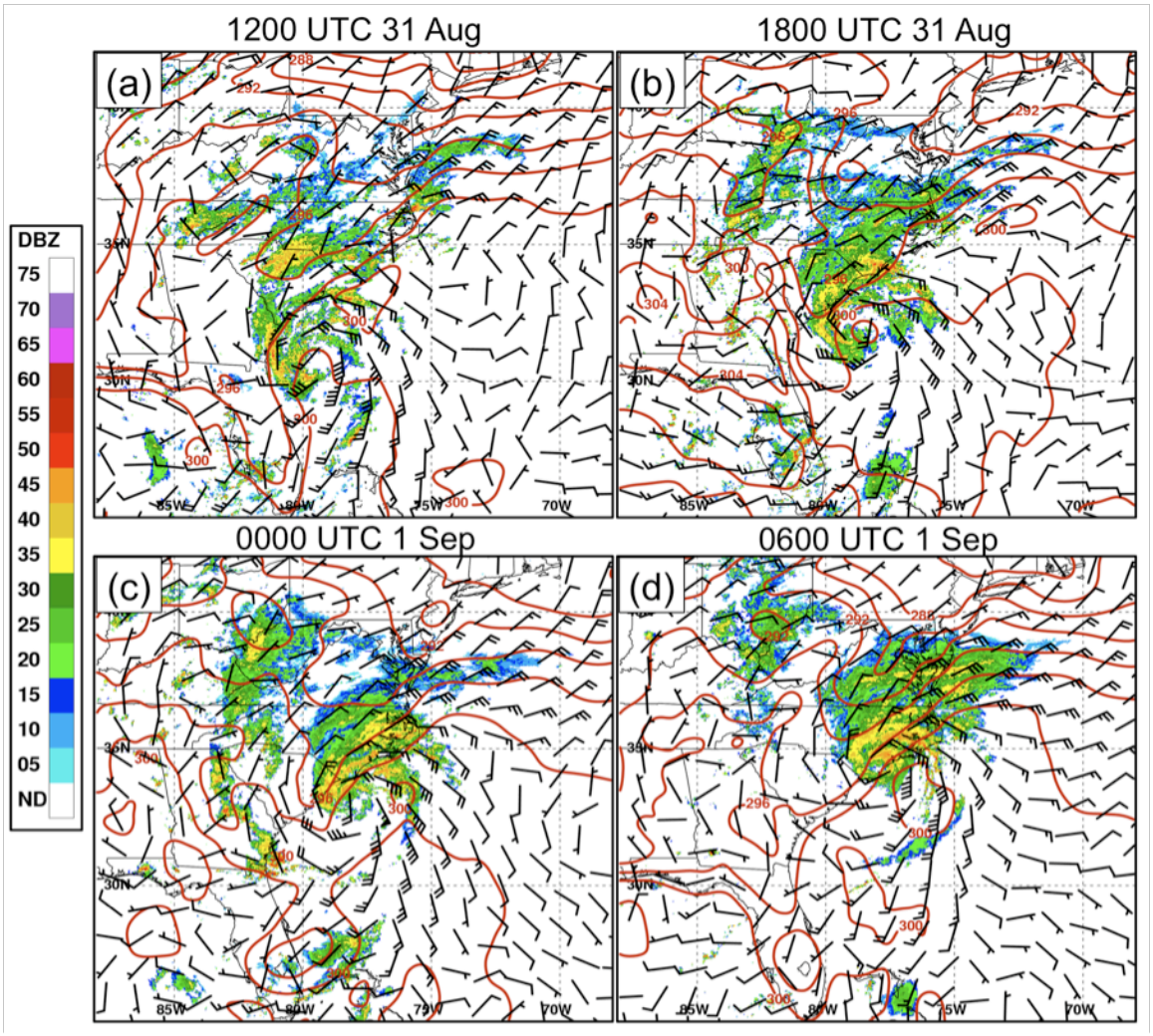


Figure 5.21: As in Fig. 5.14, except for (a) 1200 UTC 31 August, (b) 1800 UTC 31 August, (c) 0000 UTC 1 September, and (d) 0600 UTC 1 September 2006.

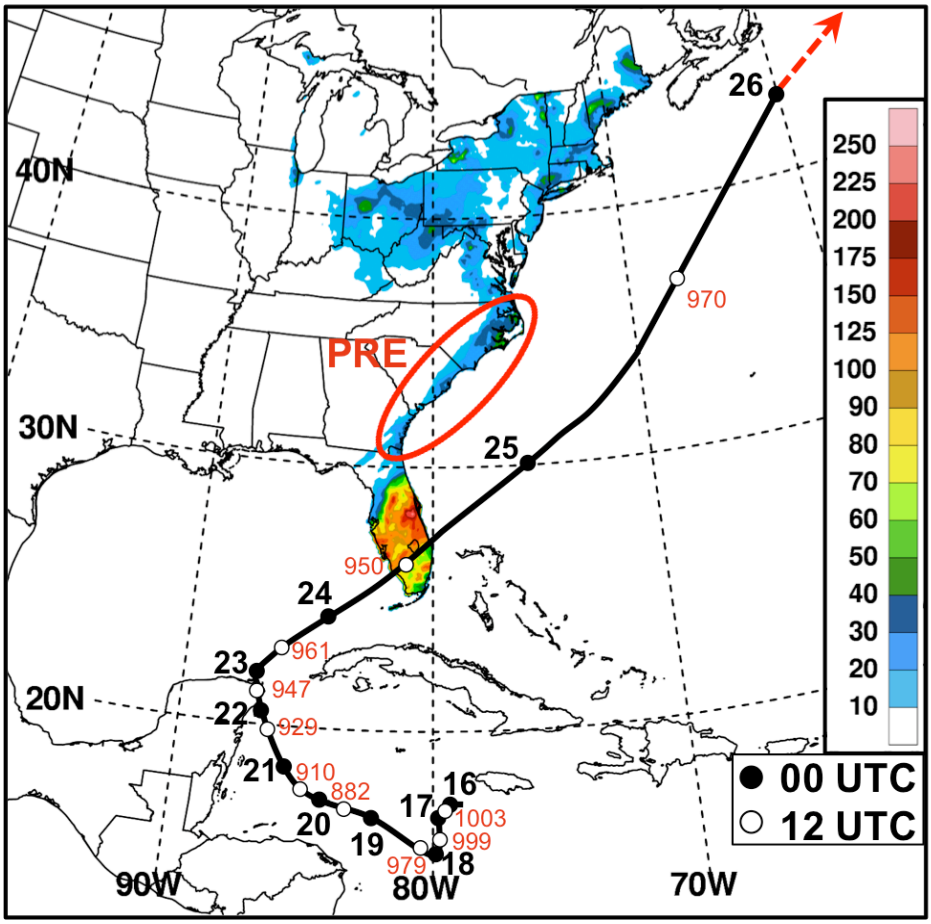


Figure 5.22: The NHC Best Track positions for TC Wilma during 16–26 October 2005 overlaid on the NPVU QPE analysis (shaded in mm according to the color bar) for 1200 UTC 23–1200 UTC 25 October 2005. The filled (unfilled) circles denote the 0000 UTC (1200 UTC) TC positions. The red numbers indicate the 1200 UTC central sea level pressure values (hPa) for TC Wilma. The red dashed line indicates the time and location at which TC Wilma was classified as extratropical.

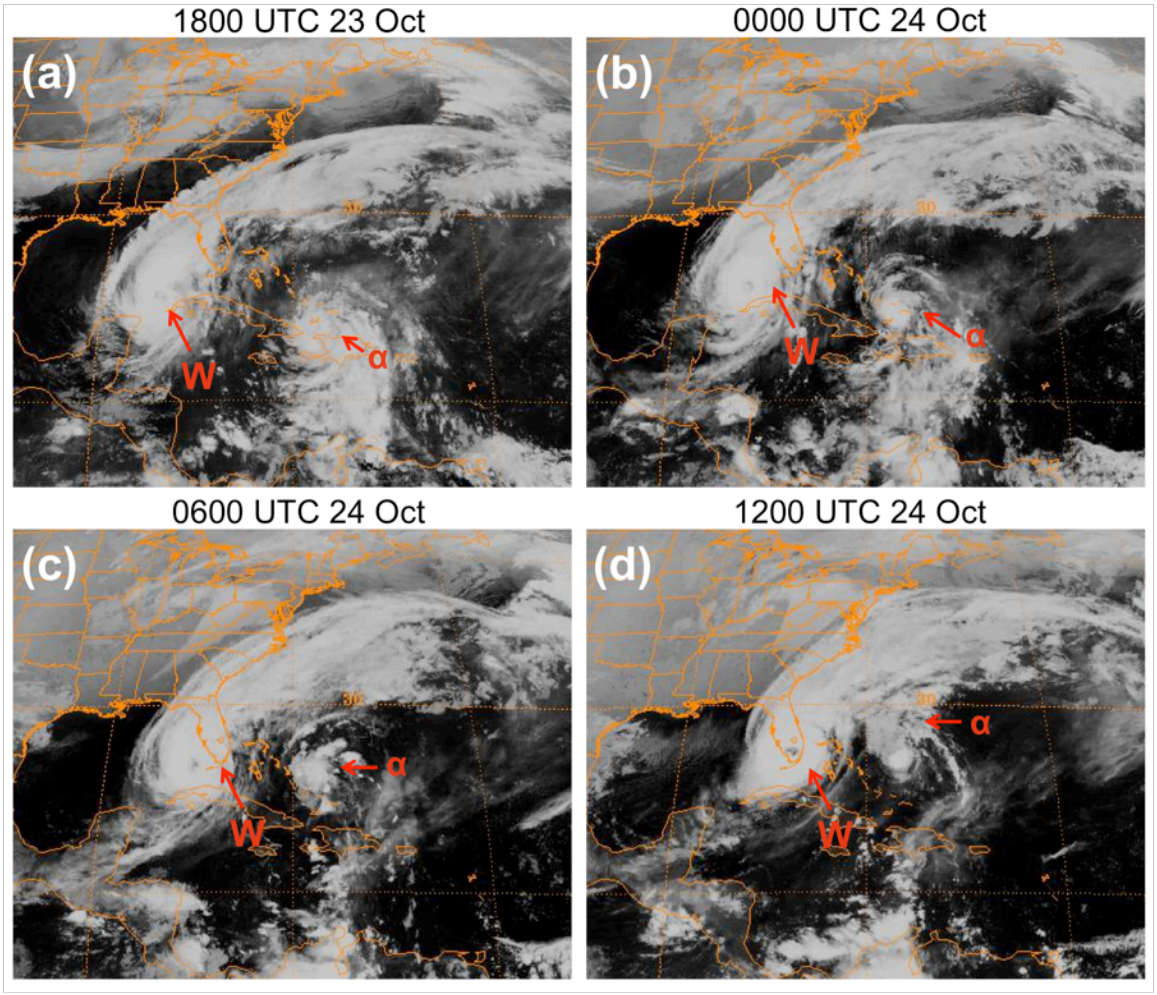


Figure 5.23: *GOES-12* IR (~11 $\mu$m) satellite imagery at (a) 1800 UTC 23 October, (b) 0000 UTC 24 October, (c) 0600 UTC 24 October, and (d) 1200 UTC 24 October 2005. The "W" and the "α" symbols indicate the positions of TC Wilma and TS Alpha, respectively. [Images courtesy of the National Climatic Data Center (NCDC) GIBBS web site at http:// www.ncdc.noaa.gov/gibbs/].

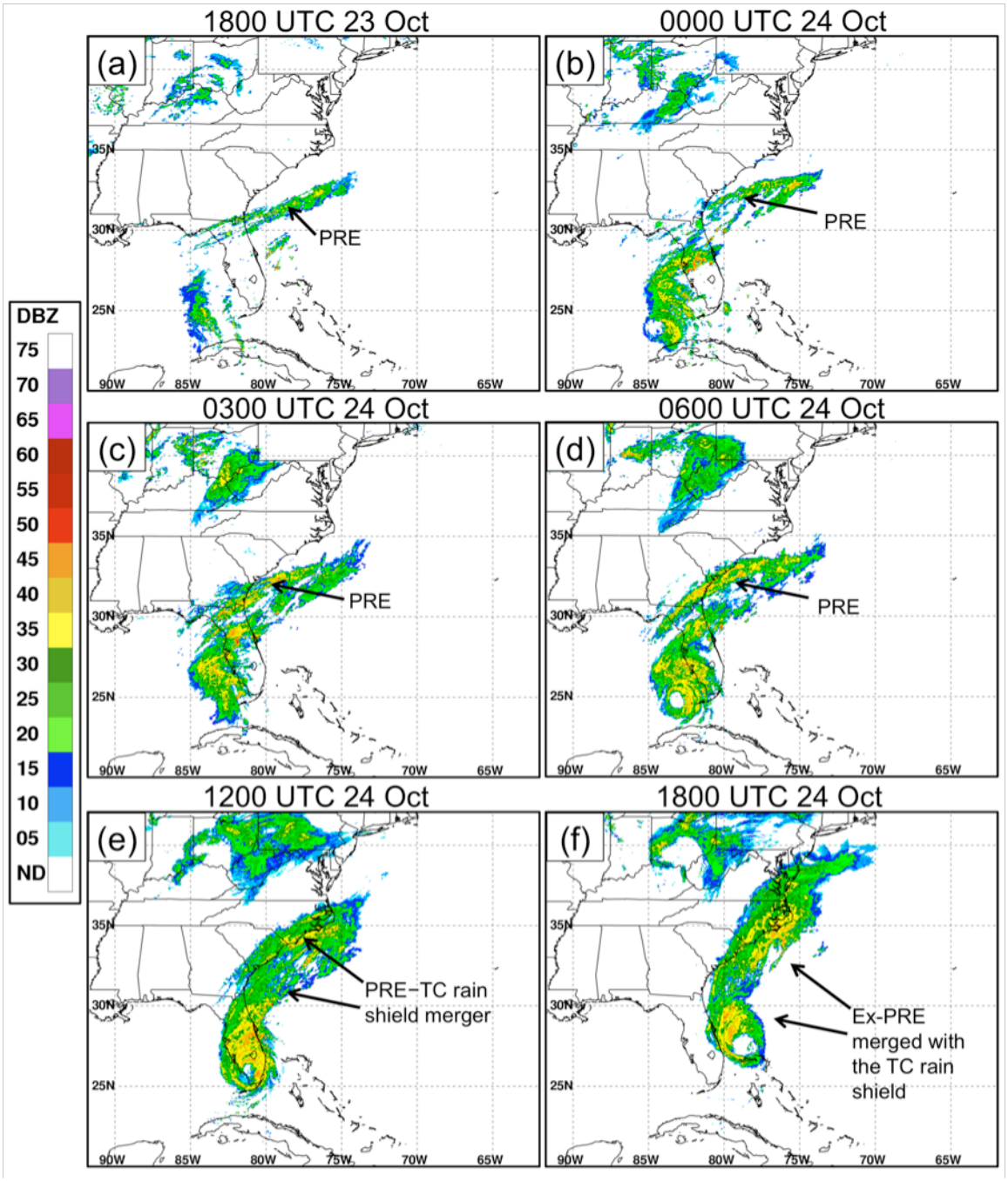


Figure 5.24: WSI NOWrad radar reflectivity mosaics (shaded in dBZ according to the color bar) at (a) 1800 UTC 23 October, (b) 0000 UTC 24 October, (c) 0300 UTC 24 October, (d) 0600 UTC 24 October, (e) 1200 UTC 24 October, and (f) 1800 UTC 24 October 2005.

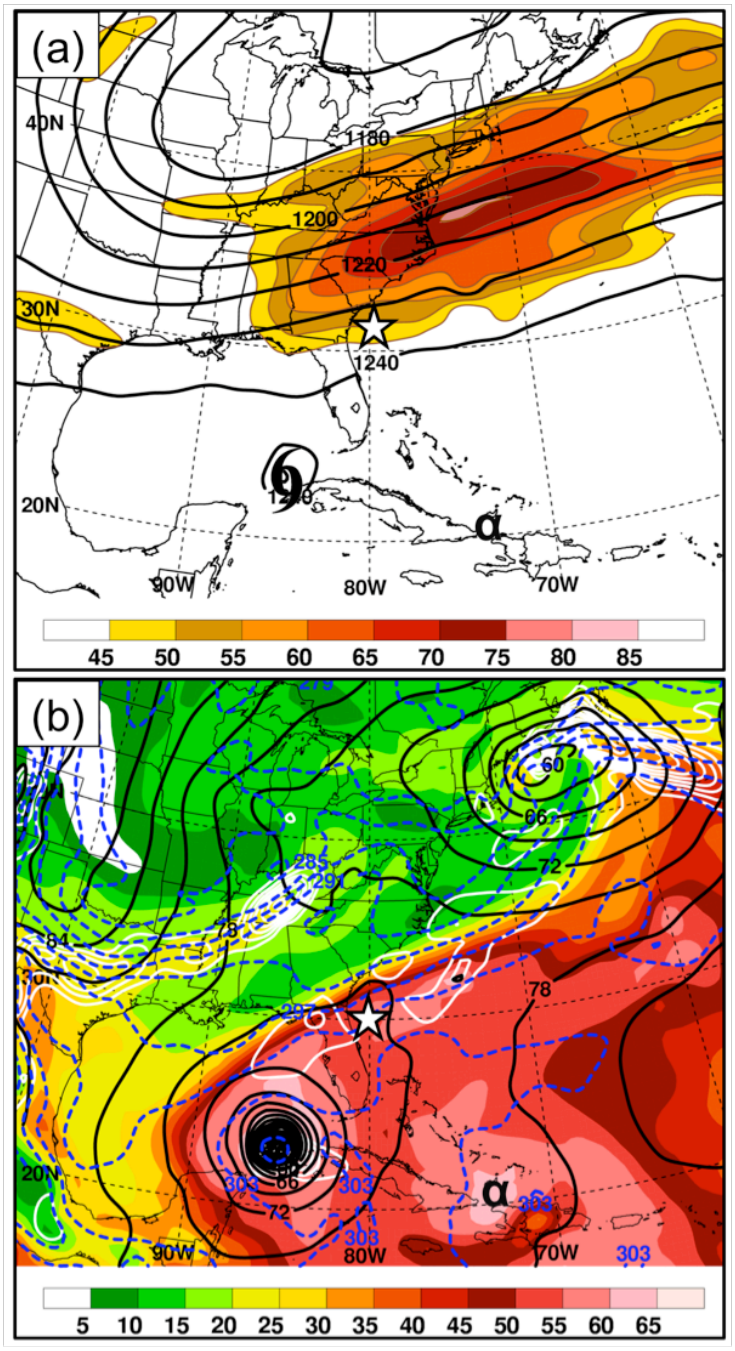


Figure 5.25: As in Fig. 5.3, except for 1800 UTC 23 October 2005, and the position of TS Alpha is indicated by the "α" symbol.

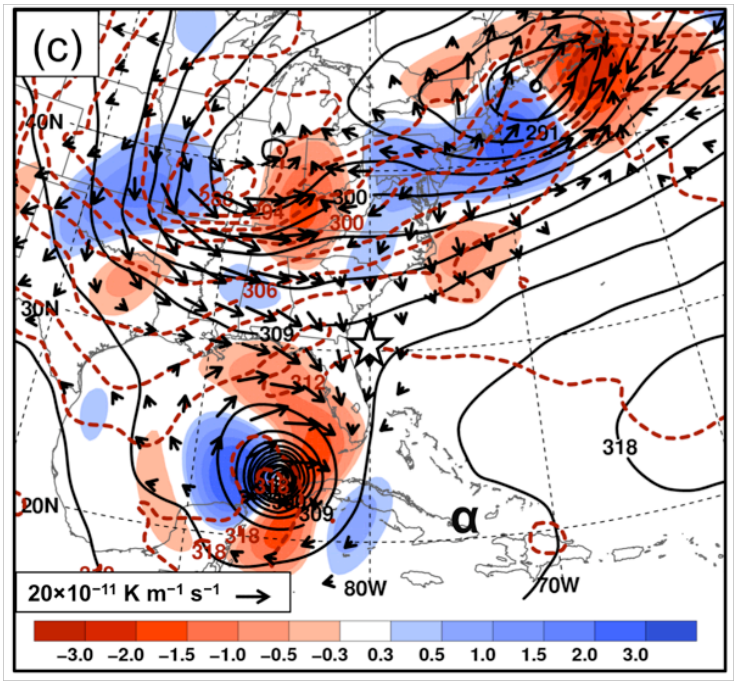
(c)
40N
30N
20N
291
300
306
309
312
318
80W
70W
20×10⁻¹¹ K m⁻¹ s⁻¹
−3.0 −2.0 −1.5 −1.0 −0.5 −0.3 0.3 0.5 1.0 1.5 2.0 3.0

*FIG. 5.25 (cont.)*

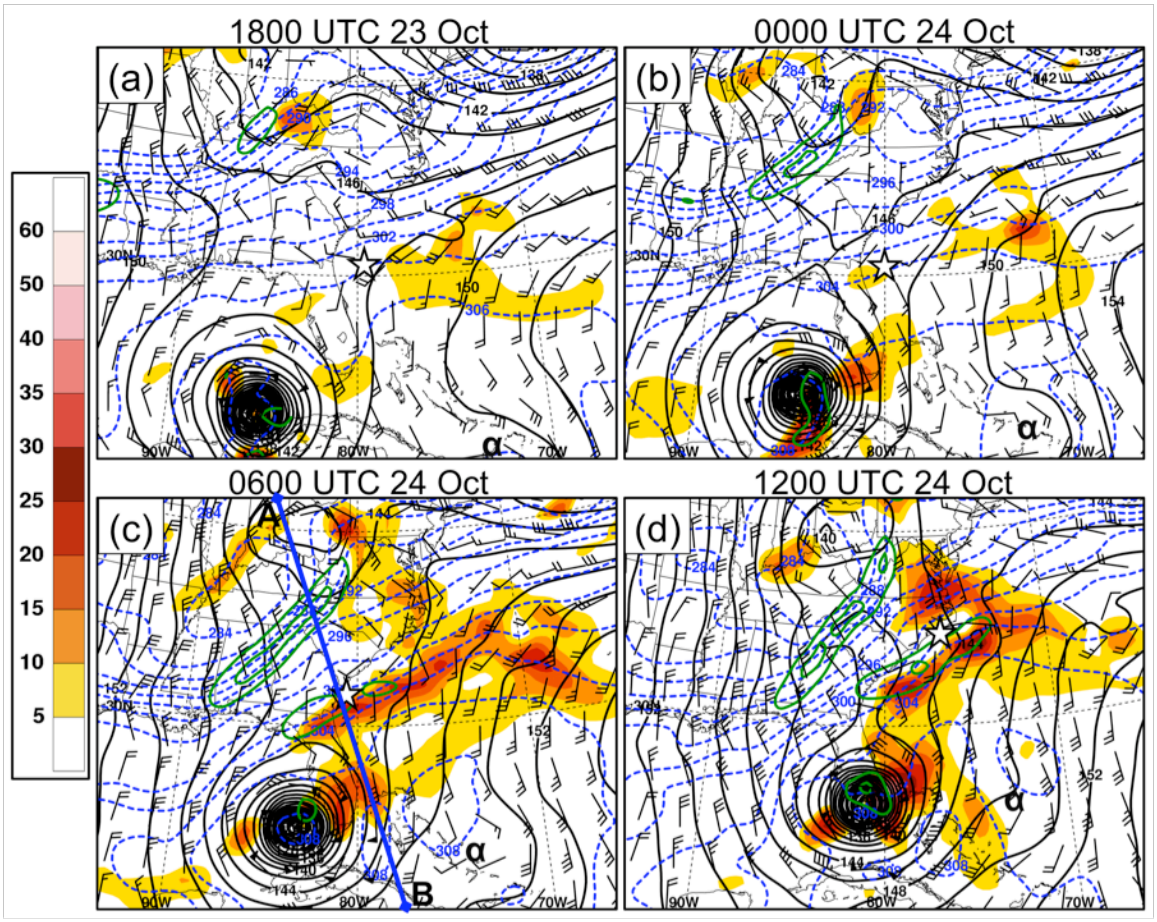


Figure 5.26: 850-hPa geopotential height (contoured in black every 2 dam), potential temperature (contoured in blue every 2 K), Petterssen frontogenesis [contoured in green every 1 K (100 km)$^{-1}$ (3 h)$^{-1}$ starting at 1 K (100 km)$^{-1}$ (3 h)$^{-1}$], and positive potential temperature advection (shaded in $10^{-5}$ K s$^{-1}$ according to the color bar) generated from the NCEP 1° GFS analyses at (a) 1800 UTC 23 October, (b) 0000 UTC 24 October, (c) 0600 UTC 24 October, and (d) 1200 UTC 24 October 2005. Cross section A–B is indicated in panel (c).

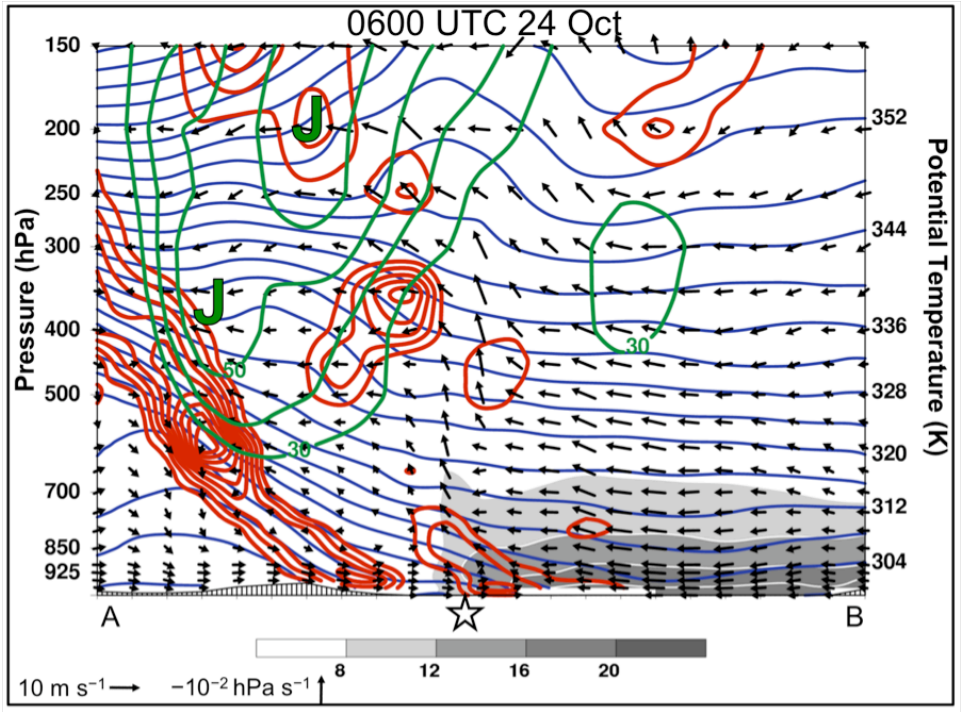


Figure 5.27: As in Fig. 5.16, except generated from the NCEP 1° GFS analysis at 0600 UTC 24 October 2005. The star denotes the position of the PRE. The cross section location is indicated in Fig. 5.26c.

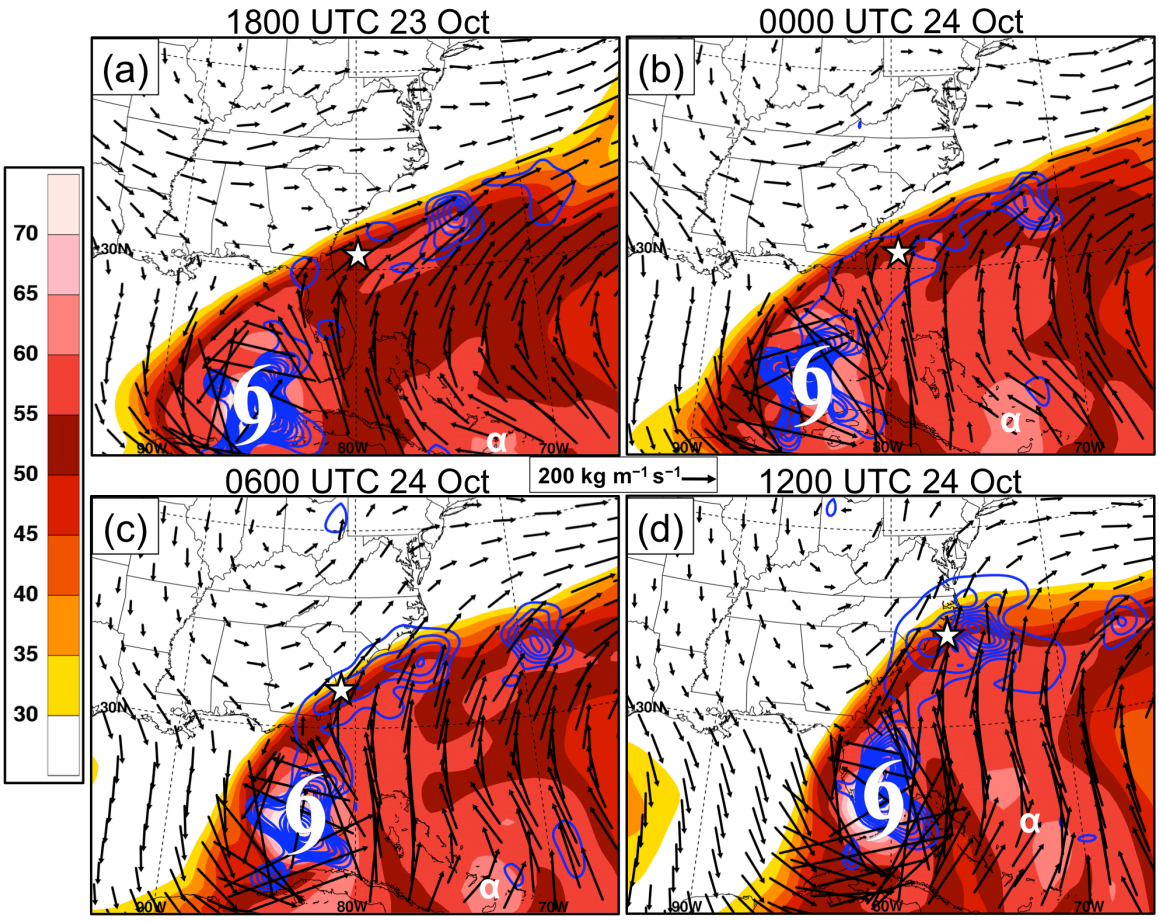


Figure 5.28: As in Fig. 5.17, except generated from the NCEP 1° GFS analyses at (a) 1800 UTC 23 October, (b) 0000 UTC 24 October, (c) 0600 UTC 24 October, and (d) 1200 UTC 24 October 2005.

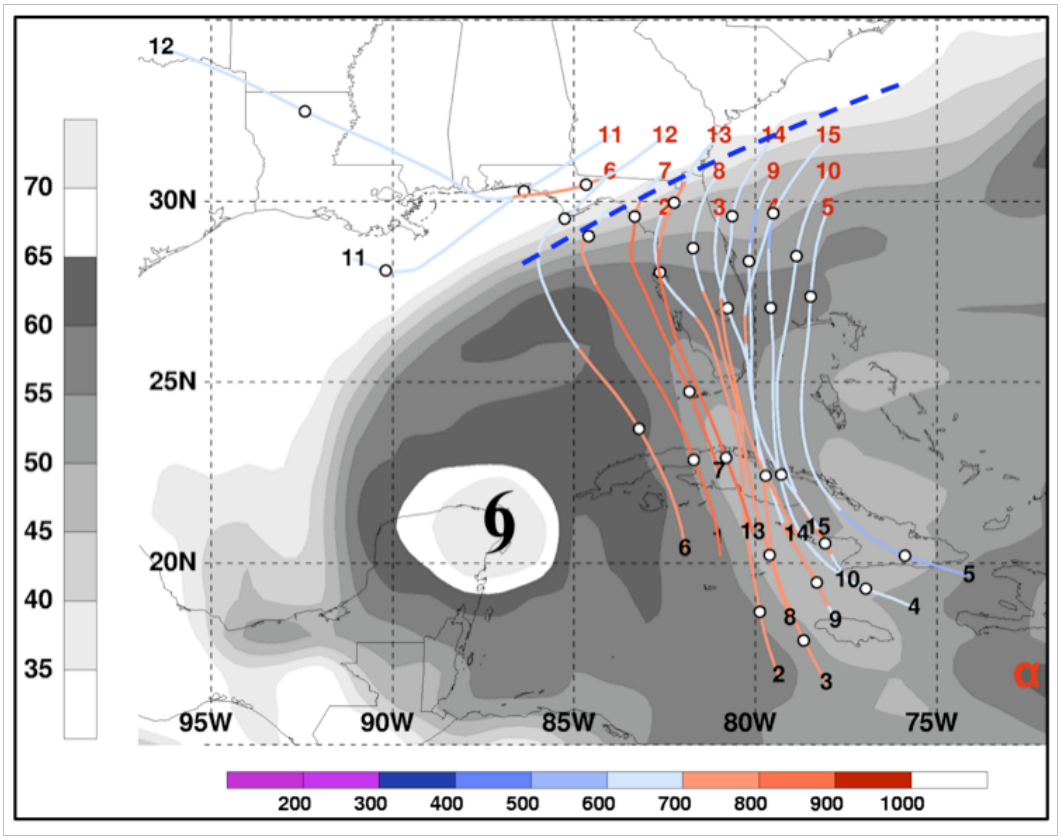


Figure 5.29: As in Fig. 5.18, except all trajectories end at 600 hPa at 0600 UTC 24 October 2005, and the PW analysis at 1800 UTC 22 October is shaded. The dashed blue line denotes the axis of maximum radar reflectivity values associated with the PRE at 0600 UTC 24 October. The red "α" symbol denotes the position of TS Alpha at 1800 UTC 22 October.

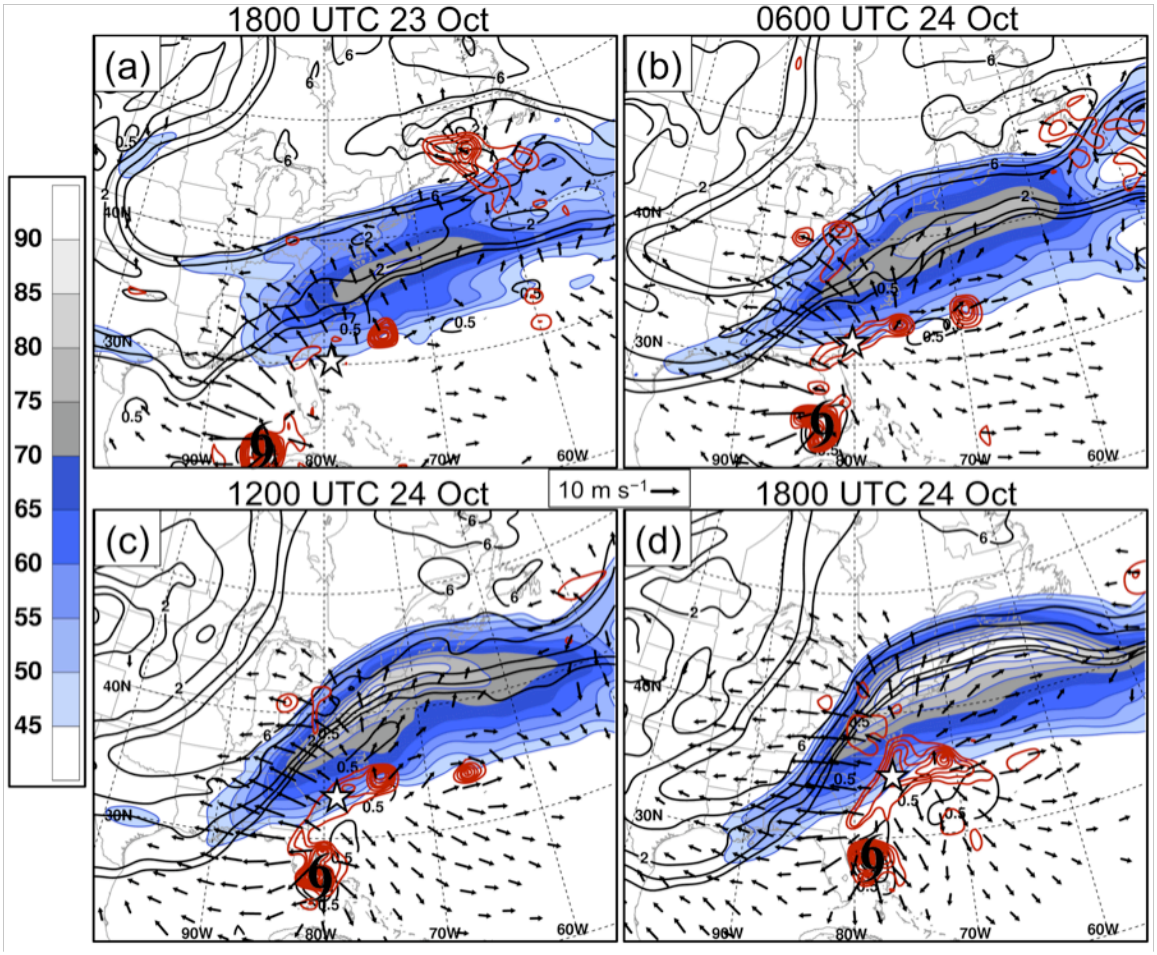


Figure 5.30: As in Fig. 5.10, except for (a) 1800 UTC 23 October, (b) 0600 UTC 24 October, (c) 1200 UTC 24 October, and (d) 1800 UTC 24 October 2005.

## 6. Summary and Discussion

### 6.1 Climatology of PREs during 1988–2008

A total of 56 PREs were identified in association with 38 North Atlantic basin TCs during 1988–2008. Of the 38 TCs, 12 were associated with more than one PRE. Of the 56 PREs identified, 26 (46%) were SJ category PREs, 16 (29%) were DC category PREs, 8 (14%) were JR category PREs, and 6 (11%) were unclassifiable. In accordance with previous studies (C07; GBS10), PREs developed most frequently in August and September. The monthly frequency distributions of SJ category PREs and DC category PREs were slightly skewed toward the late (August–October) and early (June–August) season, respectively, whereas that of the JR category exhibited no apparent skewness. The preferential occurrence of SJ category PREs in the latter part of the season is likely a reflection of the strong baroclinicity that often characterizes their environments. By contrast, DC category PREs tended to occur in environments characterized by weak baroclinicity.

PREs were observed to develop throughout the continental U.S. east of the Rocky Mountains ahead of recurving TCs that made landfall either along the Gulf of Mexico coastline or along the eastern U.S. coastline. Each PRE category exhibited a geographical preference with regard to the PRE development locations and to the parent TC tracks. JR category PREs all developed in the Midwest U.S. ahead of TCs making landfall along the western and central Gulf of Mexico coastline. With some exceptions, SJ category PREs tended to develop throughout the eastern U.S. ahead of sharply recurving TCs that typically tracked along the eastern U.S. coast. DC category PREs

tended to develop over the southeastern U.S. ahead of TCs that made landfall along the central and eastern Gulf of Mexico coastline.

Consistent with the findings of C07 and GBS10, PREs occurred most often to the left of the total observed parent TC track. This finding likely relates to the fact that PREs frequently developed in association with dynamical forcing for ascent ahead of an upper-level trough situated upstream and poleward of the TC. Atallah et al. (2007) showed that the precipitation distribution directly associated with a TC typically shifts to the left of the TC track in response to the approach of a strong upstream upper-level trough. For PREs occurring to the left of the TC track, the parent TCs typically acquired a strong eastward component of motion as they moved poleward and encountered an upstream trough. Of all PREs, those in the JR and SJ categories most frequently occurred to the left of the TC track. For the DC category, PREs frequently occurred either along or to the right of the TC track and the primary upper-level trough was always positioned downstream and poleward of the TC. In association with the position of the primary trough, DC category PREs typically formed within a region of dynamical forcing for ascent located downstream and poleward of the TC. In the absence of both a strong upstream trough and strong westerly/southwesterly steering flow, the parent TCs were often observed to translate poleward, with only a weak eastward component of motion, frequently placing the PRE region either directly along or to the right of the TC track.

The median values for longevity and separation distance for all PREs, consistent with the results of C07 and GBS10, were 16 h and 950 km, respectively, while the median maximum rainfall value for all PREs was 90 mm. There were, however, considerable differences in these statistical quantities among the three PRE categories.

The JR category was generally characterized by the greatest longevity (median value of 24 h), the greatest separation distances (median value of 1100 km), and the greatest maximum rainfall totals (median value of 180 mm). DC category PREs tended to be the shortest lived (median longevity of 13.5 h), whereas SJ category PREs tended to produce the lowest maximum rainfall totals (median value of 80 mm). In association with their tendency to occur during the summer months (June–August), DC category PREs generally occurred in environments more conducive to convection than SJ category PREs and were thus typically characterized by higher rainfall rates and higher maximum rainfall totals than SJ category PREs. By contrast, SJ category PREs tended to develop in the later part of the season (August–October) and generally had fewer convective elements than either the JR category or the DC category, often manifested as bands of heavy stratiform precipitation. The tendency of JR category PREs to produce the greatest maximum rainfall totals is related to the fact that they were frequently manifested as long-lived MCSs resembling the "training line/adjoining stratiform" (TL/AS) extreme-rain-producing MCS archetype documented by Schumacher and Johnson (2005). This mesoscale organizational mode of JR PREs allowed for persistent convective and stratiform rainfall over a given location, often resulting in rainfall totals > 150 mm. Notably, all JR PREs occurred in the central U.S., the region where TL/AS MCSs occur most frequently (Schumacher and Johnson 2006).

## 6.2 PRE-relative composite analysis

The PRE-relative composites presented for each of the three PRE categories in this study illustrate the common environmental properties and dynamical processes

associated with PREs. In accordance with previous studies on PREs (C07; GBS10), the composites indicate that PREs tend to develop in association with: 1) forcing for ascent within the equatorward entrance region of an upper-level jet streak, 2) forcing for ascent associated with low-level warm-air advection and low-level frontogenesis along a low-level baroclinic zone, and 3) poleward transport of deep moisture from the vicinity of a TC. The composite analysis for each of the three PRE categories demonstrates a distinct synoptic-scale configuration in which these three key elements can contribute to the development of a PRE ahead of a landfalling (or near-landfalling) TC.

For the JR category, the TC is embedded within an upper-level ridge, well equatorward (~1100 km) from a region of forcing for ascent associated with the equatorward entrance region of an anticyclonically curved upper-level jet streak and a quasi-stationary low-level baroclinic zone. The PRE develops as moisture is transported well poleward from the TC on the eastern flank of a low-level ridge into this region of forcing for ascent. The large separation distance between the TC and the PRE for the JR category suggests that the dynamical influence of the TC on PRE development is likely small. The low-level cyclonic circulation associated with the TC is likely too far removed from the low-level baroclinic zone to directly influence the development of frontogenesis and warm-air advection within the PRE region. Similarly, the upper-level diabatically driven outflow associated with the TC does not extend far enough poleward to directly affect the evolution of the upper-level jet streak. It is likely that the environments of JR category PREs are often preconditioned for heavy rainfall and that the role of the TC in producing the PRE is mainly *indirect*, serving primarily as a source of deep moisture. In the JR composites, this hypothesis that the environment is

preconditioned for heavy rainfall is supported by the presence of deep moisture, low-level frontogenesis, low-level warm-air advection, and upper-level divergence within the PRE region 12 h prior to the time of PRE initiation (Figs. 4.1a,b). It is not until the TC moisture is transported into the PRE region that the most significant heavy rainfall commences. GBS10 suggested for the PRE ahead of TC Erin (2007) that the presence of deep moisture from the TC likely turned a significant rain event into an unprecedented rain event.

For the SJ category, dynamical forcing for PRE development arises from the interaction between the TC and an upstream midlatitude baroclinic system. At low levels, the outer circulation of the TC interacts with an approaching baroclinic zone, establishing focused warm-air advection and frontogenesis. Meanwhile, the upper-level diabatically driven low-PV outflow associated with the TC leads to ridge amplification ahead of an approaching upper-level trough, strengthening a southwesterly jet streak poleward of the PRE region. These lower- and upper-level TC–midlatitude interactions contribute to deep ascent poleward of the TC, which, in the presence of a stream of deep moisture from the TC, results in PRE development. Various studies have documented similar dynamical interactions between TC outflow and an upper-level trough (e.g., Klein et al. 2002; Atallah and Bosart 2003; Agustí-Panareda et al. 2004) and between a TC and a low-level baroclinic zone (e.g., Klein et al. 2000; Harr and Elsberry 2000; Atallah and Bosart 2003; Colle 2003) for the process of ET. For the SJ category, the inferred dynamical importance of the TC in establishing lift within the PRE region indicates that the TC plays a *direct* role in the development of the PRE. In contrast to the JR category,

it is likely that heavy rainfall would not otherwise occur in the absence of the dynamical influence of the TC.

DC category PREs develop as the circulation of a poleward-moving TC approaches a weak zonally oriented low-level baroclinic zone that trails behind a downstream midlatitude baroclinic system. An upper-level jet streak is situated in region of confluence downstream of the TC associated with an eastward-moving downstream trough positioned poleward of a diabatically amplified ridge extending poleward and eastward from the TC. As southerly low-level flow on the eastern flank of the TC circulation impinges upon the weak low-level baroclinic zone, frontogenesis and warm-air advection are established beneath the equatorward entrance region of the jet streak, contributing to the development of deep ascent poleward and eastward of the TC. PRE development is favored as deep moisture streams poleward on the eastern flank of the TC circulation towards this region of ascent. As in the SJ configuration, the role of the TC in PRE development in the DC category is typically *direct*, wherein the dynamical interactions between the TC and the midlatitude flow aid in establishing forcing for ascent poleward of the TC.

## 6.3 Case studies

### *6.3.1 PRE ahead of TC Rita (2005)*

The PRE ahead of TC Rita (2005) highlights the close similarity between the JR pattern and the classic "frontal" pattern for flash-flood-producing MCSs originally documented by Maddox et al. (1979). The PRE developed and rapidly became organized during 25 September 2005 over southern Minnesota and northern Iowa as a nocturnally

intensifying low-level jet impinged upon a quasi-stationary low-level baroclinic zone situated along the Minnesota–Iowa border. As previous studies (e.g., Maddox et al. 1979; Trier and Parsons 1993; Augustine and Caracena 1994; Junker et al. 1999; Moore et al. 2003) have shown for heavy-rain-producing MCSs, focused mesoscale ascent associated with warm-air advection and frontogenesis maximized at the intersection of the low-level jet with the baroclinic zone provided support for the continuous development of heavy convective rainfall over southern Minnesota and northern Iowa. In addition to supporting focused mesoscale ascent within the PRE region, the low-level jet facilitated the strong poleward transport of low-level moisture from the northeastern flank of the TC Rita circulation into the PRE region. As was suggested above regarding the JR category composites, the role of TC Rita in the development of the PRE was primarily indirect, acting through a low-level jet to provide moisture to a region of focused ascent that was separated from the dynamical influences (i.e., cyclonic low-level circulation, upper-level outflow) of the TC. The importance of a strong low-level jet for transporting TC moisture and for establishing focused ascent along a quasi-stationary low-level baroclinic zone was also shown by GBS10 for the high-impact PRE ahead of TC Erin (2007).

The TC Rita PRE was manifested as a linear MCS resembling the TL/AS extreme-rain-producing MCS archetype documented by Schumacher and Johnson (2005). This mesoscale organizational mode was associated with the repeated passage of convective and stratiform precipitation over southern Minnesota and northern Iowa. The PRE remained quasi-stationary throughout much of its lifespan due to the continuous upshear development of convective and stratiform precipitation within a region of strong

low-level moisture flux convergence (e.g., Glass et al. 1995; Junker et al. 1999). Persistent heavy rainfall during 25 September 2005 resulted in extreme rainfall totals (~200 mm) and flash flooding throughout southern Minnesota and northern Iowa. This PRE, along with the PREs ahead of TC Erin (2007; GBS10) and TC Ike (2008), was one of three high-impact, flash-flood-producing JR category PREs that affected the upper Midwest during only a 4-year period (2005–2008).

As the TC Rita PRE developed and became organized, the upper-level diabatically driven low-PV outflow associated with the coherent region of heavy precipitation contributed to the development of a strong, concentrated 200-hPa jet streak directly poleward of the PRE region. Upper-level jet streak development (or enhancement) has been documented in previous studies to occur in response to upper-level ridge amplification associated with the diabatically driven outflow from a midlatitude MCS (e.g., Maddox et al. 1981; Trier and Sharman 2009). The development of this jet streak in response to diabatic processes was accompanied by the development of deep, vigorous ascent and, accordingly, by the enhancement of precipitation within the PRE region. This enhancement of ascent and precipitation is consistent with the findings of Keyser and Johnson (1984), who showed that the thermally direct circulation within the entrance region of a jet streak can be enhanced in response to diabatic heating associated with an MCS. It is possible that this diabatically enhanced thermally direct circulation associated with the jet streak was coupled with the thermally direct circulation associated with low-level frontogenesis (e.g., Hakim and Keyser 2001), contributing to the deep ascent observed over the PRE region.

*6.3.2 PRE ahead of TC Ernesto (2006)*

The DC category PRE ahead of TC Ernesto (2006) developed on 30 August 2006 over central North Carolina beneath the equatorward entrance region of a 200-hPa jet streak and along a surface thermal boundary associated with a weak region of cold-air damming to the east of the Appalachian Mountains. An evaporationally induced surface cold pool formed in association with the developing PRE, enhancing an antecedent cold pool over North Carolina associated with the region of cold-air damming. As moisture continuously streamed poleward on the eastern flank of the TC Ernesto circulation, the PRE intensified and became organized over North Carolina and Virginia during 30–31 August in association with lifting along a mesoscale region of enhanced baroclinicity on the southeastern flank of this evaporationally enhanced cold pool. Lifting along a mesoscale region of baroclinicity associated with evaporationally enhanced cold-air damming was shown by Bosart and Dean (1991) and Srock and Bosart (2009) to be important for focusing heavy rainfall ahead of TC Agnes (1972) and TC Marco (1990), respectively. Additionally, the process by which convection develops and becomes organized in association with lifting on the periphery of an evaporationally induced cold pool has been frequently documented for heavy-rain-producing MCSs (e.g., Maddox et al. 1979, Chappell 1986; Schumacher and Johnson 2005).

In contrast to the DC category composites, the locus of PRE development was separated from the direct dynamical influences of TC Ernesto. Specifically, the interactions of the low-level cyclonic circulation and the upper-level diabatically driven outflow associated with TC Ernesto with the midlatitude flow were minimal during the lifespan of the PRE. Rather, as in the TC Rita PRE, the role of TC Ernesto in the

development of the PRE was primarily to serve as a source of deep moisture. Although the PRE lasted for less than 12 h, the presence of this deep moisture from TC Ernesto, combined with moderate-to-strong conditional instability, likely favored high precipitation rates and high precipitation efficiencies (e.g., Market et al. 2003), culminating in local rainfall maxima of 50–100 mm throughout North Carolina and Virginia

The impacts of the heavy rainfall associated with the TC Ernesto PRE were augmented by the subsequent passage of the TC Ernesto rain shield between 31 August and 1 September. Upper-level ridge amplification associated with the diabatically driven low-PV outflow from TC Ernesto likely precluded the eastward movement of a weak upstream short-wave trough and reinforced a southerly steering flow over the TC. This southerly steering flow likely caused TC Ernesto to move poleward along the southeastern U.S. coast and to track over North Carolina and Virginia, producing heavy rainfall over soils previously saturated by the PRE. The ability of the outflow associated with TC Ernesto to reconfigure the upper-level flow and to impact the motion of the TC is consistent with the results of Wu and Emanuel (1993), who showed that the upper-level anticyclonic flow induced by TC outflow can impact the steering flow overlying the TC.

As TC Ernesto tracked along the southeastern U.S. coastline and into North Carolina and Virginia, the heavy precipitation directly associated with the TC rain shield was focused along and on the cool side of a surface thermal boundary situated along the coastlines of South Carolina, North Carolina, and Virginia, consistent with the findings of Klein (2007, 66–68). Though requiring further investigation, the mesoscale analysis in

the present study suggests that the evaporationally enhanced cold pool associated with the PRE was instrumental for establishing this coastal surface thermal boundary. It is therefore argued that the PRE itself aided in setting up favorable conditions for heavy precipitation associated with TC Ernesto to be focused over the region previously affected by the PRE.

*6.3.3 PRE ahead of TC Wilma (2005)*

The SJ category PRE that occurred ahead of TC Wilma (2005) illustrates the dynamical linkage that can exist between PRE development and ET. Resembling "step 1" of the transformation stage of ET documented by Klein et al. (2000), the PRE developed and expansion during 23–24 October 2005 as the outer circulation of TC Wilma interacted with a low-level midlatitude baroclinic zone along the southeastern U.S. coastline. As has been documented in various studies of ET (e.g., Klein et al. 2000; Harr and Elsberry 2000; Atallah and Bosart 2003; Colle et al. 2003), frontogenesis and warm-air advection served as a focus for heavy rainfall as southeasterly low-level flow impinged upon the baroclinic zone. The distinction for this case, however, from cases of ET is that the PRE was a separate entity from the TC rain shield. In addition to providing dynamical support for PRE development, the circulation of TC Wilma transported deep moisture into the PRE region, favoring the growth and intensification of the PRE.

The upper-level diabatically driven low-PV outflow associated with the PRE and TC Wilma contributed to upper-level ridge amplificaton and to the strengthening of a 200-hPa jet streak poleward of the PRE region. Upper-level jet streak strengthening in response to the diabatically driven low-PV outflow and ridge amplification associated

with a TC is a common characteristic of ET (e.g., Klein et al. 2002; Atallah and Bosart 2003; Agustí-Panareda et al. 2004). This upper-level jet strengthening, in turn, has been shown to be associated with the enhancement of upper-level divergence and lift within the equatorward entrance region of the jet streak (e.g., Atallah and Bosart 2003). For the Wilma PRE, the strengthening of the jet streak due to diabatic processes was concurrent with the intensification and expansion of ascent and precipitation beneath the equatorward entrance region of the jet streak.

The TC Wilma PRE case demonstrates the possibility that PREs can develop just prior to or in the early stages of ET when the TC circulation first begins to interact with a midlatitude baroclinic zone. The key dynamical processes (i.e., warm-air advection, frontogenesis, jet streak enhancement) associated with the PRE continued as TC Wilma became embedded in the midlatitude baroclinic zone and merged (as depicted in the radar imagery) with the PRE. During this merger, the PRE remained a coherent region of heavy rainfall while becoming a part of the structure of the transitioning TC, eventually constituting an elongated region of heavy rainfall extending poleward from the center of TC Wilma. The ET of TC Floyd (1999; e.g., Atallah and Bosart 2003) was similarly preceded by a PRE. The TC Floyd PRE developed at the onset of the interaction between the TC and a midlatitude baroclinic zone (not shown). As in the TC Wilma PRE case, the PRE was followed by the development of an elongated region of heavy rainfall that extended poleward from the center of TC Floyd in conjunction with the continued interaction between the TC circulation and the baroclinic zone (Atallah and Bosart 2003; Colle 2003).

## 6.4 Conceptual models for use in operational forecasting

The following three subsections will present conceptual models illustrating the synoptic-scale environments for each of the three PRE categories. Each conceptual model depicts the salient lower- and upper-level features that have been documented in this study through the PRE-relative composite analysis and through the three case studies. The objective of these conceptual models is to provide operational forecasters with tools for identifying favorable environments for PRE development as a TC makes (or nearly makes) landfall over the U.S. east of the Rocky Mountains.

### *6.4.1 JR category*

A conceptual model of the synoptic-scale environment associated with JR category PREs is shown in Fig. 6.1. The PRE develops along a quasi-stationary low-level baroclinic zone and beneath the equatorward entrance region of an anticyclonically curved upper-level jet streak situated on the poleward flank of a broad upper-level ridge. A slow-moving, positively tilted upper-level trough is typically situated well upstream of the PRE region. The parent TC is embedded within the broad ridge and is situated well equatorward (~1100 km) of the PRE region. The poleward transport of deep moisture from the TC toward the PRE is afforded by a strong poleward-extending low-level jet on the western flank of a low-level ridge situated to the east of the TC circulation. Ascent within the PRE region develops in association with warm-air advection and frontogenesis at the intersection of the low-level jet with the quasi-stationary low-level baroclinic zone. Persistent heavy rainfall is favored as the poleward-moving stream of moisture from the TC encounters the region of ascent along the low-level baroclinic zone and beneath the

equatorward entrance region of the upper-level jet streak. As heavy rainfall develops within the PRE region, the upper-level diabatically driven low-PV outflow acts to strengthen PV gradients along the axis of the upper-level jet streak, contributing to the intensification of the jet streak and to the enhancement of along-flow wind speed gradients within the jet entrance region. These flow changes associated with the jet streak are typically coincident with the enhancement of ascent and precipitation within the PRE region.

*6.4.2 SJ category*

A conceptual model of the environment of SJ category PREs is shown in Fig. 6.2. SJ category PREs involve the interaction between a poleward-moving TC and an approaching midlatitude trough. The PRE develops within the equatorward entrance region of a southwesterly upper-level jet streak that is situated between the approaching trough and a slow-moving ridge extending poleward and eastward from the TC. The PRE is focused within a region of warm-air advection and frontogenesis established as southeasterly low-level flow within the outer circulation of the TC impinges upon a southwest–northeast oriented low-level baroclinic zone. Deep moisture is continuously transported into the PRE region by this strong southeasterly flow. At upper levels, the diabatically driven outflow associated with both the TC and PRE leads to ridge amplification poleward of the TC and PRE along the axis of the jet streak. This ridge amplification enhances PV and geopotential height gradients ahead of the approaching trough, thereby acting to strengthen the jet streak.

*6.4.3 DC category*

A conceptual model of the environment of DC category PREs is shown in Fig. 6.3. The PRE develops beneath the equatorward entrance region of an upper-level jet streak positioned within a region of upper-level confluent flow associated with a trough-over-ridge pattern situated downstream of the TC. In contrast to the JR and SJ configurations, the primary upper-level trough is situated downstream of the TC, while the upstream upper-level flow is generally weak. Forcing for ascent is provided within the PRE region in association with warm-air advection and frontogenesis as southerly low-level flow on the eastern flank of the TC circulation impinges upon a zonally oriented low-level baroclinic zone that trails behind the downstream trough. Deep moisture is transported into the PRE region by strong southerly flow on the eastern flank of the circulation of the TC. At upper levels, ridge amplification associated with the diabatically driven outflow from the PRE and TC enhances confluent flow on the upstream flank of the jet streak and often acts to backbuild the jet streak. Through this backbuilding process, the entrance region of the jet streak is "anchored" poleward of the PRE location, contributing to the maintenance of strong ascent.

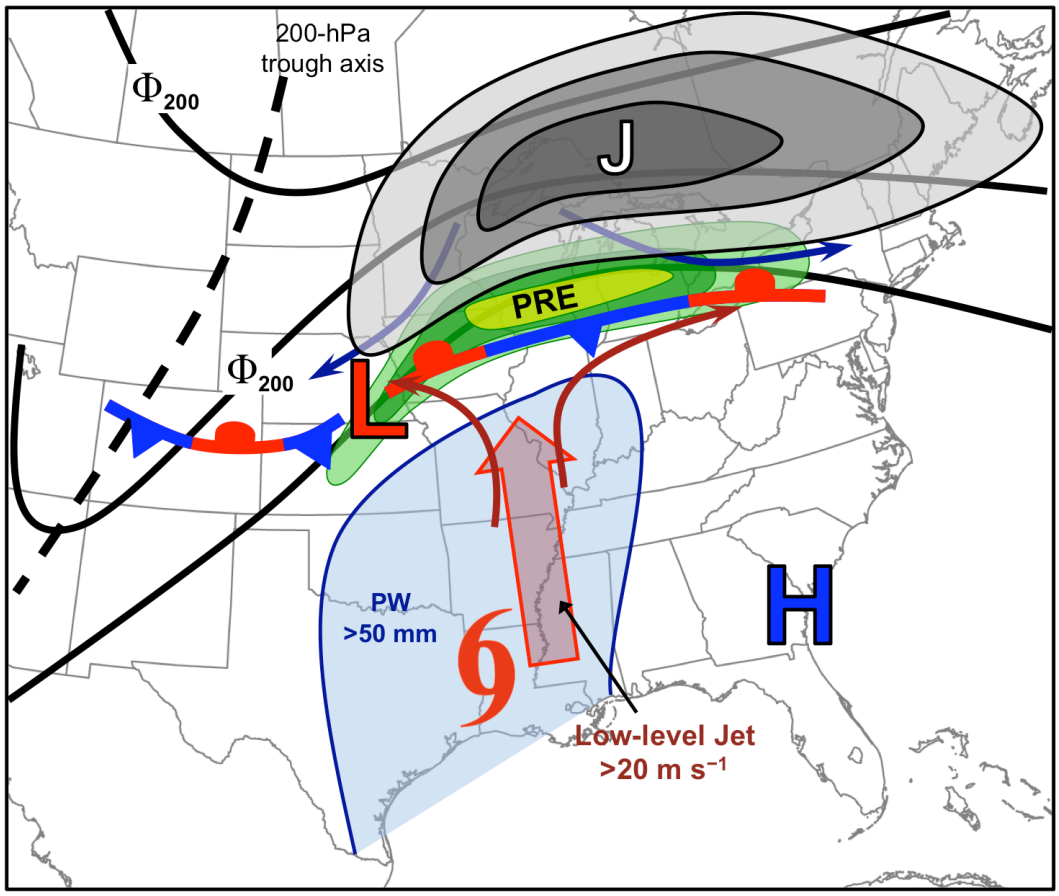


Figure 6.1: Conceptual model of the synoptic-scale environment of JR category PREs showing 200-hPa geopotential height (solid black contours), 200-hPa wind speed (gray shading; "J" symbol marks the location of maximum wind speed), low-level (i.e., 925-hPa) streamlines (red indicates warm advection, blue indicates cold advection), the low-level jet (large red arrow), the low-level baroclinic zone (stationary front symbol), and PW (values > 50 mm shaded in blue). The position of the PRE is indicated by the green shading, the position of the TC is indicated by the tropical storm symbol, and the maxima and minima in low-level geopotential height are indicated by the "H" and "L" symbols, respectively.

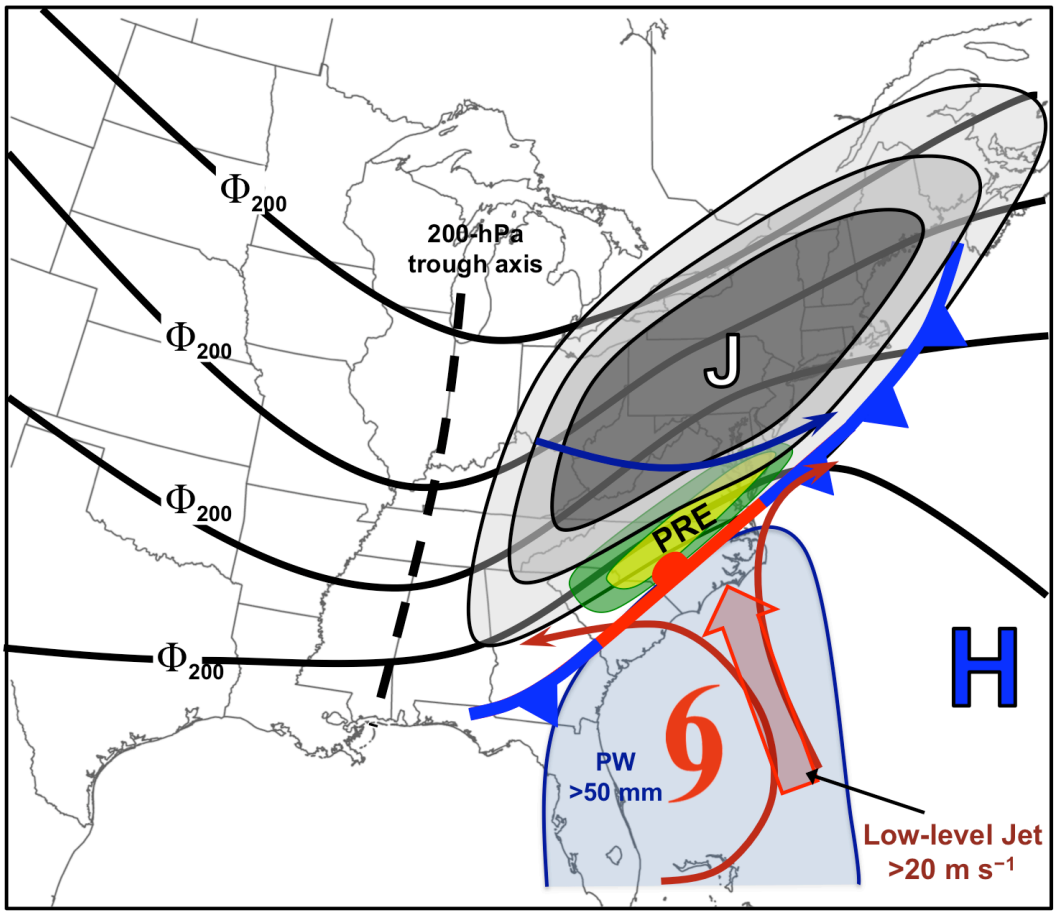


Figure 6.2: As in Fig. 6.1, except for the SJ category.

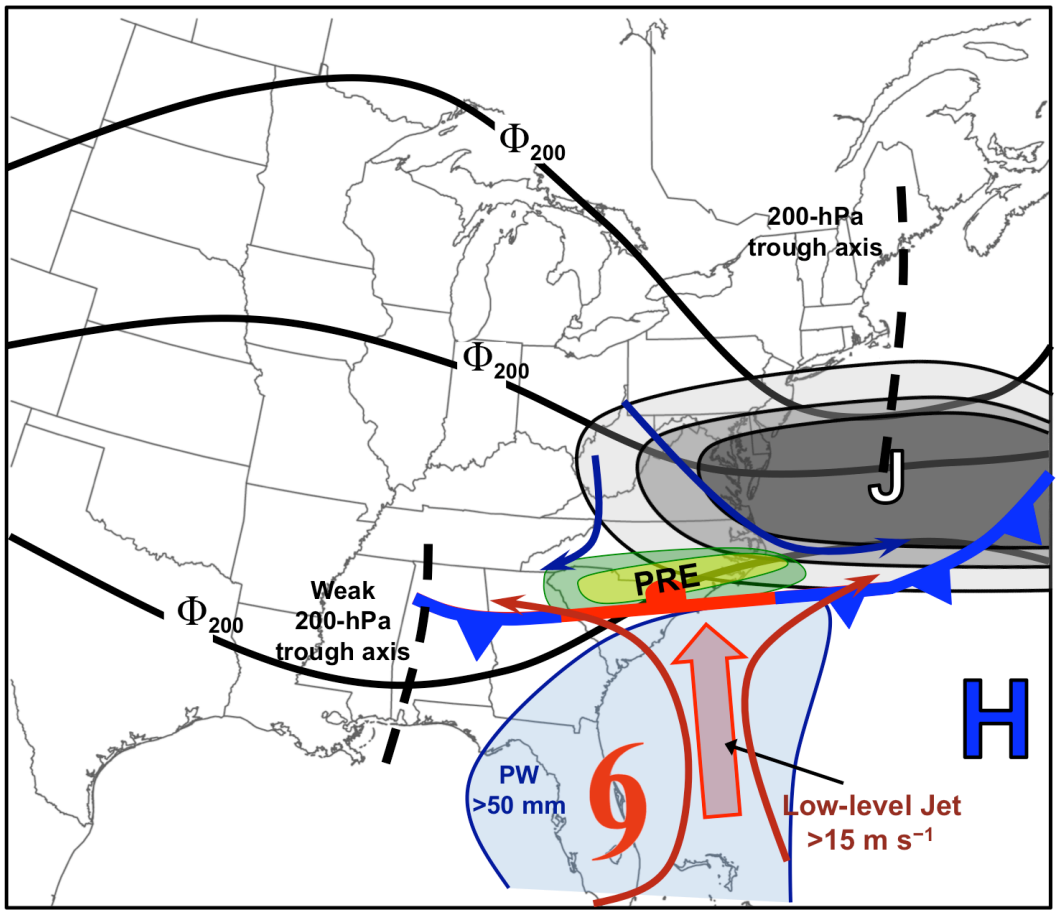


Figure 6.3: As in Fig. 6.1, except for the DC category.

## 7. Conclusions and suggestions for future work

### 7.1 Conclusions

The primary objectives of this thesis were to: 1) document the distinct synoptic-scale configurations favorable for the development of PREs, and 2) examine the dynamical mechanisms associated with PREs. To accomplish these objectives, PREs occurring in the U.S. ahead of North Atlantic basin TCs during 1988–2008 were stratified based upon the upper-tropospheric flow configuration within which the PRE and TC were embedded. This stratification procedure revealed three PRE categories: JR, SJ, and DC, each category linked to a distinct synoptic-scale flow configuration. Following this stratification procedure, a climatology for 1988–2008 was conducted in order to document the temporal and geographical distributions and the statistical properties of PREs. PRE-relative composites were prepared for each of the three PRE categories in order to elucidate the key synoptic-scale features and dynamical mechanisms associated with PRE development. The PREs associated with TC Rita (2005; JR category), TC Wilma (2005; SJ category), and TC Ernesto (2006; DC category) were selected for individual case studies.

The results of the composites and the case studies provide insight into the key environmental properties and dynamical mechanisms associated with PREs. These results also indicate that the influence of the TC on the development of the PRE varies among the three categories. For the JR category, a TC is typically embedded within an environment resembling the Maddox et al. (1979) "frontal" pattern for flash-flood-producing MCSs, acting as a source of moisture to a region already favorable for heavy rainfall. The SJ category is typified by the direct dynamical interaction between a TC

and an approaching midlatitude baroclinic system, often closely resembling the early stages of ET (e.g., Klein et al. 2000). During this TC–midlatitude interaction, the low-level cyclonic circulation and the upper-level diabatically driven outflow associated with the TC contribute to dynamical forcing for PRE development in the presence of deep moisture emanating from the TC. For the DC category, the role of the TC can vary among individual PRE cases. For many DC category PREs, the direct dynamical interaction between the TC and a weak midlatitude baroclinic zone contributes to the development of a PRE, whereas for others [e.g., the PRE ahead of TC Ernesto (2006)], the TC primarily acts as a source of moisture to a region already favorable for heavy rainfall and has no direct dynamical influence on the development of the PRE.

C07 asserted that a TC can contribute to the development of a PRE by: (1) transporting deep moisture poleward to a region of ascent, and (2) amplifying an upper-level ridge downstream of the TC through diabatic heating and enhancing the horizontal divergence within the equatorward entrance region of an intensifying upper-level jet streak. The results of the current study support this assertion and, moreover, suggest a third possible contribution of a TC: poleward low-level flow on the eastern flank of the cyclonic circulation of a TC can aid in establishing focused warm-air advection and frontogenesis along a low-level baroclinic zone.

## 7.2 Suggestions for future work

While this thesis provides insight into the favorable synoptic-scale environments and dynamical mechanisms associated with PREs, opportunities remain for future work on PREs. There is a continued need for detailed case studies in order to improve

understanding of the various dynamical processes associated with PREs. Unresolved issues related to operational forecasting that should be the subject of future case studies are: 1) the processes associated with the generation of multiple concurrent or consecutive PREs ahead of a single TC, and 2) the processes that govern the so-called "unclassifiable" (UC) PREs. UC PREs pose a considerable forecasting challenge because they typically occur in association with subtle mesoscale boundaries or with topographic features in environments of weak dynamical forcing. In conjunction with continued case studies, a comprehensive assessment of the performance of medium- and extended-range operational models for individual PRE cases is necessary in order to provide operational forecasters with useful information on how to use model guidance to forecast the location, intensity, and longevity of PREs.

The results of the composites and case studies presented in this thesis suggest that the presence of a stream of deep moisture emanating from a TC can significantly enhance rainfall totals associated with a PRE. Of interest from both an operational and a research perspective would be a quantitative assessment of the relative impact of TC-related moisture on rainfall totals in individual PRE cases using numerical model simulations. For these model simulations, the high moisture values associated with the TC could be reduced in the initial conditions to values representative of the ambient environment. The model could then be run through the lifespan of the PRE, and the resultant precipitation distribution could be compared with that of a control simulation or perhaps with actual precipitation observations.

Numerical model simulations could also be employed to assess the dynamical influence of a TC on PRE development. For assessing the role of the cyclonic circulation

of the TC, a similar methodology to the one used by McTaggart-Cowan et al. (2001) could be employed. Specifically, the PV anomaly associated with the TC circulation could be removed from the initial conditions of a numerical model simulation. Upon removal of this PV anomaly, a piecewise PV inversion (e.g., Davis 1992) could then be performed on the resultant PV field in order to obtain the balanced fields with which to initialize the model. The results of the model simulation could then be compared with the results of a control simulation that includes the PV anomaly associated with the TC in order to quantify the influence of the TC circulation on the development of the PRE. To assess the impacts of the diabatically driven outflow associated with the PRE and the TC, numerical model simulations could be run with the effects of latent heating removed and compared with a control simulation that includes the effects of latent heating.

## REFERENCES


Agustí-Panareda, A., C. D. Thorncroft, G. C. Craig, and S. L. Gray, 2004: The extratropical transition of Hurricane Irene (1999): A potential vorticity perspective. *Quart. J. Roy. Meteor. Soc.*, **130**, 1047–1074.

Atallah, E. H., and L. F. Bosart, 2003: The extratropical transition and precipitation distribution of Hurricane Floyd (1999). *Mon. Wea. Rev.,* **131,** 1063–1081.

——, ——, and A. R. Aiyyer, 2007: Precipitation distribution associated with landfalling tropical cyclones over the eastern United States. *Mon. Wea. Rev.,* **135,** 2185–2206.

Augustine, J. A., and F. Caracena, 1994: Lower-tropospheric precursors to nocturnal MCS development over the central United States. *Wea. Forecasting,* **9,** 116–135.

Beard, K. V., and H. T. Ochs III, 1993: Warm-rain initiation: An overview of microphysical mechanisms. *J. Appl. Meteor.,* **32**, 608–625.

Bell, G. D., and L. F. Bosart, 1988: Appalachian cold-air damming. *Mon. Wea. Rev.,* **116**, 137–161.

Benjamin, S. G., and Coauthors, 2002: RUC20 –The 20-km version of the Rapid Update Cycle. NWS Technical Procedures Bulletin 490, National Oceanic and Atmospheric Administration/National Weather Service, 30 pp.

Bluestein, H. B., 1992: *Principles of Kinematics and Dynamics.* Vol. I. *Synoptic-Dynamic Meteorology in Midlatitudes.* Oxford University Press, 431 pp.

Brennan, Michael J., Gary M. Lackmann, Kelly M. Mahoney, 2008: Potential vorticity (PV) thinking in operations: the utility of nonconservation. *Wea. Forecasting*, **23**, 168-182.

Bonner, W. D., 1968: Climatology of the low-level jet. *Mon. Wea. Rev.,* **96,** 833–850.

Bosart, L. F., 1975: New England coastal frontogenesis. *Quart. J. Roy. Meteor. Soc.*, **101**, 957–978.

——, and F. H. Carr, 1978: A case study of excessive rainfall centered around Wellsville, New York, 20–21 June 1972. *Mon. Wea. Rev.,* **106,** 348–362.

——, and G. M. Lackmann, 1995: Postlandfall tropical cyclone reintensification in a weakly baroclinic environment: A case study of Hurricane David (September 1979). *Mon. Wea. Rev.,* **123,** 3268–3291.

——, and D. B. Dean, 1991: The Agnes rainstorm of June 1972: Surface feature evolution culminating in inland storm redevelopment. *Wea. Forecasting,* **6,** 515–537.

Brooks, H. E., and D. J. Stensrud, 2000: Climatology of heavy rain events in the United States from hourly precipitation observations. *Mon. Wea. Rev.,* **128,** 1194–1201.

Caracena, F., R. A. Maddox, L. R. Hoxit, and C. F. Chappell, 1979: Mesoanalysis of the Big Thompson storm. *Mon. Wea. Rev.,* **107,** 1–17.

Carbone, R. E., J. D. Tuttle, D. A. Ahijevych, and S. B. Trier, 2002: Inferences of predictability associated with warm season precipitation episodes. *J. Atmos. Sci.*, **59**:2033–2056.

Carr, F. H., and L. F. Bosart, 1978: A diagnostic evaluation of rainfall predictability for Tropical Storm Agnes, June 1972. *Mon. Wea. Rev.,* **106,** 363–374.

Chappell, C. F., 1986: Quasi-stationary convective events. *Mesoscale Meteorology and Forecasting,* P. S. Ray, Ed. Amer. Meteor. Soc., 289–309.

Colle, B. A., 2003: Numerical simulations of the extratropical transition of Floyd (1999):

Structural evolution and responsible mechanisms for heavy rainfall over the northeast United States. *Mon. Wea. Rev.,* **131,** 2905–2926.

Corbosiero, K. L., M. J. Dickinson, and L. F. Bosart, 2009: The contribution of eastern North Pacific tropical cyclones to the rainfall climatology of the southwest United States. *Mon. Wea. Rev.,* **137,** 2415–2435.

Cote, M. R., 2007: Predecessor rain events in advance of tropical cyclones. M.S. Thesis, Department of Atmospheric and Environmental Sciences, University at Albany, State University of New York, 200 pp. [Available online at http://cstar.cestm.albany.edu/CAP_Projects/Project10/index.htm.]

Davis, C. A., 1992: Piecewise Potential Vorticity Inversion. *J. Atmos. Sci.,* **49**, 1397-1411.

——, K. W. Manning, R. E. Carbone, S. B. Trier, and J. D. Tuttle, 2003: Coherence of warm-season continental rainfall in numerical weather prediction models. *Mon. Wea. Rev.*, **131**:2667–2679.

Davis, R. S., 2001: Flash flood forecast and detection methods. *Severe Convective Storms, Meteor. Monogr.,* No. 50, Amer. Meteor. Soc., 481–525.

DiMego, G. J., and L. F. Bosart, 1982a: The transformation of tropical storm Agnes into an extratropical cyclone. Part I: The observed fields and vertical motion computations. *Mon. Wea. Rev.,* **110**, 385–411.

——, and ——, 1982b: The transformation of tropical storm Agnes into an extratropical cyclone. Part II: Moisture, vorticity and kinetic energy budgets. *Mon. Wea. Rev.,* **110**, 412–433.

Doswell, C. A., III, 1987: The distinction between large-scale and mesoscale contribution to severe convection: A case study example. *Wea. Forecasting,* **2**, 3–16.

——, H. E. Brooks, and R. A. Maddox, 1996: Flash flood forecasting: An ingredients-based methodology. *Wea. Forecasting,* **11,** 560–581.

_____, C. Ramis, R. Romero and S. Alonso (1998): A diagnostic study of three heavy precipitation episodes in the western Mediterranean. *Wea. Forecasting*, **13**, 102-124.

——, and L. F. Bosart, 2001: Extratropical synoptic-scale processes and sever convection. *Severe Convective Storms, Meteor. Monogr.,* No. 50, Amer. Meteor. Soc., 27–69.

Eliassen, A., 1962: On the vertical circulation in frontal zones. *Geofys. Publ.*, **24**, 147–160.

Farfán, L. M. and I. Fogel, 2007: Influence of tropical cyclones on humidity patterns over southern Baja California, Mexico. *Mon. Wea. Rev.*, **135**, 1208–1224.

Funk, T. W., 1991: Forecasting techniques utilized by the forecast branch of the National Meteorological Center during a major convective rainfall event. *Wea. Forecasting,* **6**, 548–564.

——, 2003: Heavy convective rainfall forecasting: A comprehensive look at parameters, processes, patterns, and rules of thumb. Training document, National Weather Service weather forecast office, Louisville, KY. [Available online at http://www.crh.noaa.gov/lmk/soo/docu/.].

Galarneau, T. J., Jr., L. F. Bosart, and R. S. Schumacher, 2010: Predecessor rain events ahead of tropical cyclones. *Mon. Wea. Rev.,* In press.

Glass, F. H., D. L. Ferry, J. T. Moore, and S. M. Nolan, 1995: Characteristics of heavy convective rainfall events across the mid-Mississippi valley during the warm season: Meteorological conditions and a conceptual model. Preprints, *14th Conf. on Weather Analysis and Forecasting,* Dallas, TX, Amer. Meteor. Soc., 34–41.

Hakim, G. J., and D. Keyser, 2001: Canonical frontal circulation patterns in terms of Green's functions for the Sawyer–Eliassen equation. *Quart. J. Roy. Meteor. Soc.*, **127**, 1795–1814.

Harr, P. A., and R. L. Elsberry, 2000: Extratropical transition of tropical cyclones over the western north Pacific. Part I: Evolution of structural characteristics during the transition process. *Mon. Wea. Rev.*, **128**, 2613–2633.

——, ——, and T. F. Hogan, 2000: Extratropical transition of tropical cyclones over the western north Pacific. Part II: The impact of midlatitude circulation characteristics. *Mon. Wea. Rev.*, **128**, 2634–2653.

Higgins, R. W., W. Shi, E. Yarosh, and R. Joyce, 2000: Improved United States Precipitation Quality Control System and Analysis. [Available online at http://www.cpc.ncep.noaa.gov/research_papers/ncep_cpc_atlas/7/toc.html.].

Higgins, R. W. and W. Shi, 2005: Relationships between Gulf of California moisture surges and tropical cyclones in the eastern Pacific basin. *J. Climate*, **18**, 4601–4620.

Hoskins, B. J., I. Draghici, and H. C. Davies, 1978: A new look at the omega equation. *Quart. J. Roy. Meteor. Soc.,* **104,** 31–38.

——, M. McIntyre, and A. W. Robertson, 1985: On the use and significance of isentropic potential vorticity maps. *Quart. J. Roy. Meteor. Soc.*, **111**:877–946.

Houze, R. A., Jr., B. F. Smull, and P. Dodge, 1990: Mesoscale organization of springtime rainstorms in Oklahoma. *Mon. Wea. Rev.,* **118**, 613–654.

——, R. A., Jr., 2004: Mesoscale convective systems. *Rev. Geophys.*, **42**, 10.1029/2004RG000150, 43 pp.

Hsie, E-Y., R. A. Anthes, and D. Keyser, 1984: Numerical simulation of frontogenesis in a moist atmosphere. *J. Atmos. Sci.*, **41**, 2581–2594.

Jankov, I. and W. A. Gallus, 2004: MCS rainfall forecast accuracy as a function of large-scale forcing. *Wea. Forecasting*, **19**:428–439.

Jones, S. C., and Coauthors, 2003: The extratropical transition of tropical cyclones: Forecast challenges, current understanding, and future directions. *Wea. Forecasting,* **18,** 1052–1092.

Junker, N. W., R. S. Schneider, and S. L. Fauver, 1999: A study of heavy rainfall events during the Great Midwest Flood of 1993. *Wea. Forecasting,* **14,** 701–712.

Kalnay, E., and Coauthors, 1996: The NCEP/NCAR 40-Year Reanalysis Project. *Bull. Amer. Meteor. Soc.,* **77,** 437–472.

Keyser, D., M. J. Reeder, and R. J. Reed, 1988: A generalization of Petterssen's frontogenesis function and its relation to the forcing of vertical motion. *Mon. Wea. Rev.*, **116**, 762–780.

——, B. D. Schmidt, and D. G. Duffy, 1992: Quasigeostrophic vertical motions diagnosed from along- and cross-isentrope components of the Q vector. *Mon. Wea. Rev.*, **120**, 731–741.

——,1999: On the representation and diagnosis of frontal circulations in two and three dimensions. *The Life Cycles of Extratropical Cyclones,* M. A. Shapiro and S.

Gronas, Eds., Amer. Meteor. Soc., 239-264.

Keyser, D. A. and D. R. Johnson, 1984: Effects of diabatic heating on the ageostrophic circulation of an upper tropospheric jet streak. *Mon. Wea. Rev.*, **112**, 1709–1724.

Kistler, R., and Coauthors, 2001: The NCEP/NCAR 50-year reanalysis: Monthly means CD-ROM and documentation. *Bull. Amer. Meteor. Soc.*, **82**, 247–267.

Klein, J. R., 2007: Mesoscale precipitation structures accompanying landfalling and transitioning tropical cyclones over the northeast United States. M.S. Thesis, Department of Atmospheric and Environmental Sciences, University at Albany, State University of New York, 139 pp. [Available online at http://cstar.cestm.albany.edu/CAP_Projects/Project10/index.htm.]

Klein, P. M., P. A. Harr, and R. L. Elsberry, 2000: Extratropical transition of western north Pacific tropical cyclones: An overview and conceptual model of the transformation stage. *Wea. and Forecasting*, **15**, 373–395.

——, ——, and ——, 2002: Extratropical transition of western north Pacific tropical cyclones: Midlatitude and tropical cyclone contributions to reintensification. *Mon. Wea. Rev.*, **130**, 2240–2259.

Konrad, C. E., II, 1997: Synoptic-scale features associated with warm season heavy rainfall over the interior southeastern United States. *Wea. Forecasting,* **12**, 557–571.

LaPenta, K. D., and Coauthors, 1995: The challenge of forecasting heavy rain and flooding throughout the eastern region of the National Weather Service. Part I: Characteristics and events. *Wea. Forecasting*, **10**, 78–90.

Lin, Y. L, S. Chiao, T. A. Wang, M. L. Kaplan, and R. P. Weglarz, 2001: Some common ingredients for heavy orographic rainfall. *Wea. Forecasting,* **16**, 633–660.

Maddox, R. A., 1980: Mesoscale convective complexes. *Bull. Amer. Meteor. Soc.,* **60,** 115–123.

——, 1983: Large-scale meteorological conditions associated with midlatitude mesoscale convective complexes. *Mon. Wea. Rev.*, **111**, 1475–1493.

——, L. R. Hoxit, C. F. Chappell, and F. Caracena, 1978: Comparison of meteorological aspects of the Big Thompson and Rapid City flash floods. *Mon. Wea. Rev.,* **106,** 375–389.

——, C. F. Chappell, and L. R. Hoxit, 1979: Synoptic and meso- scale aspects of flash flood events. *Bull. Amer. Meteor. Soc.,* **60,** 115–123.

——, D. J. Perkey, and J. M. Fritsch, 1981: Evolution of upper tropospheric features during the development of a mesoscale convective complex. *J. Atmos. Sci.,***38,** 1664–1674.

Market, P., S. Allen, R. Scofield, R. Kuligowski, and A. Gruber, 2003: Precipitation efficiency of warm-season Midwestern mesoscale convective systems. *Wea. Forecasting,* **18,** 1273–1285.

Martin, J. E., 2006a: *Mid-latitude Atmospheric Dynamics: A First Course.* John Wiley and Sons, 336 pp.

——, 2006b: The role of shearwise and transverse quasigeostrophic vertical motions in the midlatitude cyclone life cycle. *Mon. Wea. Rev.,* **134,** 1174–1193.

McDonald, B.E., and M.N. Baker, 2001: The NWS National QPF Verification Program. COMET RFC/HPC Hydrometeorology course 02-1. [Available online at http://www.hpc.ncep.noaa.gov/npvu/confpres/hydromet02/hydromet02_1.pdf.].

McTaggart-Cowan, R., J. R. Gyakum, M. K. Yau, 2001: Sensitivity Testing of Extratropical Transitions Using Potential Vorticity Inversions to Modify Initial Conditions: Hurricane Earl Case Study. *Mon. Wea. Rev.,* **129**, 1617-1636.

Moore, J. T., F. H. Glass, C. E. Graves, S. M. Rochette, and M. J. Singer, 2003: The environment of warm-season elevated thunderstorms associated with heavy rainfall over the central United States. *Wea. Forecasting,* **18,** 861–878.

Moore, J. T. and G. E. VanKnowe, 1992: The effect of jet-streak curvature on kinematic fields. *Mon. Wea. Rev.*, **120**, 2429–2441.

Morgan, M. C. and J. W. Nielsen-Gammon, 1998: Using tropopause maps to diagnose midlatitude weather systems. *Mon. Wea. Rev.*, **126**, 2555–2579.

O'Handley, C., and L. F. Bosart, **1996**: The impact of the Appalachian mountains on cyclonic weather systems Part I: A climatology. *Mon. Wea. Rev.*, **124**, 1353–1373.

Parker, M. D., 2007: Simulated convective lines with parallel precipitation. Part I: Basic structures. *J. Atmos. Sci.*, **64**, 267–288.

Petterssen, S., 1936: Contribution to the theory of frontogenesis. *Geofys. Publ.,* **11**(6), 1–27.

——, 1956: *Weather Analysis and Forecasting, Vol. 1, Motion and Motion Systems.* 2nd ed. McGraw-Hill 428 pp.

Pierce, C. H., 1939: The meteorological history of the New England hurricane of Sept. 21, 1938. *Mon. Wea. Rev.,* **67,** 237–285.

Pontrelli, M. D., G. Bryan, and J. M. Fritsch, 1999: The Madison County, Virginia, flash flood of 27 June 1995. *Wea. Forecasting,* **14,** 384–404.

Pyle, M. E., D. Keyser, and L. F. Bosart, 2004: A diagnostic study of jet streaks: Kinematic signatures and relationship to coherent tropopanse disturbances. *Mon. Wea. Rev.*, **132**, 297–319.

Ralph, F. M., P. J. Neiman, and R. Rotunno, 2005: Dropsonde observations in low-level jets over the northeastern Pacific Ocean from CALJET-1998 and PACJET-2001: Mean vertical-profile and atmospheric-river characteristics. *Mon. Wea. Rev.*, **133**, 889–910.

Riemer, M., S. C. Jones, and C. A. Davis, 2008: The impact of extratropical transition on the downstream flow: An idealised modelling study with a straight jet. *Quart. J. Roy. Meteor. Soc.,* **134**, 69–91.

Romero, R., C. A. Doswell III, and C. Ramis, 2000: Mesoscale numerical study of two cases of long-lived quasistationary convective systems over eastern Spain. *Mon. Wea. Rev*, **128**, 3731–3751.

Schumacher, P. N., D. J. Knight, and L. F. Bosart, 1996: Frontal interaction with the Appalachian Mountains. Part I: A climatology. *Mon. Wea. Rev.*, **124**, 2453–2468.

Schumacher, R. S., and R. H. Johnson, 2005: Organization and environmental properties of extreme-rain-producing mesoscale convective systems. *Mon. Wea. Rev.,* **133,** 961–976.

——, and ——, 2006: Characteristics of U.S. extreme rain events during 1999–2003. *Wea. Forecasting,* **21,** 69–85.

——, and ——, 2008: Mesoscale processes contributing to extreme rainfall in a

midlatitude warm-season flash flood. *Mon. Wea. Rev.,* **136,** 3964–3986.

——, and ——, 2009: Quasi-stationary, extreme-rain-producing convective systems associated with midlevel cyclonic circulations. *Wea. Forecasting,* **24,** 555–574.

Schwarz, F. K., 1970: The unprecedented rains in Virginia associated with the remnants of Hurricane Camille. *Mon. Wea. Rev.,* **98,** 851–859.

Sinclair, M. R., 1993: A diagnostic study of the extratropical precipitation resulting from Tropical Cyclone Bola. *Mon. Wea. Rev.*, **121**, 2690–2707.

Srock, A. F., and L. F. Bosart, 2009: Heavy precipitation associated with southern Appalachian cold-air damming and Carolina coastal frontogenesis in advance of weak landfalling Tropical Storm Marco (1990). *Mon. Wea. Rev.,* **137,** 2448–2470.

Svoma, B. M., 2010: The influence of monsoonal gulf surges on precipitation and diurnal precipitation patterns in central Arizona. *Wea. Forecasting,* **25**, 281–289.

Trenberth, K. E., 1978: On the interpretation of the diagnostic quasi-geostrophic omega equation. *Mon. Wea. Rev.,* **106**, 131–137.

Trier, S. B. and D. B. Parsons, 1993: Evolution of environmental conditions preceding the development of a nocturnal mesoscale convective complex. *Mon. Wea. Rev.*, **121**, 1078–1098.

——, C. A. Davis, D. A. Ahijevych, M. L. Weisman, and G. H. Bryan, 2006: Mechanisms supporting long-lived episodes of propagating nocturnal convection within a 7-day WRF model simulation. *J. Atmos. Sci.,* **63,** 2437–2461.

——, and R. D. Sharman, 2009: Convection-permitting simulations of the environment supporting widespread turbulence within the upper-level outflow of an MCS. *Mon. Wea. Rev.*, **137,** 1972–1990.

Tuttle, J. D. and C. A. Davis, 2006: Corridors of warm season precipitation in the central United States. *Mon. Wea. Rev.*, **134**, 2297–2317.

Uccellini, L. W., and D. R. Johnson, 1979: The coupling of upper and lower tropospheric jet streaks and implications for the development of severe convective storms. *Mon. Wea. Rev.,* **107,** 682–703.

——, 1980: On the role of upper tropospheric jet streaks and leeside cyclogenesis in the development of low-level jets in the Great Plains. *Mon. Wea. Rev.,* **108,** 1689–1696.

Wang, Yo., Wang, Yu., and H. Fudeyasu, 2009: Effect of Typhoon Songda (2004) on remote heavy rainfall in Japan. *Mon. Wea. Rev.,* **137,** 3699–3716.

Wu, Chun-Chieh, Kerry A. Emanuel, 1993: Interaction of a baroclinic vortex with background shear: application to hurricane movement. *J. Atmos. Sci.,* **50**, 62-76.